

NAUSIVIOS CHORA

A Journal in Naval Sciences and Technology

PART A:

Mechanical and Marine Engineering



ΝΑΥΣΙΒΙΟΣ ΧΩΡΑ

Περιοδική Έκδοση Ναυτικών Επιστημών

ΜΕΡΟΣ Α:

**Επιστήμες Ναυπηγού και Μηχανολόγου
Μηχανικού**

Volume 7/2018 - Τεύχος 7/2018

TABLE OF CONTENTS

Marios I. Kourampas, Elias A. Yfantis, John S. Katsanis and Efthimios G. Pariotis, <i>Development of a Computational Model for DI Diesel Engine Cylinder Pressure, Injection Pressure and TDC Position Data Processing and Performance Analysis</i>	A-3
Charalampos Titakis, Panayota Vassiliou and Ioannis Ziomas, <i>Atmospheric Corrosion of Carbon Steel, Aluminum, Copper and Zinc in a Coastal Military Airport in Greece</i>	A-35
John S. Katsanis, Marios I. Kourampas, Elias A. Yfantis, Efthimios G. Pariotis and Theodoros C. Zannis, <i>Thermodynamic Analysis of the Effect of Compression and Injection Quality Faults on DI Diesel Engine Combustion and Performance Characteristics</i>	A-59

Development of a Computational Model for DI Diesel Engine Cylinder Pressure, Injection Pressure and TDC Position Data Processing and Performance Analysis

Marios I. Kourampas^a, Elias A. Yfantis^a, John S. Katsanis^a and Efthimios G. Pariotis^a

^a*Naval Architecture and Marine Engineering Section, Hellenic Naval Academy, End of Hatzikiriakou Ave. 18539 Piraeus, Greece*

Abstract. A general-purpose computational model is developed for processing experimental data for cylinder pressure, injection pressure and top dead centre (TDC) position, which can be obtained from direct injection (DI) diesel engines. Specifically, the developed computational model is able to process measured data for in-cylinder pressure, fuel injection pressure and TDC position obtained from engine tests in a DI diesel engine over many engine cycles at a certain engine operating point i.e. specific engine speed and load. Upon processing, the computational model calculates the average cylinder pressure and injection pressure profiles over all received cycles and then, it uses the aforementioned profiles for calculating main engine performance characteristics such as indicated power, indicated mean effective pressure (IMEP) and indicated specific fuel consumption (ISFC). The model also performs a heat release rate analysis for calculating instantaneous and cumulative gross and neat release rates and also instantaneous in-cylinder heat loss rates. The developed model is used in the present study for processing in-cylinder pressure and injection pressure for five conventional diesel fuels with variable physical properties, which were obtained during an experimental investigation performed in a single-cylinder high-speed DI diesel engine. Hence, the influence of variable fuel physical properties such as density, viscosity and compressibility factor on DI diesel engine performance characteristics and combustion parameters is facilitated through developed model analysis.

Keywords: diesel engine; cylinder pressure; injection pressure; combustion; performance

INTRODUCTION

Deterioration of the global warming phenomenon in combination with the high prices of fossil fuels require the implementation of drastic measures for the further improvement of brake specific fuel consumption (BSFC) and the reduction of gaseous and particulate pollutants emitted from internal combustion engines. Despite their superior thermal efficiency compared to all other thermal engines, diesel engines still emit high values of CO₂, NO_x, PM, CO and HC emissions,

which are strongly interrelated not only with diesel engine configuration, settings and size but also with fuel molecular structure and physical and chemical properties [1-5]. Hence, one of the most promising techniques for the curtailment of gaseous and particulate emissions from diesel engines is the optimization of the chemical synthesis and the physical and chemical properties of conventional diesel oils [6-11]. The optimization of the chemical synthesis and the physical and chemical properties of light diesel fuels can lead to the substantial improvement of the operational and environmental behavior not only of future but also of existing fleet of diesel-powered vehicles [9,11]. According to the literature [12-18], the physical and the chemical properties of diesel fuels affect in a different manner the main diesel engine performance parameters and each one of the gaseous and particulate emissions (CO₂, CO, HC, NO_x and soot). For example, it has reported in the literature [9,11,18-20] that CO, HC and aldehyde emissions are depending on fuel cetane number whereas, NO_x emissions are primarily affected by fuel density and polyaromatic hydrocarbon and soot emissions are directly correlated to diesel fuel aromatic content. Conventional diesel oil composition in monoaromatic, diaromatic and triaromatic hydrocarbons as well as in aromatic species affects explicitly its physical and chemical properties and thus it defines its diesel engine combustion behavior and its tendency for formation of gaseous and particulate pollutants [1-4,9,11,18-20]. In general, there is a strong interaction between fuel molecular structure (paraffins, olefins, naphthenes and aromatic hydrocarbons), fuel chemical properties (cetane number, ignition point etc.) and fuel physical properties (density, viscosity, surface tension and compressibility factor) [4-7,9,11,12-14,16]. Hence, it is quite difficult – if not impossible – to assign specific variations observed in the diesel engine performance characteristics and pollutant emissions from the replacement of one diesel fuel from another to the variation of only one fuel property. For this reason, according to the literature [21,22], the type and the degree of fuel effect on diesel engine performance characteristics and pollutant emissions varies significantly with engine type used in experiments, the specific procedure followed to perform the engine tests and the method used for preparing the test fuels.

The detailed and effective evaluation of a diesel fuel influence on diesel engine combustion characteristics and pollutant emissions is based on the accurate measurement of cylinder pressure profile (i.e. variation of cylinder pressure with crank angle during entire engine operating cycle). Also in many cases the assessment of the impact of fuel properties on diesel engine injection system characteristics is based on the accurate measurement of fuel injection pressure. The accurate measurement of cylinder pressure is essential for the proper calculation of cylinder main performance and combustion characteristics such as indicated power, indicated mean effective pressure (IMEP), indicated specific fuel consumption (ISFC), ignition angle, combustion duration and ignition delay. Also the precise measurement of fuel injection pressure is essential for the exact calculation of injection pressure profile, start of injection (SOI) or else, dynamic injection timing, fuel injection rate and injection duration. The calculation of all aforementioned performance parameters in diesel engines require not only the accurate measurement of cylinder pressure and injection pressure but also the measurement of Top Dead Centre (TDC) position for determining the average cylinder pressure and injection pressure diagram from all recorded engine cycles at a certain engine operating point (i.e. engine load and speed). Also the precise measurement of cylinder pressure is essential for diesel engine condition monitoring and diagnostics applications [23]. The precise measurement of fuel injection pressure can also be quite useful for condition monitoring and diagnostics of a diesel engine fuel injection system (fuel pump, high-pressure fuel line and fuel injector).

The first attempts for measuring cylinder pressure are very old and in these attempts high-speed electronic transducers capable of converting the deflection of a low inertia diaphragm to electric signal were designed for satisfying the requirement for cylinder pressure measurement instrumentation with superior quality characteristics compared to previous attempts. Initial editions of these devices indicated sufficient frequency response to the phenomena taking place inside the combustion chambers of internal combustion engines and they developed using extensometers [24] and piezoelectric transducers as cylinder pressure sensors. However, these new electronic pressure transducers, which were connected with analog data acquisition systems, were comprised of a signal amplifier, a cathode ray oscilloscope and a photographic camera, which was used for the recording of the cylinder pressure signal from the oscilloscope (Brown, 1967). This cylinder pressure measuring process was difficult and it indicated various uncertainties associated with the photographic film exposure time and the cylinder pressure trace in the oscilloscope [25].

At the end of 1960's, more sophisticated analog systems become available, which were capable of performing a complete electronic processing of the cylinder pressure signal from the piezoelectric transducer. These devices were initially used for specific applications as the determination of the cylinder indicated power [26], the indicated mean effective pressure [27] and the phenomena of knocking and misfiring in spark-ignition engines [28]. The interface of these measuring devices with the user comprised of a voltmeter, which indicated a voltage analogous to the indicated mean effective pressure or alternatively, comprised of an electromechanical counter, which indicated the number of cycles at which appeared knocking or misfiring phenomena. At the middle of 1970's, analog to digital converters were incorporated in the engine experimental equipment and thus, experimental measurements of multiple targets and lower complexity were available compared to the recent past [25,29]. From this time period and then, the cylinder pressure signal after the amplifiers were digitized and stored in personal computers allowing its further processing through proper software. Hence, it was secured higher storage capacity and flexibility in cylinder pressure data processing sustaining also in parallel acceptable levels of measuring accuracy [25,29].

Nowadays there are sophisticated systems for recording various engine operating parameters such as cylinder pressure, fuel line pressure and TDC position [30,31]. Specifically, the fuel pressure in the high-pressure fuel line is recorded by a sensor based on a strain gauge or either a piezoelectric transducer, which is connected to an amplifier whereas the signal generated by the cylinder pressure piezoelectric transducer can be processed using two different processes [30-33]. In the first process, the cylinder pressure is obtained using a signal amplifier, which amplifies the cylinder pressure signal received from the piezoelectric transducer, whereas in the second process an electric current transducer is used for the measurement of the cylinder pressure variation rate [30-33]. The cylinder pressure measurements are correlated with the angular position of the crankshaft with reference the compression TDC. Usually the angular position of the crankshaft is determined using an optical crank encoder, which provides a pulse per crank rotation in a channel, which is used for the determination of the TDC reference angle and 720 pulses per two rotations stored in a second channel for the determination of the instantaneous relative angular position. External pulse multipliers can be used for the improvement of the sensitivity of the relative angular position up to 3600 pulses per rotation. Each angular position pulse activates a high-speed data acquisition system, which is capable of receiving simultaneously signals from the amplifiers and to collect data from multiple engine cycles for

determining the average cylinder pressure and injection pressure profiles over all received engine cycles and finally, store all the data in a personal computer [30-33].

From the aforementioned literature review, it becomes obvious that the measurement of cylinder pressure and injection pressure in diesel engines are of high importance for understanding the underlying transport phenomena taking place inside a cylinder of a diesel engine. Also the accurate measurement of cylinder pressure and injection pressure is essential in the case of diesel engine tests with fuels of different synthesis and physicochemical properties since the individual impact of each fuel on diesel engine performance characteristics and combustion parameters is facilitated through the processing of measured cylinder pressure and injection pressure data.

For this reason, in the present study a detailed computational model is developed for processing raw cylinder pressure, injection pressure and TDC position data obtained from a high-speed single-cylinder naturally-aspirated DI diesel engine at various operating conditions using five test fuels with different fuel properties. The computational model is general purpose software developed in MATLAB [34], which requires a limited number of input data and it can be used for diesel engine experimental data processing both in four-stroke and two-stroke engines and also it can be used for processing signals received from two sensors (cylinder pressure piezoelectric transducer and TDC position magnetic pickup or shaft encoder). Hence, experimental data for cylinder pressure, injection pressure and TDC position obtained during a previous experimental investigation in a single-cylinder DI diesel engine using five test fuels with different properties are processed from the developed computational model and useful experimental results for performance parameters and combustion characteristics are generated, which are thoroughly discussed.

TEST FUELS DESCRIPTION

The conventional test diesel oils used in the present study were prepared under a European research program, which aimed to the determination of fuels that can be used in both existing and future fleet of diesel-powered vehicles [21,22]. The main purpose of this research program was the determination of the optimum diesel fuel physical properties for attaining a further reduction of diesel emitted pollutants without deteriorating or if possible further improving the specific fuel consumption of modern diesel engines. Hence, under this research program, five conventional diesel oils were prepared by an oil refinery in Finland for examining the effect of fuel density, viscosity and compressibility factor on diesel engine performance characteristics and gaseous and pollutant emissions [21,22]. Initially, the specifications of the reference fuel, which was called “BASE” fuel were chosen. This fuel was used for the preparation of other fuels of the specific research program. The main specifications of the “BASE” fuel, which was selected to be Finnish summer grade city diesel oil, were the following [21]:

- Density: 820 – 840 kg/m³.
- Viscosity: 2 – 4 mm²/s.
- Cetane number: higher than 55.
- Total aromatic content: close to 20% w/w
- Polyaromatic content: lower than 5% w/w
- Sulfur content: 20 ppm.
- Additive type: Only cetane number improver and fuel lubricity improver

Upon determination of the specific requirements of the “base” fuel, four additional conventional diesel oils namely D1, D2, D3 and D4 were prepared with variable density, viscosity and compressibility factor. Figures 1-5 provide a comparison of the main compositional parameters, physical properties and chemical properties of all test fuels (i.e. BASE, D1, D2, D3 and D4) considered in this study for understanding individual variations in chemical synthesis and properties between test fuels. In Figure 1(a) are shown the values of paraffinic content of each one of test fuels BASE, D1, D2, D3 and D4. As evidenced, the highest paraffinic content corresponds to fuel D1 since this fuel was prepared from the mixing of paraffins with a low temperature distillation additive. The paraffinic content of test fuels BASE, D3 and D4 is almost similar. Figure 1(b) shows a comparison of the naphthenic content of test fuels BASE, D1, D2, D3 and D4. The highest value of naphthenes is observed in the case of test fuel D2 compared to all other fuels. Observing both Figures 1(a) and 1(b) it can be concluded that the transition from fuel D1 to fuel D2 and also the transition from fuel D3 to fuel D4 is accompanied by reduction in paraffins and simultaneous increase of naphthenes.

From the observation also of Figure 2(a) it can be derived that the highest value of aromatic content is witnessed for BASE fuel whereas the aromatic contents of test fuels D1, D2, D3 and D4 are similar. According to Figure 2(b), the transition from test fuel D1 to fuel D2 and the corresponding transition from fuel D3 to fuel D4 results in a relative increase of distillation temperature 5% v/v.

Also from the observation of Figures 3(a) and 3(b), which show corresponding comparisons of distillation temperature 50% v/v and distillation temperature 95% v/v for all fuels considered in the present analysis, the transition from fuel D1 to fuel D2 and the pertinent transition from fuel D3 to D4 results in a substantial increase of both distillation temperatures. This can be ascribed to the fact that fuel D2 contains a high distillation temperature whereas fuel D1 contains a low distillation temperature additive. Also fuel D3 is the mixing product of BASE fuel and a low distillation temperature additive whereas fuel D4 is a high distillation temperature fuel.

Figure 4(a) shows a comparison of cetane numbers of test fuels BASE, D1, D2, D3 and D4 whereas Figure 4(b) shows a comparison of LHV of the aforementioned test fuels. As evidenced from Figure 4(a), the increase of distillation temperature observed in the transition cases D1 to D2 and D3 to D4 results in an increase of the cetane number of fuels D4 and D2 compared to the ones of fuels D3 and D1 respectively. Also, as witnessed from Figure 4(b), there are no serious deviations in LHV between test fuels BASE, D1, D2, D3 and D4.

According to Figure 5(a), which shows a comparison of density values of test fuels BASE, D1, D2, D3 and D4, density values of fuels BASE, D2 and D4 are similar and are obviously higher than the corresponding values of test fuels D1 and D3. The same behavior is evidenced from the examination of Figure 5(b), which illustrates comparison of viscosity values of all fuels examined in this study. On the other hand, according to Figure 5(c), the transition from fuel D1 to D2 and the pertinent transition from fuel D3 to D4 results in reduction of compressibility factor.

Consequently, the main conclusion emerging from the detailed examination of the chemical synthesis and the physical and chemical properties of test fuels BASE, D1, D2, D3 and D4 is that the transition from test fuel D1 to test fuel D2 and the corresponding transition from fuel D3 to fuel D4 results in a substantial increase of fuel density and fuel viscosity and in a simultaneous reduction of compressibility as a result of the partial replacement of paraffins from naphthenes and of the increase of the distillation temperature. Hence, the processing of cylinder and injection pressure data and the implementation of heat release rate analysis for fuel pairs D1-D2 and D3-

D4 will facilitate the derivation of conclusions regarding the influence of fuel density, viscosity and compressibility on DI diesel engine performance parameters and combustion characteristics.

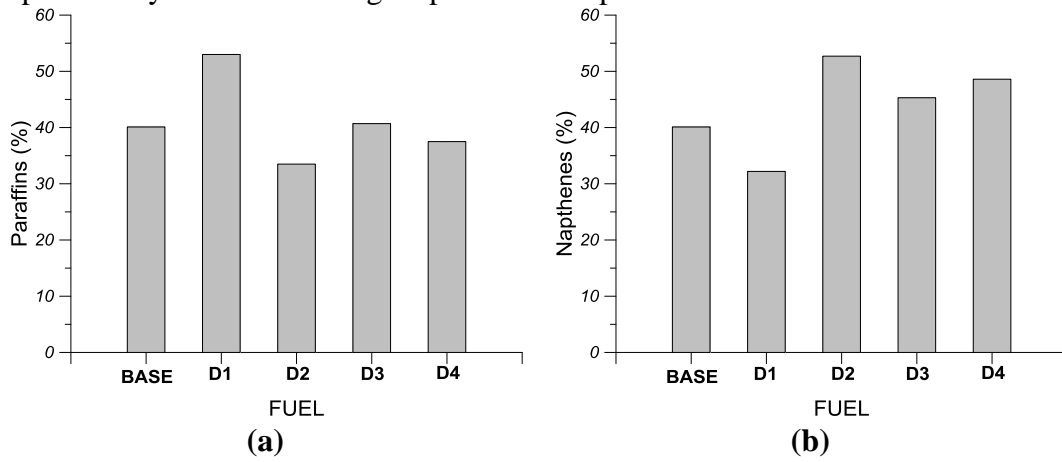


FIGURE 1. Comparison of (a) paraffins and (b) naphthenes of the test fuels BASE, D1, D2, D3 and D4, which are examined in the present study [21]

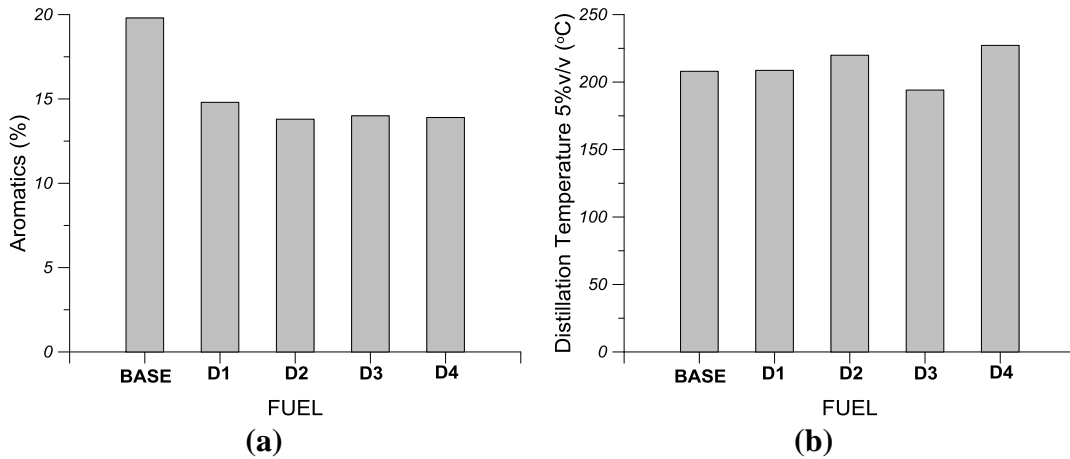


FIGURE 2. Comparison of (a) aromatics and (b) distillation temperature 5% v/v of the test fuels BASE, D1, D2, D3 and D4, which are examined in the present study [21]

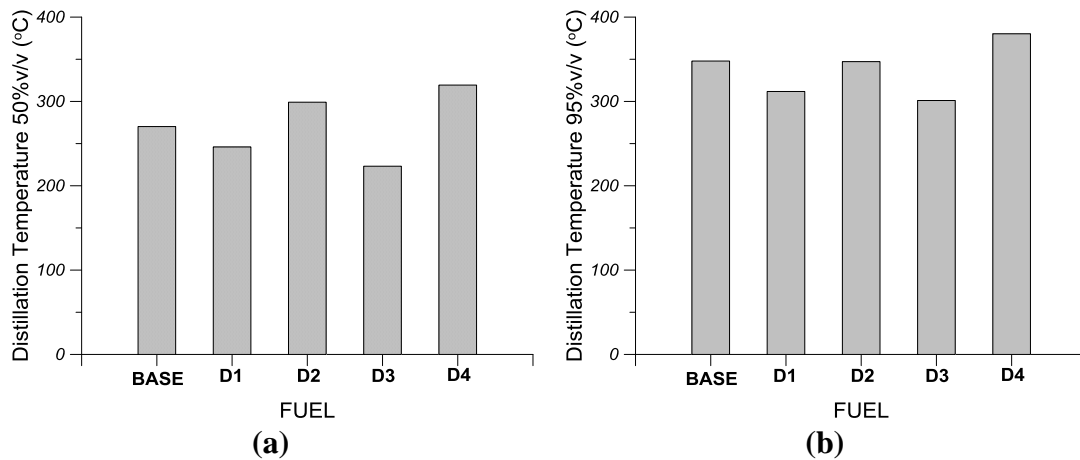


FIGURE 3. Comparison of (a) distillation temperature 50% v/v and (b) distillation temperature 95% v/v of the test fuels BASE, D1, D2, D3 and D4, which are examined in the present study [21]

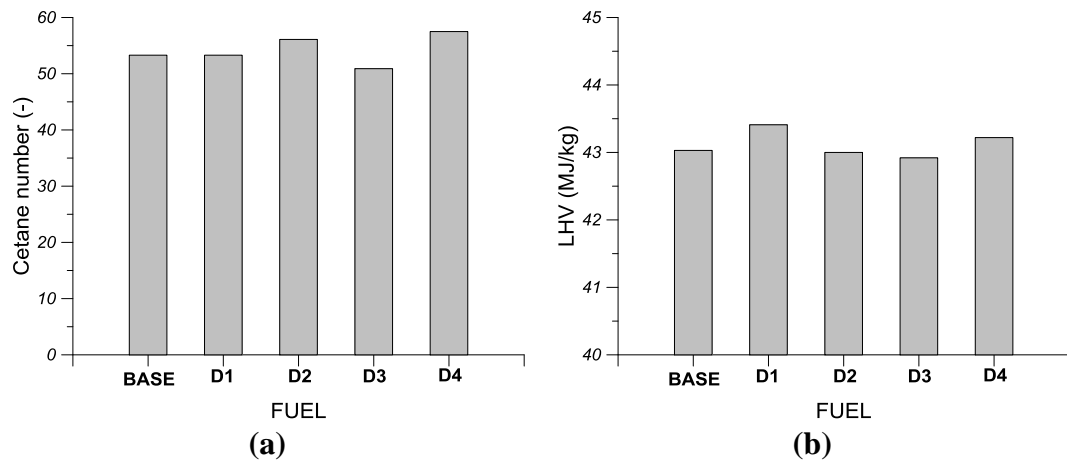


FIGURE 4. Comparison of (a) cetane number and (b) lower heating value (LHV) of the test fuels BASE, D1, D2, D3 and D4, which are examined in the present study [21]

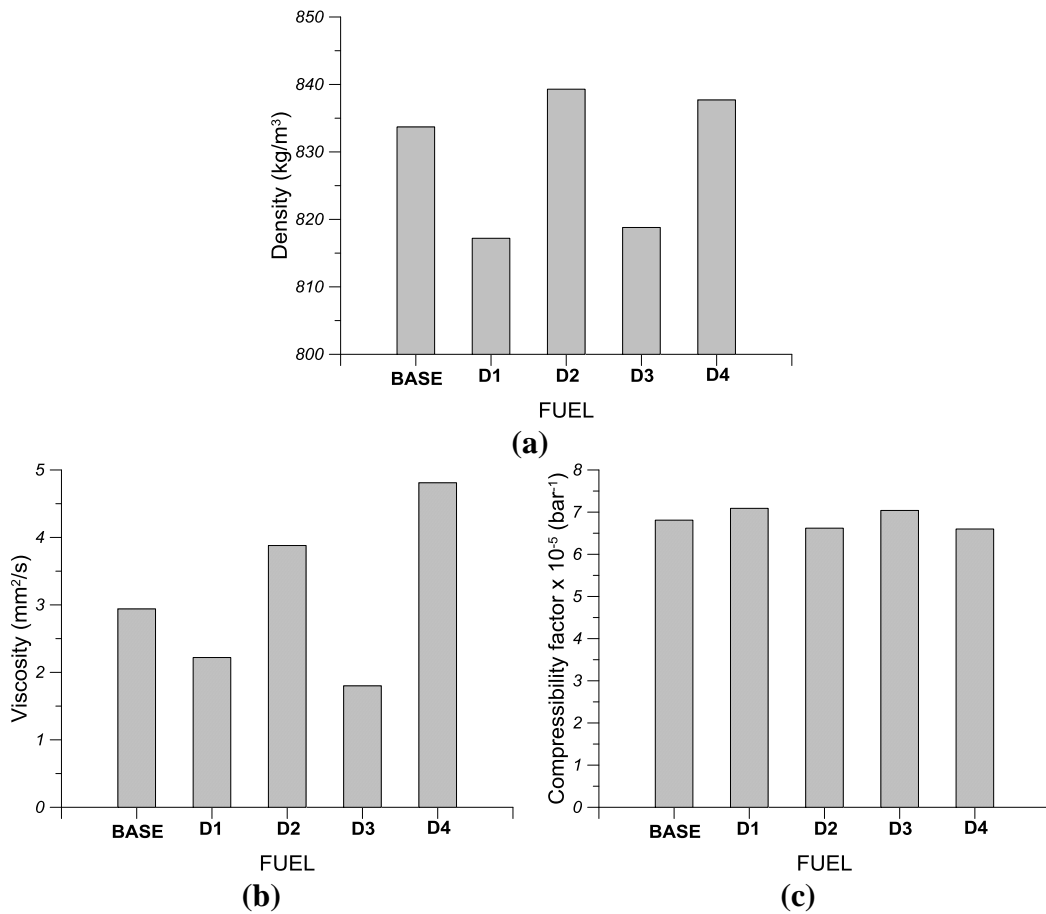


FIGURE 5. Comparison of (a) density, (b) viscosity and (c) compressibility factor of the test fuels BASE, D1, D2, D3 and D4, which are examined in the present study [21]

DESCRIPTION OF THE DIESEL ENGINE EXPERIMENTAL APPARATUS AND THE TESTING PROCEDURE

An experimental installation was installed in the past at the Internal Combustion Engines Laboratory of National Technical University of Athens, Greece based on a single cylinder DI diesel engine coupled with a hydraulic dynamometer. In the specific experimental apparatus devices for controlling diesel engine operation and monitoring its operational parameters were installed. The experimental diesel engine (“Lister LV1”) of this installation is a four stroke, air cooled naturally-aspirated single-cylinder high-speed DI diesel engine, which is equipped with a bowl-in-piston. “Lister LV1” diesel engine has a cylinder bore of 0.08573 m, a piston stroke of 0.08255 m and the connecting rod length is 0.1885 m [1,20,22]. The compression ratio of “Lister LV1” diesel engine is 17:1 and its nominal speed range varies from 1000 to 3000 rpm. Diesel fuel is injected in “Lister LV1” engine through a three-hole injector (nozzle orifice diameter 250 μ m), which is located at the center of the combustion chamber and its opening pressure is 180 bar. “Lister LV1” engine is coupled with a Heenan & Froude hydraulic dynamometer [1,20,22].

The main measuring equipment comprised of an Alcock air flow meter (viscous type), fuel tank and flow-meter for measuring engine fuel consumption, thermocouples for recording exhaust gas temperature, intake air temperature, lubricant oil temperature and engine coolant temperature, a magnetic pickup for recording TDC position, a crankshaft rotational speed indicator and a piezoelectric transducer for measuring in-cylinder pressure. A similar piezoelectric transducer was fitted to the high-pressure fuel line between pump and injector close to the injector for monitoring fuel injection pressure. It was also used a fast data acquisition system for recording cylinder pressure, injection pressure and TDC position measurements and storing them in a PC [1,20,22].

Engine tests were performed with test fuels BASE, D1, D2, D3 and D4 at 2500 rpm and at four engine loads namely 20, 40, 60 and 80% of full load at 2500 rpm. All tests were carried out using constant static injection timing (26degCA BTDC) of the fuel injection system to avoid variations in fuel injection commencement inside the combustion chamber due to static injection timing variations. Also a serious effort was made all engine tests to be performed without noticeable variations of intake air temperature and lubricant oil temperature as a method for avoiding engine operation fluctuations and most importantly, engine loading variations. Specifically, all engine tests were performed for intake air temperature of 24°C and air pressure of 1.01 bars. Engine testing procedure comprised of the following two steps [1,20,22]:

1. Initially engine tests were carried out at 2500 rpm and at all engine loads (20, 40, 60 and 80% of full load) using only BASE fuel. At each operating point, various engine operational parameters were recorded such as fuel consumption, exhaust gas temperature, intake temperature and flow mass rate, cylinder pressure and injection pressure. Hence, using this testing methodology, the engine baseline operation for the reference “BASE” fuel was constituted.
2. The previous testing procedure was repeated for the same engine operating conditions for each one of the test fuels D1, D2, D3 and D4.

As already mentioned the experimental single-cylinder DI diesel engine considered in the present study (“Lister LV1”) is directly connected to a proper hydraulic dynamometer. The hydraulic brake manufacturer provided the following equation for the calculation of engine brake power [1,20,22]:

$$P_e (CV) = \frac{W (kg) \times RPM}{1500} \quad (1)$$

where P_e is the engine's brake power in CV, W is the brake's dynamometer load indication in kg and RPM is the rotational speed of the engine – brake connecting shaft.

Engine intake air flow rate was measured using an Alcock measuring device, which measures intake pressure variation and it has been calibrated for air temperature of 20°C. Hence, the intake air volume flow rate is calculated using the following relation, which has been derived according to a proper diagram accompanying the Alcock measuring device [1,20,22]:

$$\dot{V}_A \left(\frac{m^3}{h} \right) = 1.698 \times (\text{Alcock value (cm)}) \quad (2)$$

During experiments the laboratory temperature T_{room} and the barometric pressure p_{room} were recorded and they were used for calculating the engine intake air mass flow rate using measured intake air volume flow rate and the ideal gas equation of state [1,20,22]:

$$\dot{m}_A \left(\frac{kg}{h} \right) = \frac{p_{room}}{RT_{room}} \times \dot{V}_A \left(\frac{m^3}{h} \right) \quad (3)$$

A constant volume tube of 50 ml is used for measuring engine fuel consumption. The measurement of fuel consumption is based on the measurement of time required for the evacuation of the 50 ml diesel oil tube from the engine. Consequently, the fuel consumption in kg/h is calculated using the following relation [1,20,22]:

$$\dot{m}_f \left(\frac{kg}{h} \right) = \left[\frac{50 (ml) \times \rho_f \left(\frac{kg}{m^3} \right) \times 10^{-6} \left(\frac{m^3}{ml} \right) \times 3600 \left(\frac{s}{h} \right)}{\Delta t (s)} \right] \quad (4)$$

where ρ_f is fuel density and Δt in sec is the time required for the evacuation of the 50 ml diesel fuel tube during engine operation.

DESCRIPTION OF THE DIESEL ENGINE EXPERIMENTAL DATA PROCESSING MODEL

A computational model was developed during a diploma thesis in Hellenic Naval Academy for processing initial experimental signals for cylinder pressure, injection pressure and TDC position previously obtained during an engine testing procedure in “Lister LV1” using test fuels BASE, D1, D2, D3 and D4. Engine tests were performed at 2500 rpm and at four engine loads namely 20, 40, 60 and 80% of full engine load. The developed model was used to process the aforementioned experimental signals for generating the average cylinder pressure – crank angle profile and the average fuel injection pressure – crank angle profile and then to use these profiles for calculating the main performance and combustion characteristics of the “Lister LV1” for all test fuels examined. Of particular importance is the description of the mathematical process adopted from the developed model to process the initial cylinder pressure, injection pressure and TDC position signals over all obtained complete engine cycles for generating the average

cylinder pressure and the average injection pressure profiles for each examined engine operating point and each examined test fuel.

Hence, during the engine testing procedure and at each engine operating point after setting the rack position in the fuel pump and after securing constant operating conditions the following signals obtained from the engine were recorded in a personal PC through a fast data acquisition system: The cylinder pressure signal, the injection pressure signal and the TDC position signal. In Figure 6 are shown the characteristic signals of cylinder pressure (Figure 6(a)), injection pressure (Figure 6(b)) and TDC position (Figure 6(c)) as obtained from the diesel engine during testing procedure of BASE fuel at 2500 rpm and 80% of full load. It should be mentioned that in the specific experimental investigation at least 10 consecutive engine cycles were recorded at each engine operating point as evidenced also from Figures 6(a)-(c).

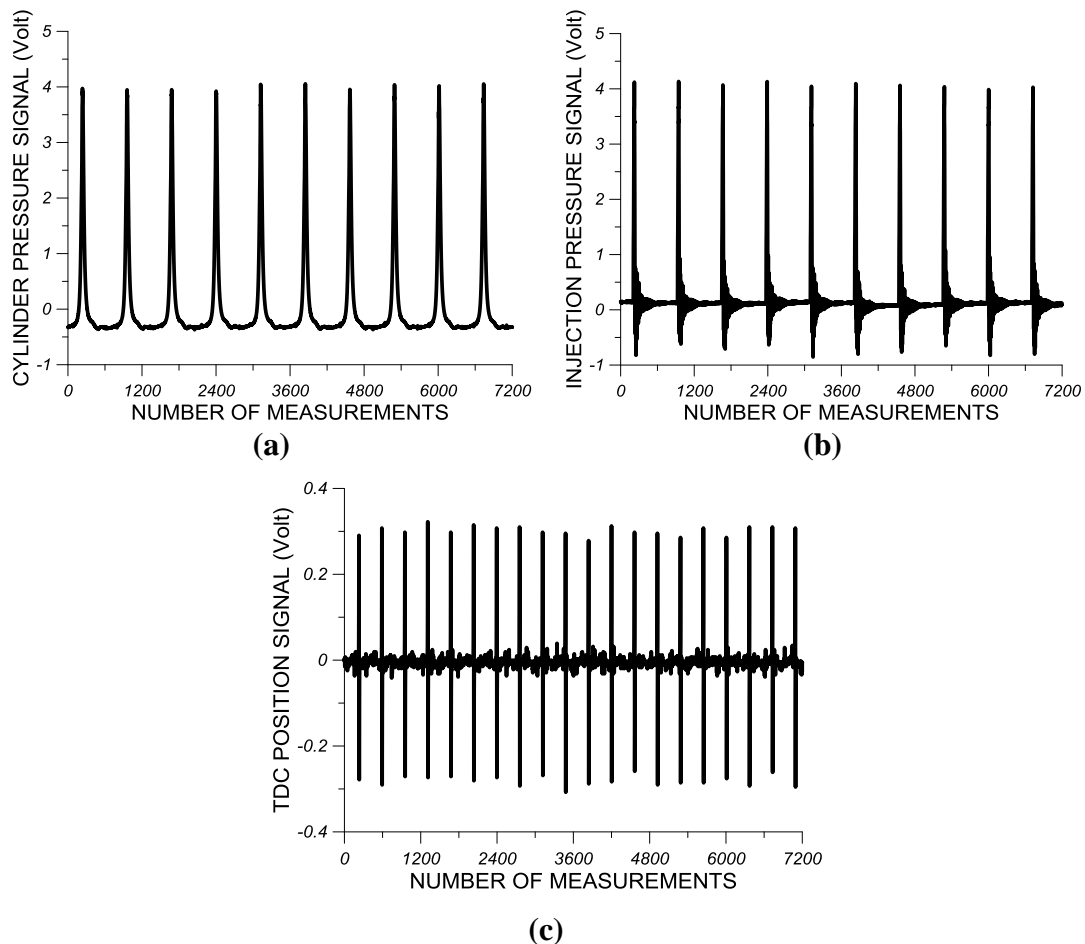


FIGURE 6. Initial signals of (a) cylinder pressure, (b) fuel injection pressure and (c) TDC position as obtained from the “Lister LV1” engine during testing procedure for test fuel BASE at 2500 rpm and at 80% of full engine load

As evidenced from Figure 7, TDC position signal undergoes at a specific acquisition point an abrupt rise and immediately afterwards a steep reduction around zero. The cross-section point of the TDC position curve which connects the local maximum with the local minimum of the TDC position signal with the zero horizontal line corresponds to the piston immobilization position at TDC (Figure 8). The number of measurements between two consecutive positions at

which the TDC position signal becomes equal to zero provides the number of measurements, which were actually received during a complete engine cycle.

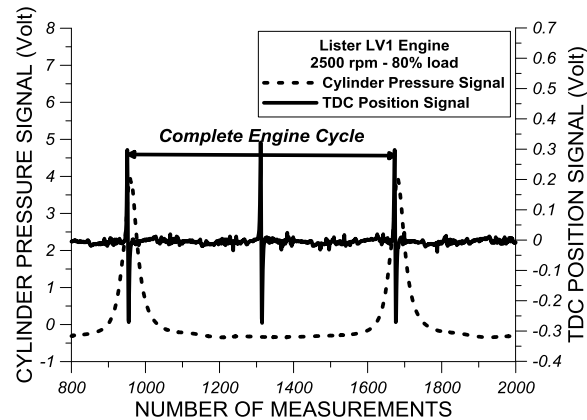


FIGURE 7. Graphical explanation of the procedure followed for the determination of the number of complete engine cycles. Experimental data are given for “Lister LV1” engine at 2500 rpm and at 80% of full engine load using BASE fuel.

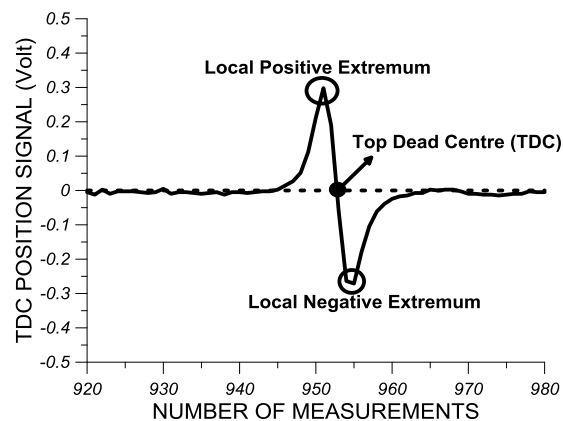


FIGURE 8. Graphical explanation of TDC position determination per engine cycle. Experimental data are given for “Lister LV1” engine at 2500 rpm and at 80% of full engine load using BASE fuel.

At the point that the TDC position signal becomes equal to zero it can be matched a value of crank angle (CA) equal to 180 degCA or 540 degCA (it is assumed that the crank angle is equal to 0 degCA when the piston is at BDC). This procedure provides us with the opportunity to correlate the measured values of cylinder pressure and injection pressure with specific crank angles for a complete engine cycle. Having specified the points at which the TDC position signal becomes equal to zero, we can then determine the points that correspond to TDC positions during combustion (180degCA) since all other TDC position zero points correspond to the gas exchange period of an engine cycle (540 degCA). The TDC position zero points that assigned to 180 degCA are those that correspond to the peak values of the cylinder pressure signal.

Having determined the TDC position points and knowing the number of measurements at each obtained complete engine cycle it can be calculated the actual acquisition step, which is equal to the ratio of the theoretical number of measurements, which are supposed to be obtained during a complete four-stroke engine cycle in the case the acquisition step was equal to 1 degCA (720 measurements) to the actual number of measurements obtained during engine tests at a complete engine cycle (e.g. 722 measurements). Small deviations between the theoretical and the

actual total number of measurements can be ascribed to the fact the engine crankshaft speed indicates small deviations compared to the specified value during engine tests.

At this point it should be underlined that all three signals of TDC position, cylinder pressure and injection pressure are not received at exactly the same time instant from the fast acquisition card. In other words, there is a time phase between the three recorded signals. Specifically, during an acquisition step are recorded all three signals. Hence, the time phase between two consecutive signals is equal with 1/3 of the acquisition step e.g. if the acquisition step is set to 1 degCA then at the first 1/3 of the degree is recorded the cylinder pressure signal, the second 1/3 of the degree is recorded the injection pressure signal and the final 1/3 of the degree is recorded the TDC position signal.

Having determined the measurement points of each obtained complete engine cycle corresponding to 180 degCA, we then determine the rest of the complete engine cycle points by moving each time with the actual acquisition step from one point to another and by performing linear interpolation between corresponding values of cylinder pressure and injection pressure signals. With this process the measured values of cylinder pressure and injection pressure are derived for all recorded complete engine cycles. The values of cylinder pressure and injection pressure for each complete engine cycle are then used to calculate the average cylinder pressure – crank angle and the average injection pressure – crank angle profiles. The determination of the average cylinder pressure – crank angle and the average injection pressure – crank angle profiles provides us with the opportunity to calculate the engine performance parameters of the examined diesel engine such as indicated work and power, IMEP, ISFC, gross and net heat release rate, ignition delay and combustion duration. The derivation of individual cylinder pressure and injection pressure profiles for all recorded complete engine cycles and their processing for performance and heat release rate analysis can be proven quite useful in engine cases that there is cyclic variation on performance and combustion characteristics between consecutive engine cycles.

Calculation of Indication Power

Having calculated the average cylinder pressure profile over all complete engine cycles of the examined DI diesel engine for which cylinder pressure measurements were received it can be then calculated the indicated work per cylinder and through this the cylinder indicated power. The calculation of the indicated work requires the transformation of the average cylinder pressure – crank angle diagram to a cylinder pressure – instantaneous cylinder volume diagram in order to calculate the effective area between thermodynamic variation curves, which corresponds to the indicated work. Cylinder indicated work corresponds to the net useful mechanical work generated by one cylinder and it is equal to all positive expansion works minus all negative compression works. The instantaneous in-cylinder volume is calculated using the following relation:

$$V(\varphi) = V_c + \frac{\pi D^2}{4} x(\varphi) \quad (5)$$

where V_c is the dead volume, D is the cylinder bore and $x(\varphi)$ is the instantaneous piston distance from TDC, which is calculated according to the following relation:

$$x(\varphi) = r \cdot (1 - \cos \varphi) + L \cdot \left[1 - \sqrt{1 - \lambda^2 \cdot \sin^2 \varphi} \right] \quad (m) \quad (6)$$

where r is the crank radius, L is the connecting rod length and λ is the ratio of the crank radius to conn rod length. Consequently, using Eqs (5) and (6) the instantaneous piston distance from TDC and the instantaneous volume can be calculated for each one of the 720 degrees crank angle of a full engine cycle. Hence, through this the aforementioned it is facilitated the transition from a measured initial cylinder pressure – crank angle degree diagram to a measured cylinder pressure – instantaneous volume diagram. Indicative cylinder pressure – crank angle diagram and its corresponding cylinder pressure – instantaneous cylinder volume diagram are given in Figures 9(a) and 9 (b) respectively.

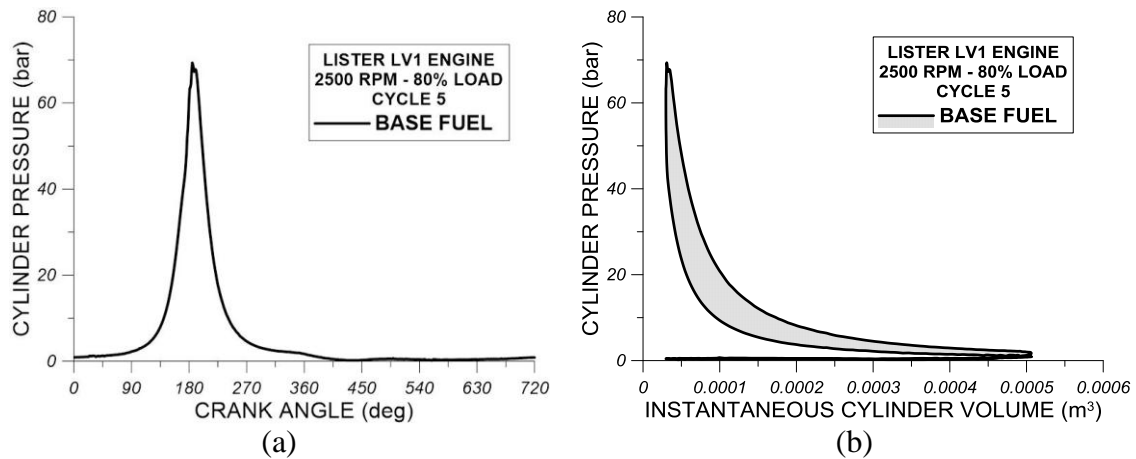


FIGURE 9. (a) Measured cylinder pressure – crank angle degree profile and (b) Same measured cylinder pressure – instantaneous cylinder volume profile. Experimental results are given for “Lister LV1” diesel engine at 2500 rpm and at 80% load. Cylinder pressure profiles correspond to 5th obtained complete engine cycle using BASE fuel.

It is worth to mention that as evidenced from the observation of the Figure 9(b) the exchanged work during gas exchange process (air induction and exhaust gas forced extraction) is very small compared to exchanged work of the closed engine cycle (filled area in Figure 9(b) - all valves are closed) and thus it does not contribute significantly to the calculation of the cylinder indicated work. In the present work the numerical method adopted for the calculation of the work exchanged area of the cylinder pressure – cylinder volume diagram is the trapezoidal method according to which the cylinder indicated work is calculated using the following relation [35-38]:

$$W_i = \sum_{i=1}^{719} (p_i + p_{i+1}) \frac{(V_{i+1} - V_i)}{2} \quad (7)$$

It should be mentioned here that the accuracy of the trapezoidal method as an numerical integration method has been compared with other more analytical integration methods such as the interpolation method of cylinder pressure and cylinder volume values using piecewise polynomials and then the numerical integration of splines functions. From this comparison it has been found that the deviation in the calculation of indicated work using trapezoidal method and the analytical method using piecewise polynomials is not significant [35-38]. The issue of numerical integration is clarified since it is essential for the accurate calculation of the indicated work. Having calculated the indicated work the indicated power can be calculated from the following relation:

$$P_i(W) = W_i(J) \frac{RPM}{120} \quad (8)$$

Heat Release Rate Analysis

The calculation of the heat release rate is of high importance in diesel engines since from its processing very important information can be extracted for the initiation and the completion of the combustion, the quality of combustion, the fuel burning rate and the duration and the intensity of the premixed and the diffusion-controlled in-cylinder combustion. Hence, by differentiating the first law of thermodynamics for a closed system (i.e. trapped in-cylinder gas when all valves are closed) and the ideal gas equation of state and by also considering constant in-cylinder gas mass (blow-by losses through piston rings are negligible) the following equations can be derived [39-41]:

$$\begin{aligned} \frac{dQ_b}{d\phi} - \frac{dQ_l}{d\phi} &= p \frac{dV}{d\phi} + mc_v \frac{dT}{d\phi} \\ p \frac{dV}{d\phi} + V \frac{dp}{d\phi} &= mR \frac{dT}{d\phi} \end{aligned} \quad (9)$$

In the previous relation the term $\frac{dQ_b}{d\phi}$ is called Total or Gross Heat Release Rate whereas the difference $\frac{dQ_b}{d\phi} - \frac{dQ_l}{d\phi}$ is called Net Heat Release Rate and it can be estimated using the following relation [32,33,39-41]:

$$\frac{dQ_b}{d\phi} - \frac{dQ_l}{d\phi} = \left(1 + \frac{c_v}{R}\right) p \frac{dV}{d\phi} + \frac{c_v}{R} V \frac{dp}{d\phi} \quad (10)$$

The term $\frac{dQ_l}{d\phi}$ corresponds to the instantaneous in-cylinder gas heat transfer losses, which are transferred to the cylinder walls mainly through heat convection and secondarily, after combustion initiation, through additional heat radiation due to flame development and combustion-released burning particles. For this reason, in the present analysis the cylinder instantaneous heat losses are calculated using the semi-empirical Annand model, which takes into account both convection and radiation heat transfer mechanisms as evidenced from the following relation [32,33,39-41]:

$$\dot{q} = a_c \frac{\lambda_g}{D} Re^{0.7} (T_g - T_w) + c\sigma(T_g^4 - T_w^4) \quad (11)$$

where:

- T_g is the average in-cylinder gas temperature at each crank angle. The instantaneous gas temperature is calculated by applying the ideal gas equation of state using the measured in-cylinder temperature and the instantaneous in-cylinder volume.
- T_w is the cycle-averaged temperature of the cylinder walls, which as evidenced from previous experimental heat transfer studies in the examined diesel engine can be considered equal to 200°C.

- σ is the Stephan- Boltzmann constant ($5.67 \times 10^8 \text{ W/m}^2\text{K}^4$).
- λ_g is the in-cylinder gas thermal conductivity coefficient, which is calculated through a polynomial correlation as function of the instantaneous in-cylinder gas temperature.
- α_c is a convection term constant, which as observed from many heat transfer studies in various types of diesel engines varies between 0.3 and 0.4. In the present analysis the value of α_c was calibrated at each operating condition in order the following relation to be valid:

$$\dot{m}_f = \dot{Q}_{b,tot} / LHV \quad (12)$$

where \dot{m}_f is the measured fuel injected quantity per engine cycle, $\dot{Q}_{b,tot}$ is the total gross heat released during an engine cycle and LHV is the examined fuel lower heating value.

- Re is the Reynolds dimensionless number, which can be derived from the following equation:

$$Re = \frac{D \cdot s \cdot RPM}{30 \cdot \nu_g} \quad (13)$$

where ν_g is the kinematic viscosity of the in-cylinder gas, which is calculated through the previous calculation of the dynamic viscosity μ_g using a polynomial correlation and the in-cylinder gas density at each crank angle.

The accurate calculation of the combustion duration during an engine cycle is not easy and simple since the precise determination of the end of combustion is quite difficult. This is due to the fact the heat release rate curve indicates fluctuations towards the end of combustion and thus the precise end of combustion is quite difficult to be spotted. For this reason, in many diesel combustion investigations, various combustion durations are defined, which correspond to different proportions of fuel injected mass such as:

- CA5, which correspond to the combustion duration in crank angle degrees of the 5% of fuel injected mass,
- CA50, which correspond to the combustion duration in crank angle degrees of the 50% of fuel injected mass and
- CA90 or CA95, which correspond to the combustion duration in crank angle degrees of the 90% or 95% respectively of fuel injected mass.

The calculation process of combustion duration is facilitated considerably with the development of the diagram of cumulative heat release rate profile as function of crank angle. The total thermal power, which is expected to be released if the total fuel injected mass is burnt is:

$$\dot{Q}_{b,tot} = \dot{m}_f \cdot LHV \quad (14)$$

Having calculated the instantaneous gross heat release rate, the cumulative gross heat release rate can be calculated by summing the elementary heat release rates at each crank angle degree:

$$Q_b(\varphi) = \sum_{i=1}^{360} dQ_b(\varphi) \quad (15)$$

The computational model can be used for experimental data processing of either four-stroke or two-stroke diesel engines, where measurements of cylinder pressure, injection pressure and TDC position (three sensors) were obtained or it can be used for processing only measurements of cylinder pressure and TDC position (two sensors). Also it should be underlined that most of the input data of the computational model can be found in any case of examined diesel engine from engine manufacturer manual, from the manufacturers of piezoelectric transducers for

cylinder pressure and injection pressure transducers and from the fuel preparation entities. Hence the developed experimental data processing model can provide reliable results for the following diesel engine performance and combustion characteristics:

- Cylinder pressure – crank angle and injection pressure – crank angle profiles for each measured complete engine cycle at a certain engine operating point
- Average cylinder pressure – crank angle and injection pressure – crank angle profiles over all measured complete engine cycles at a certain engine operating point
- Indicated work and power
- Indicated mean effective pressure (IMEP) per engine cycle and per average cylinder pressure profile at a certain engine operating point
- Indicated specific fuel consumption (ISFC)
- Engine mechanical efficiency
- Brake specific fuel consumption (BSFC)
- Actual acquisition step in crank angle degrees
- Actual engine speed
- Instantaneous gross and net heat release rates for each measured cycle cylinder pressure profile and for the average cylinder pressure profile at a certain engine operating point
- Instantaneous heat transfer loss rate for each measured cycle cylinder pressure profile and for the average cylinder pressure profile at a certain engine operating point
- In-cylinder gas temperature – crank angle profile for each measured cycle cylinder pressure profile and for the average cylinder pressure profile at a certain engine operating point
- Cumulative gross and net heat release rates for each measured cycle cylinder pressure profile and for the average cylinder pressure profile at a certain engine operating point
- Cumulative heat loss rate for each measured cycle cylinder pressure profile and for the average cylinder pressure profile at a certain engine operating point
- Instantaneous and cumulative fuel burning mass rates for the average cylinder pressure profile at a certain engine operating point
- Ignition angle and ignition delay for the average cylinder pressure profile at a certain engine operating point
- Peak cylinder pressure and corresponding crank angle for each measured cycle cylinder pressure profile and for the average cylinder pressure profile at a certain engine operating point
- Combustion durations of 5%, 25%, 50%, 90% and 100% of the total injected fuel mass for each measured cycle cylinder pressure profile and for the average cylinder pressure profile at a certain engine operating point
- Average injection pressure, dynamic injection timing (i.e. Start of Injection – SOI), peak injection pressure and fuel injection duration for the average cylinder pressure profile at a certain engine operating point

RESULTS AND DISCUSSION

Experimental Results for Cylinder Pressure, Injection Pressure, Heat Release Rates and Heat Loss Rates for Test Fuels D1 and D2

Figure 10 shows a comparison of experimental results of cylinder pressure between test fuels D1 and D2 for the first operation cycle (Figure 10(a)), the fifth operation cycle (Figure 10(b)) and the ninth operation cycle (Figure 10(c)). Experimental results for cylinder pressure profiles shown in Figure 10(a)-(c) refer to engine tests performed at 2500 rpm and at 80% of full load. It is reminded that during experimental measurements in DI diesel engine “Lister LV1” with all test fuels examined in this study, cylinder pressure and injection pressure measurements were received for ten consecutive engine cycles. According to Figure 10(a) there are no substantial variations in cylinder pressure traces between test fuels D1 and D2 at all engine cycle phases. From the observation of Figure 10(b) it can be concluded that test fuel D1 indicates relatively lower cylinder pressure values in the fifth obtained engine cycle during combustion phase around TDC whereas cylinder pressure differences between fuels D1 and D2 during compression and expansion stroke are insignificant. In other words, according to cylinder pressure results of the fifth cycle of test fuels D1 and D2 (Figure 10(b)), test fuel D2 is ignited slightly faster than the test fuel D1 and this results in a more rapid cylinder pressure increase for test fuel D1 compared to D2 from ignition point and further on during combustion phase around TDC. A similar behavior between test fuels D1 and D2 is observed at Figure 10(c), which shows experimental results for cylinder pressure. Specifically, according to Figure 10(c), test fuel D2 appears to ignite slightly faster compared to D1 and this leads to higher cylinder pressures during combustion and also during late expansion. The slightly faster combustion initiation for test fuel D2 at the fifth and the ninth obtained engine cycles compared to test fuel D1 is possibly attributed to the relatively higher cetane number of fuel D2 compared to fuel D1. From the observation of the cylinder pressure profiles of Figures 10(a)-(c) it results that the effect of fuel properties on the measured cylinder pressure differs slightly from cycle to cycle and this means that in another cycle the effect is slightly apparent while in another cycle it can be insubstantial.

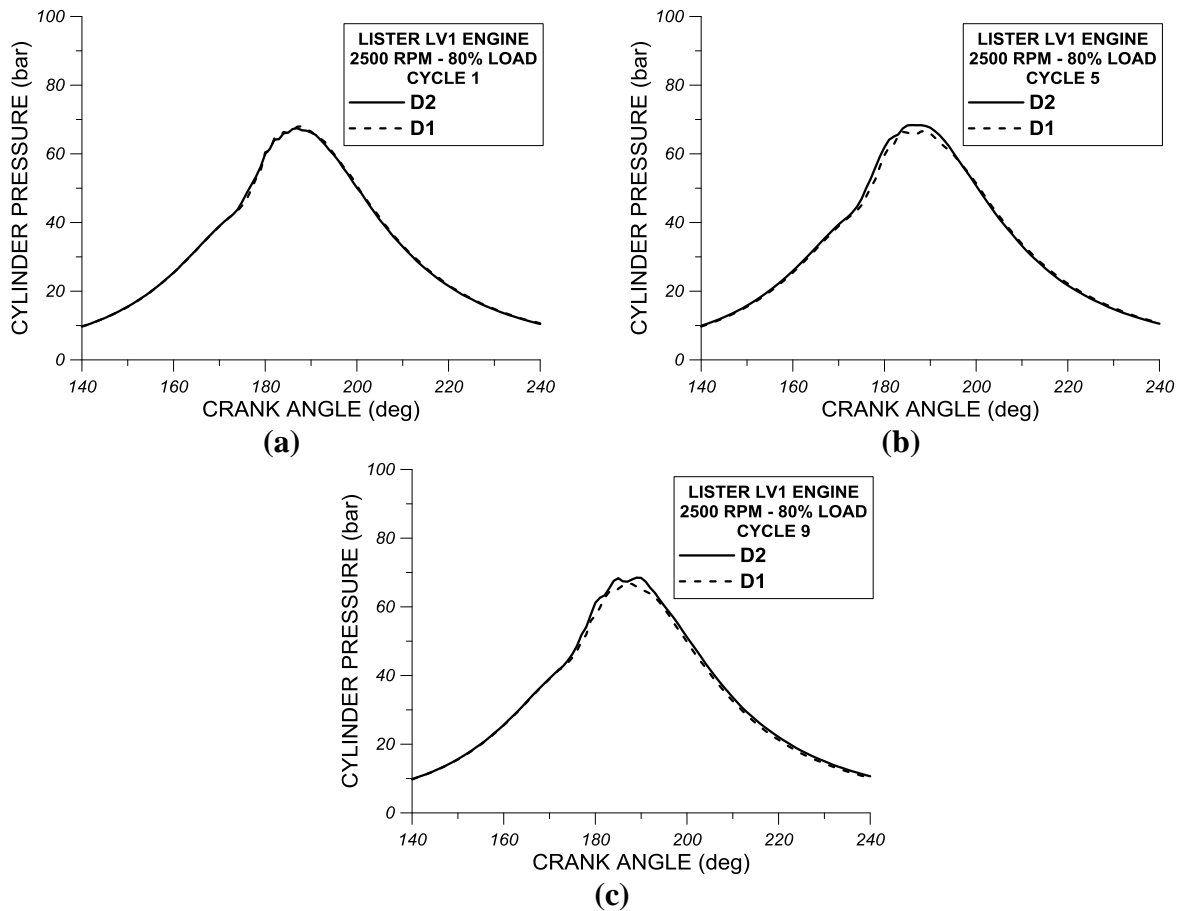


FIGURE 10. Comparison of experimental results for cylinder pressure of (a) the first operation cycle and (b) the fifth operation cycle and (c) the ninth operation cycle for test fuels D1 and D2 at 2500 rpm and at 80% of full load. Experimental results are given for high-speed single-cylinder DI diesel engine “Lister LV1”

Figure 11 shows comparative test results of the fuel injection pressure between D1 and D2 conventional fuels from the first cycle (Figure 11(a)), the fifth cycle (Figure 11(b)) and the ninth cycle (Figure 11(b)). The experimental results for the injection pressure of Figures 11(a)-(c) refer to experimental measurements obtained from “Lister LV1” at 2500 rpm and 80% of the full load. From the observation of Figures 11(a)-(c) it can be evidenced that at all engine cycles examined (first, fifth and ninth) that there is an earlier initiation of fuel injection pressure for fuel D2 compared to fuel D1. The more abrupt injection pressure rise of fuel D2 compared to D1 at all examined engine cycles results also to higher peak injection pressures for fuel D2 compared to D1. The earlier initiation and the steeper rise of the injection pressure for fuel D2 compared to fuel D1 that occur at all examined complete engine cycles can possibly be attributed to the relatively lower compressibility factor of fuel D2 compared to the one of fuel D1 having acknowledged that the compressibility factor directly affects the compressible fuel flow and thus, the fuel pressure in the high pressure fuel line connecting the fuel pump with the fuel injector.

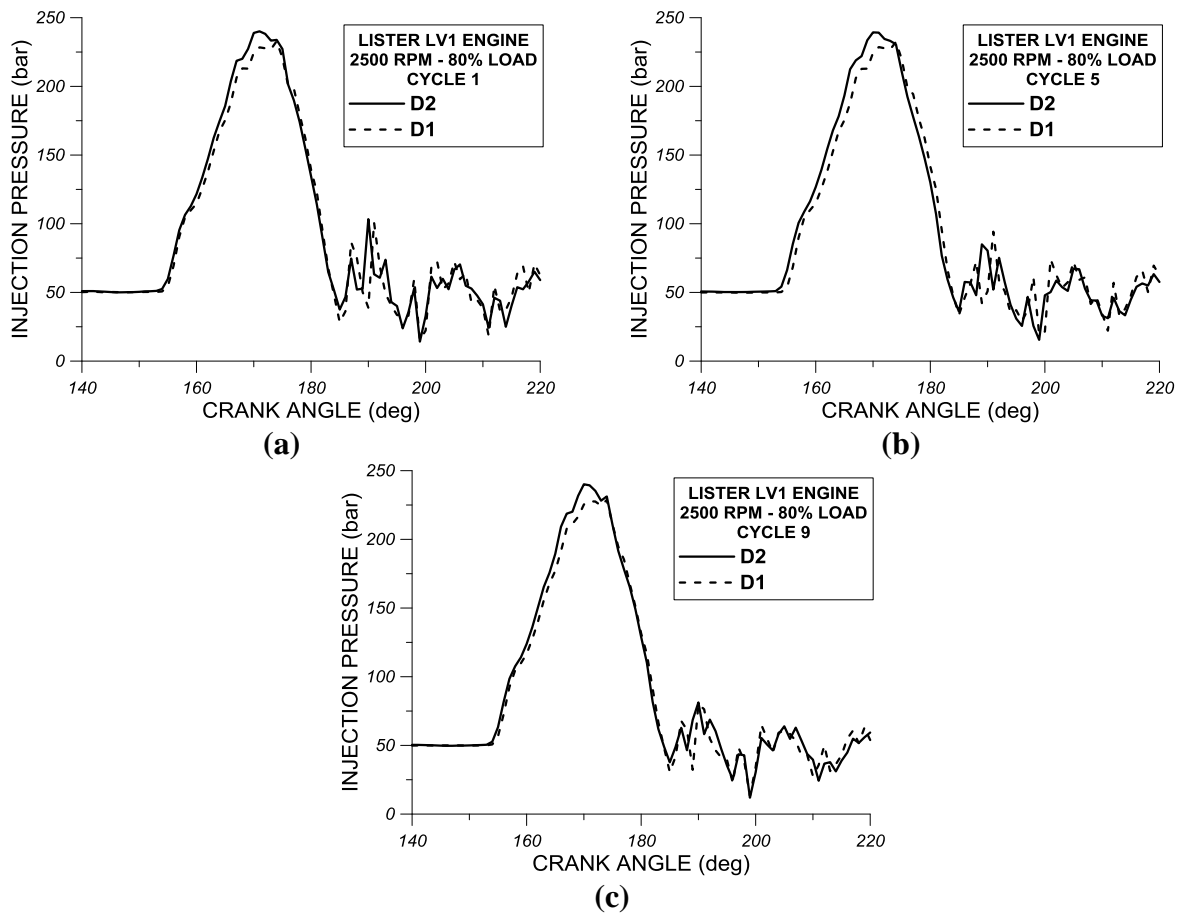


FIGURE 11. Comparison of experimental results for injection pressure of (a) the first operation cycle, (b) the fifth operation cycle and (c) the ninth operation cycle for test fuels D1 and D2 at 2500 rpm and at 80% of full load. Experimental results are given for high-speed single-cylinder DI diesel engine “Lister LV1”

Figure 12(a) shows comparative experimental results of the instantaneous gross heat release rate between conventional fuels D1 and D2 at 2500 rpm and 80% of full load. Also in Figure 12(b) are presented comparative experimental results of the instantaneous heat release rate between conventional fuels D1 and D2 at 2500 rpm and 80% of the full load. Figure 12(c) shows comparative experimental results of the instantaneous heat loss rate from the cylinder at 2500 rpm and 80% full load for D1 and D2 fuels. It is recalled here that the calculation of the instantaneous gross and net heat release rate into the cylinder has been done assuming a uniform distribution of the pressure and temperature of the processing medium within the cylinder at each crank angle (one-zone model). The observation of Figures 12(a)-(b) shows the relatively earlier start of combustion for fuel D2 than fuel D1 (the point where the net heat release rate is positive for the first time). The earlier start of combustion for the fuel D2 compared to fuel D1 is accompanied by a steeper increase in both gross and net heat release rates within the cylinder. The earlier start of combustion for fuel D2 can be possibly attributed to the relatively higher cetane number of that fuel compared to the one fuel D1. However, the intensity of the premixed combustion for the fuel D2 is lower than the corresponding intensity of fuel D1 while the intensity of the diffusion-controlled combustion phase is approximately the same for both fuels D1 and D2. The observation of Figure 12(c) shows that the values of instantaneous heat loss rate for test fuel D1 are higher compared to the ones of test fuel D2 during combustion and late

expansion phases. This observation can be ascribed to the relatively higher gross heat release rate values of fuel D1 compared to fuel D2 observed in Figure 13(a) during premixed and diffusion-controlled combustion.

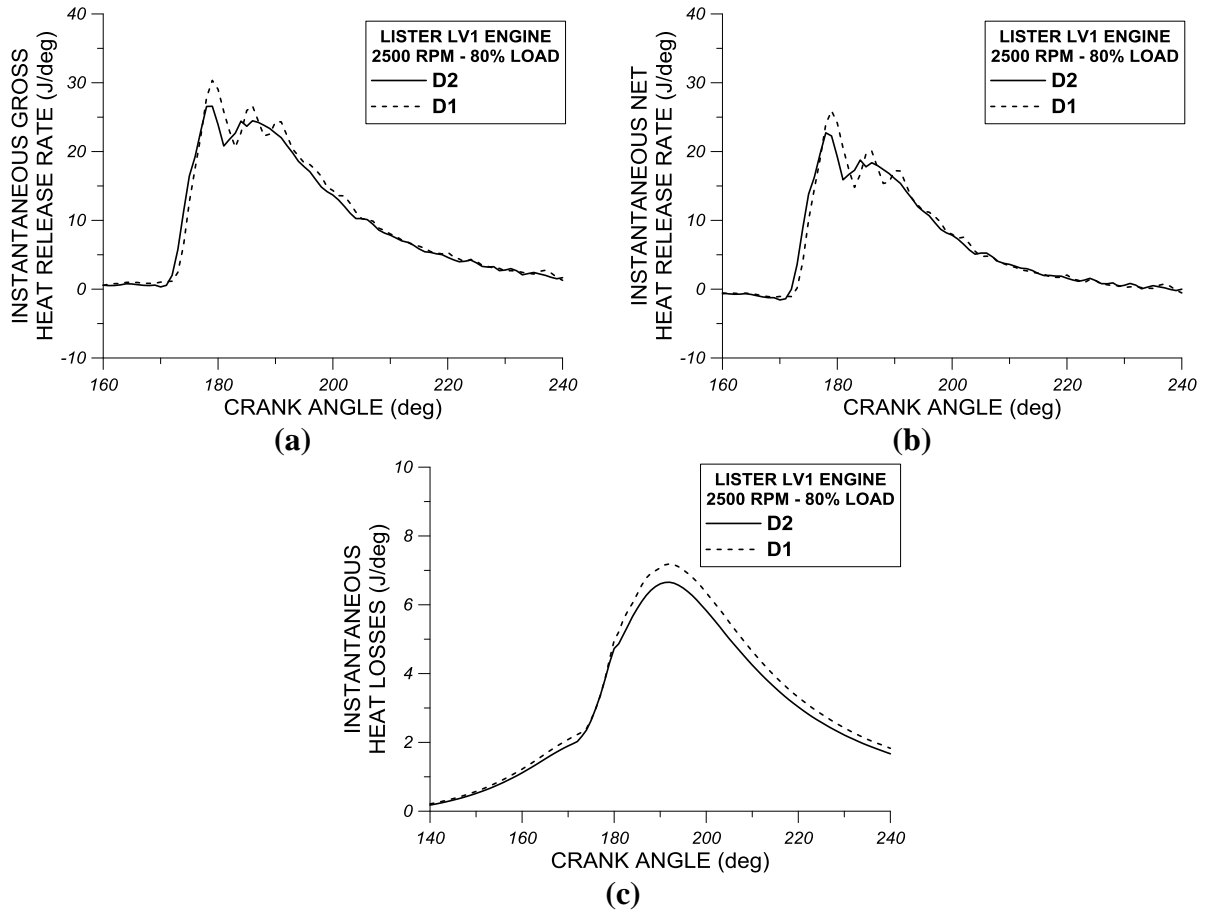


FIGURE 12. Comparison of experimental results for (a) the instantaneous gross heat rate, (b) the instantaneous net heat release rate and (c) the instantaneous heat loss rate inside engine cylinder for test fuels D1 and D2 at 2500 rpm and at 80% of full load. Experimental results are given for high-speed single-cylinder DI diesel engine “Lister LV1”

Figure 13(a) shows comparative experimental results of the cumulative gross heat release rate from “Lister LV1” engine between conventional D1 and D2 fuels at 2500 rpm and 80% of full load. Also in Figure 13(b) are presented comparative experimental results for the cumulative net heat release rate from “Lister LV1” engine between the conventional fuels D1 and D2 at 2500 rpm and 80% of the full load and finally in Figure 13(c) are presented comparatively experimental results of the cumulative heat loss rate “Lister LV1” engine at 2500 rpm and 80% of the full load for fuels D1 and D2. According to Figure 13(a) the use of fuel D1 results in slightly higher cumulative gross heat release rates of combustion than the D2 fuel under the same conditions. This small difference mainly in the phase of expansion after the TDC is probably due to the relatively higher pressure values and hence the cylinder gas temperature observed above for the fuel D1 compared to fuel D2. Deviations between fuels D1 and D2 in the cumulative net heat rate (see Figure 13(b)) are insignificant. The observation of Figure 13(c) shows that the fuel

D1 demonstrates higher cumulative heat loss rates compared to fuel D2 mainly in the phase of expansion after the TDC because of the relatively higher pressures and cylinder gas temperatures as seen above for the fuel D1 relative to the fuel D2.

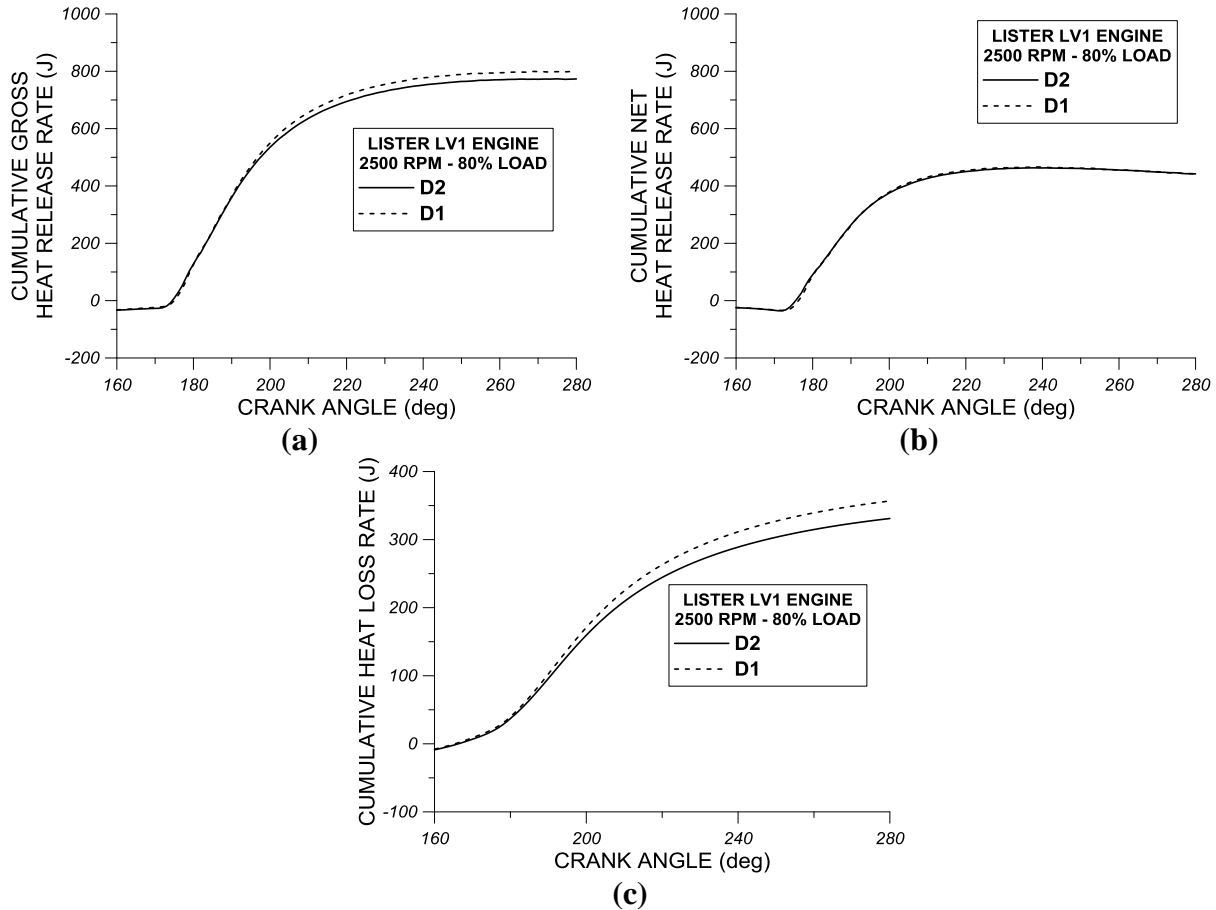


FIGURE 13. Comparison of experimental results for (a) the cumulative gross heat release rate, (b) the cumulative net heat release rate and (c) the cumulative heat loss rate for test fuels D1 and D2 at 2500 rpm and at 80% of full load. Experimental results are given for high-speed single-cylinder DI diesel engine “Lister LV1”.

Experimental Results for Cylinder Pressure, Injection Pressure, Heat Release Rates and Heat Loss Rates for Test Fuels D3 and D4

Figures 14(a)-(c) show comparative experimental results of cylinder pressure traces between conventional fuels D3 and D4 from the first operation cycle (Figure 14(a)), the fifth operation cycle (Figure 14(b)) and the ninth operation cycle (Figure 14(c)). It is reminded that during experimental measurements in DI diesel engine “Lister LV1” with all test fuels examined in this study, cylinder pressure and injection pressure measurements were received for ten consecutive engine cycles. The experimental results for cylinder pressure shown in Figures 14(a)-(c) refer to experimental measurements performed at 2500 rpm and 80% of the full load. According to Figure 14(a) it appears that the fuel D4 shows slightly higher values of cylinder pressure after ignition in the compression phase, during combustion phase around TDC and during late expansion compared to the fuel D3. The earlier start of combustion for the fuel D4 compared to

the fuel D3 can possibly be ascribed to the relatively higher value of cetane number of fuel D4 compared to corresponding value of fuel D3. The same behavior in measured cylinder pressure profiles between test fuels D3 and D4 is exhibited for the fifth operation cycle in Figure 14(b). In contrast, as shown in Figure 14(c), the differences in cylinder pressure between test fuels D3 and D4 in the ninth operation cycle are insignificant. Hence, it can be concluded from most of the examined engine cycles that the higher cetane number of fuel D4 compared to fuel D3 results in an earlier combustion initiation and slightly higher cylinder pressures during combustion phase around TDC and also, in slightly higher peak cylinder pressures.

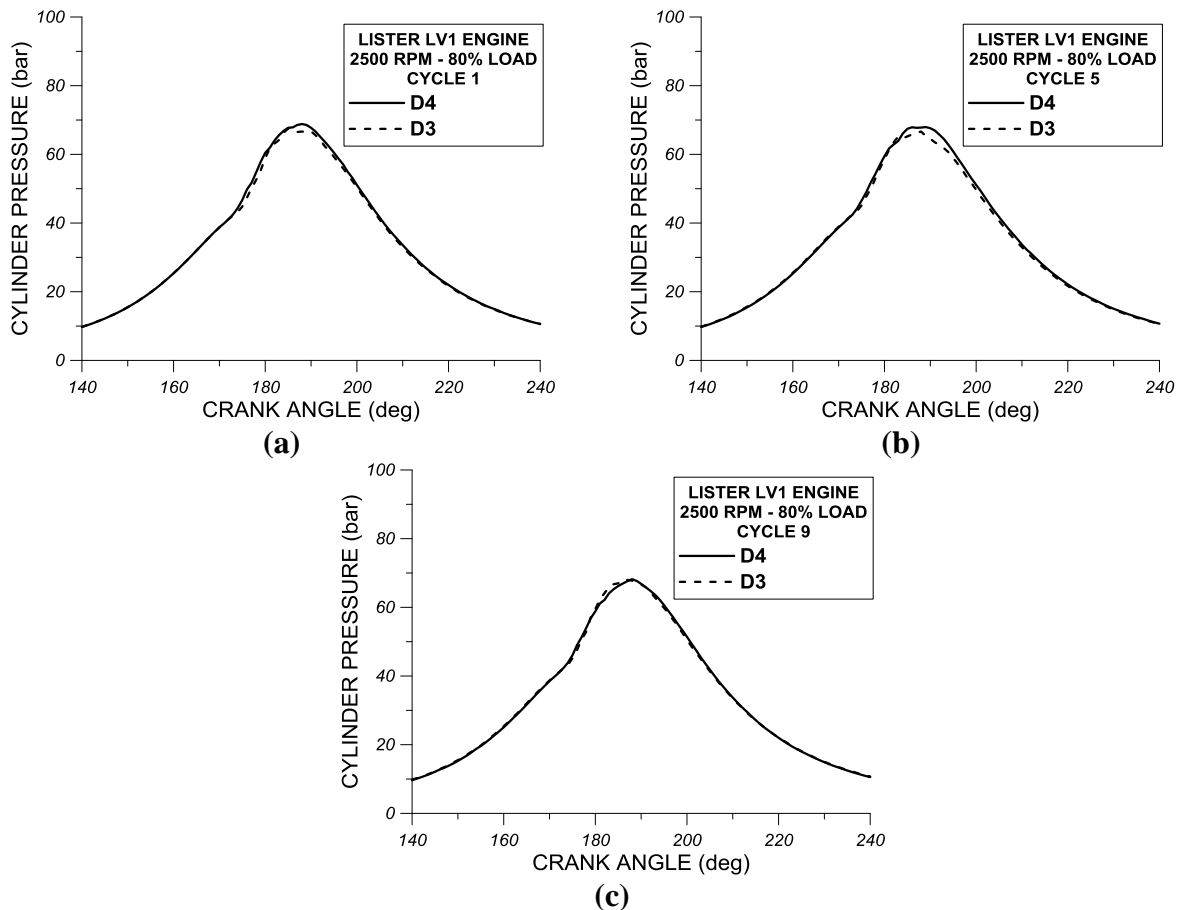


FIGURE 14. Comparison of experimental results for cylinder pressure of (a) the first operation cycle, (b) the fifth operation cycle and (c) the ninth operation cycle for test fuels D3 and D4 at 2500 rpm and at 80% of full load. Experimental results are given for the high-speed single-cylinder DI diesel engine “Lister LV1”

Figures 15(a)-(c) show comparative experimental results of the fuel injection pressure between the conventional fuels D3 and D4 from the first operation cycle (Figure 15(a)), the fifth operation cycle (Figure 15(b)) and the ninth operation cycle (Figure 15(c)). The experimental results of the injection pressure of Figures 15(a)-(c) refer to experimental measurements obtained at 2500 rpm and 80% of full load. From the observation of Figures 15(a)-(c) it results that in all examined engine operation cycles (1st, 5th and 9th) there is an earlier start of the injection pressure rise of fuel D4 compared to fuel D3. The earlier initiation and the steeper injection pressure rise

observed for fuel D4 compared to fuel D3 can be possibly be attributed to the relatively lower value of compressibility factor of fuel D4 compared to fuel D3.

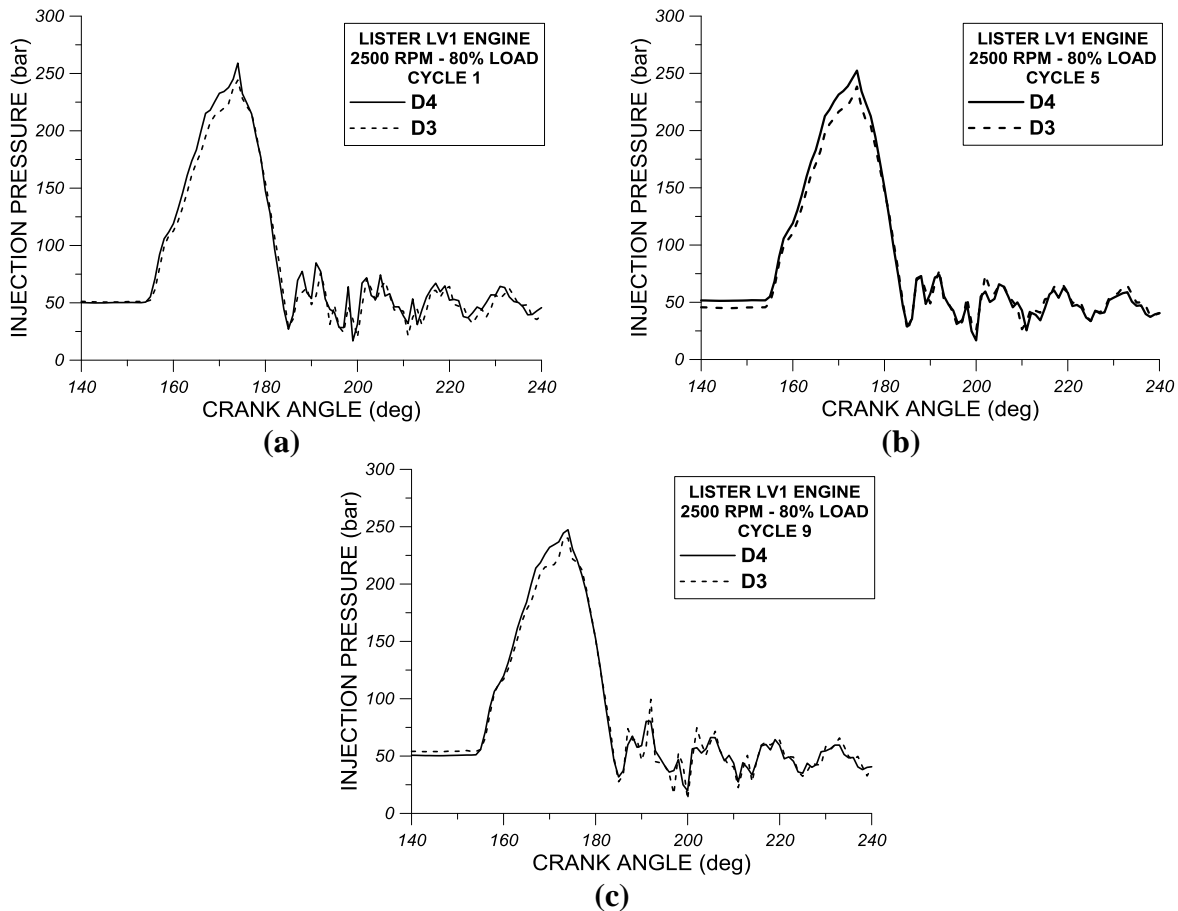


FIGURE 15. Comparison of experimental results for fuel injection pressure of (a) the first operation cycle, (b) the fifth operation cycle and (c) the ninth operation cycle for test fuels D3 and D4 at 2500 rpm and at 80% of full load. Experimental results are given for the high-speed single-cylinder DI diesel engine “Lister LV1”

Figures 16(a) shows comparative experimental results of the instantaneous gross heat release rate between test fuels D3 and D4 at 2500 rpm and 80% of the full load. Figure 16(b) shows comparative experimental results for the instantaneous net heat release rate between conventional fuels D3 and D4 at 2500 rpm and 80% of the full load and Figure 16(c) demonstrates comparative experimental results for the instantaneous heat loss rates at 2500 rpm and 80% full load for fuels D3 and D4. From the observation of Figures 16(a)-(b) it is clearly evidenced an earlier start of combustion for test fuel D4 compared to fuel D3. The earlier start of combustion of fuel D4 compared to fuel D3 is accompanied by a steeper rise of both gross and net heat release rates. The earlier start of combustion of fuel D4 is probably due to the relatively higher cetane number of that fuel compared to fuel D3. However, the premixed combustion intensity of fuel D4 is lower than the corresponding intensity of fuel D3 while the diffusion phase is slightly more intense for fuel D4 compared to fuel D3. From the observation of Figure 16(c) it is evidenced that the instantaneous heat loss rate calculated by Annand semi-empirical model is higher for fuel D4 during combustion and late expansion compared to fuel D3. This is due to the

relatively higher cylinder pressures and temperatures observed for fuel D4 compared to fuel D3 as a result of the slightly higher cetane number of fuel D4 compared to fuel D3.

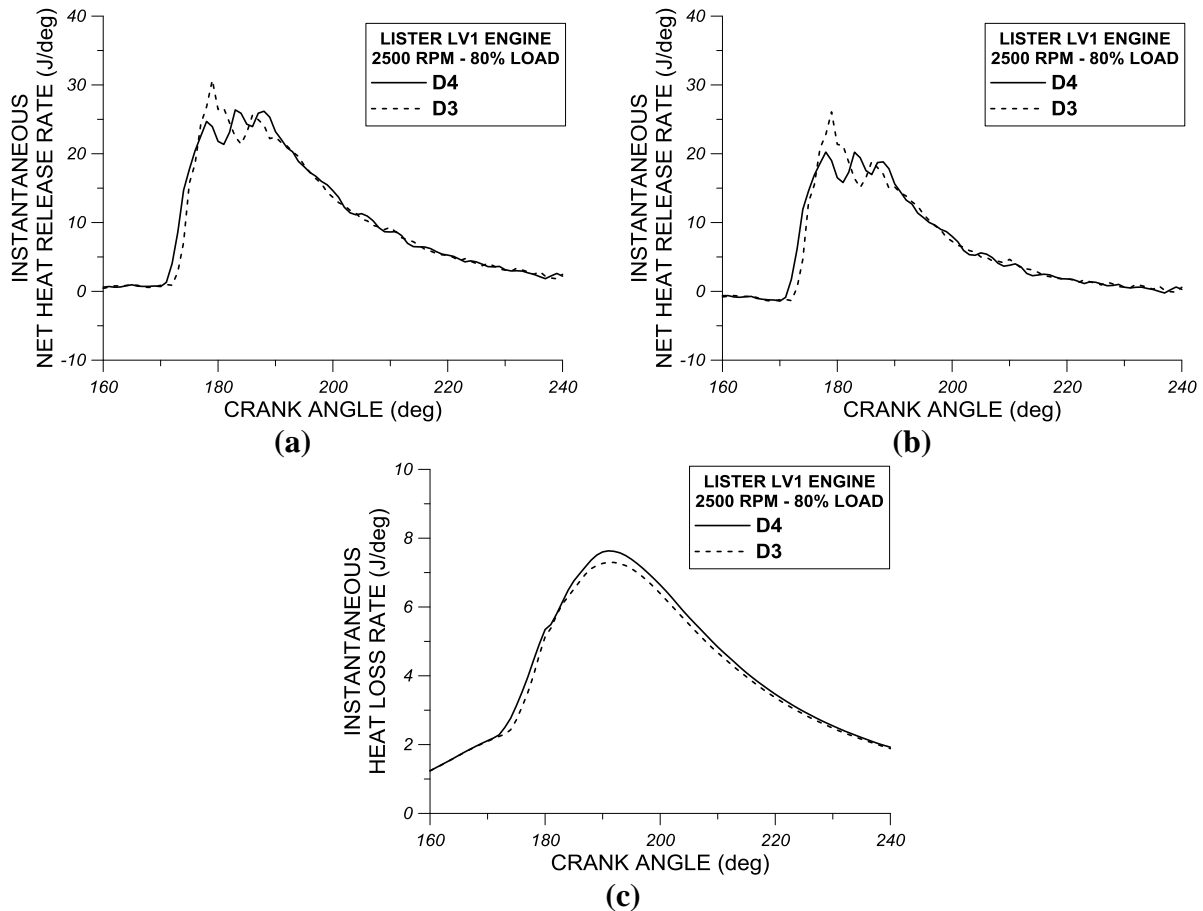


FIGURE 16. Comparison of experimental results for (a) the instantaneous gross heat release rate, (b) the instantaneous net heat release rate and (c) the instantaneous heat loss rate inside engine cylinder for test fuels D3 and D4 at 2500 rpm and at 80% of full load. Experimental results are given for the high-speed single-cylinder DI diesel engine “Lister LV1”

Figure 17(a) shows comparative experimental results of the cumulative gross heat release rate between conventional fuels D3 and D4 at 2500 rpm and at 80% of the full load. Also in Figure 17(b) are presented comparative experimental results for the cumulative net heat release rate between fuels D3 and D4 at 2500 rpm and at 80% of the full load and finally in Figure 17(c) are presented comparatively experimental results for the cumulative heat loss rate between fuels D3 and D4 at 2500 rpm and at 80% of the full load. The observation of Figure 17(a) shows that the use of fuel D4 results in slightly higher values of cumulative gross combustion-released rate compared to fuel D3 under the same operating conditions. This small difference, mainly during the expansion stroke, can possibly be attributed to the relatively higher pressures and hence higher in-cylinder gas temperature values observed above for fuel D4 compared to fuel D3. The deviations between the fuel D3 and D4 in terms of the cumulative net heat release rate (see Figure 17(b)) are insignificant. The observation of Figure 17(c) shows higher cumulative heat loss rates for fuel D4 compared to fuel D3, mainly during the expansion stroke because of the

relatively higher values of cylinder pressure and gas temperature as seen above for fuel D4 compared to fuel D3.

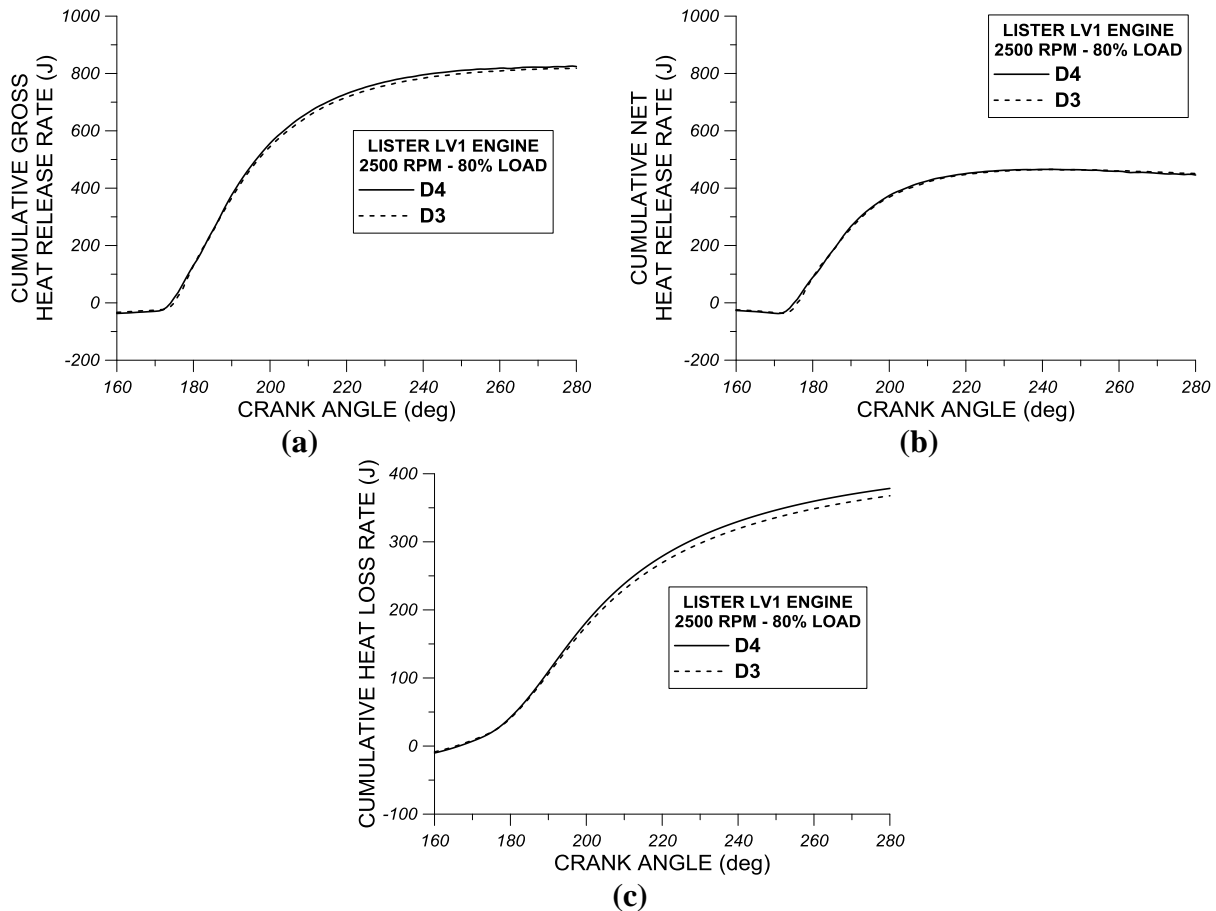


FIGURE 17. Comparison of experimental results for (a) the cumulative gross heat release rate, (b) the cumulative net heat release rate and (c) the cumulative heat loss rate for test fuels D3 and D4 at 2500 rpm and at 80% of full load. Experimental results are given for the high-speed single-cylinder DI diesel engine “Lister LV1”.

Experimental Performance and Combustion Results for Test Fuels BASE, D1, D2, D3 and D4

Figure 18(a) shows comparative experimental results of the indicated power for BASE, D1, D2, D3 and D4 fuels at 2500 rpm and at 80% of the full load from the “Lister LV1” single cylinder diesel engine. What is apparent from the observation of Figure 18(a) is that the deviations in the indicated power between the BASE, D1, D2, D3 and D4 fuels are insignificant even though the fuels D1, D2, D3 and D4 show a relatively higher value of the indicated power compared to the BASE fuel. Figure 18(b) shows comparative experimental results of the brake specific fuel consumption (BSFC) for BASE, D1, D2, D3 and D4 fuels at 2500 rpm and at 80% of full load from the “Lister LV1” engine. At this point, it should be recalled that all engine tests with all examined fuels were made by adjusting the fuel consumption according to the lower heating value of each fuel so that the fuel consumption multiplied by the lower heating value (thermal fuel power) is such that the engine load remained constant (i.e. 80% of full load at 2500

rpm of the “Lister LV1” engine corresponds to a 4kg hydraulic brake load). From the observation of Figure 18(b) the BSFC values of all examined fuels are relatively higher compared to the respective values exhibited by contemporary diesel engines. This observation can be ascribed to the fact that the “Lister LV1” is a significantly older naturally-aspirated DI diesel engine compared to modern turbocharged and highly sophisticated diesel engines, which indicate significantly lower BSFC values than the ones of the “Lister LV1” engine. However, the purpose of the present analysis is to evaluate the main engine operational parameters and the main combustion characteristics of the “Lister LV1” for all fuels examined under the same operating conditions so that this comparison draw useful conclusions regarding the effect of the chemical composition and physicochemical properties of the examined fuels on “Lister LV1” performance and combustion characteristics. From the observation of Figure 18(b) it appears that fuels D1 and D2 exhibit lower BSFC values compared to fuels BASE, D3 and D4. In addition, there is a small decrease of the BSFC when switching from fuel D1 to fuel D2 and when switching from fuel D3 to fuel D4. The lower BSFC values observed in the case of fuels D2 and D4 compared to fuels D1 and D3 can be attributed to the increase of density and viscosity and to the simultaneous reduction of compressibility factor, which as seen results in higher fuel injection pressures.

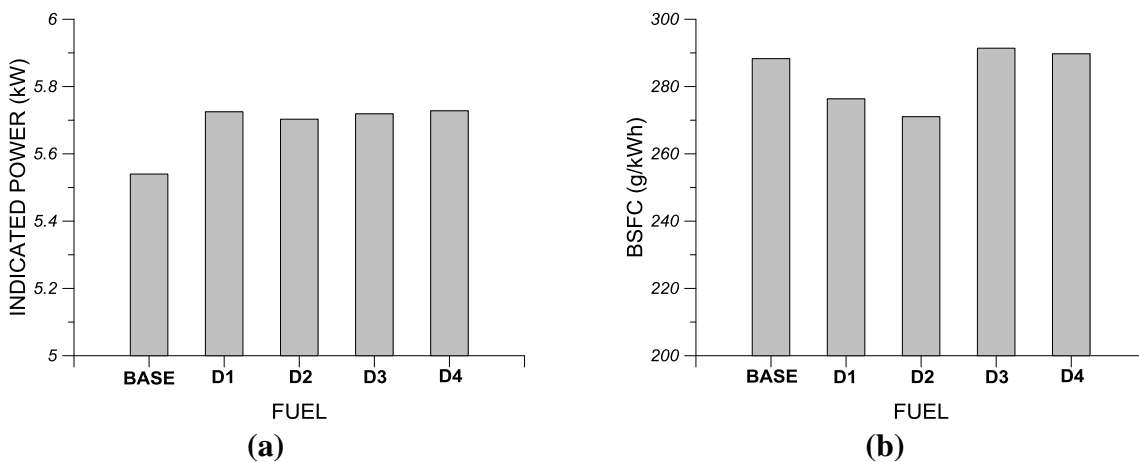


FIGURE 18. Comparative evaluation of experimental results for (a) engine indicated power and (b) engine BSFC for test fuels BASE, D1, D2, D3 and D4. Experimental results are given for the high-speed single-cylinder DI diesel engine “Lister LV1” at 2500 rpm and at 80% of full load.

Figure 19(a) shows comparative experimental results of the fuel injection duration for fuels BASE, D1, D2, D3 and D4 at 2500 rpm and at 80% of full load from “Lister LV1” single-cylinder diesel engine. The observation of Figure 19(a) shows that fuels BASE, D1 and D3 have almost identical fuel injection durations, while fuels D2 and D4 exhibit higher injection durations compared to the previous fuels. The higher values of injection duration observed for fuel D2 compared to fuel D1 and also for fuel D4 compared to D3 are due to the higher values of density and viscosity and the lower values of compressibility factor of fuels D2 and D4 compared to fuels D1 and D3. Figures 19(b)-(d) show comparative experimental results for the combustion duration of the 25% of fuel injected mass per engine cycle (CA25) (Figure 19(b)), the combustion duration of the 50% of fuel injected mass per engine cycle (CA50) (Figure 19(c)) and the combustion duration of the 90% of fuel injected mass per engine cycle (CA90) (Figure 19(d)). Results in Figures 19(b)-(d) are given for test fuels BASE, D1, D2, D3 and D4 at 2500 rpm and at 80% of full load for the “Lister LV1” single-cylinder diesel engine. According to

Figures 19(b)-(d) the transition from fuel D1 to fuel D2 results in a small increase of CA25, CA50 and CA90 and thus, the small decrease of fuel LHV when switching from fuel D1 to D2 results in the small elongation of premixed combustion (CA25) and in the small elongation also of both premixed and diffusion-controlled combustion (CA90). As observed from Figures 19(b)-(d) the transition from fuel D3 to fuel D4 results in a small decrease of CA25, CA50 and CA90 and thus, the small increase of fuel LHV when switching from fuel D3 to D4 results in the small shortening of premixed combustion (CA25) and in the small shortening also of both premixed and diffusion-controlled combustion (CA90).

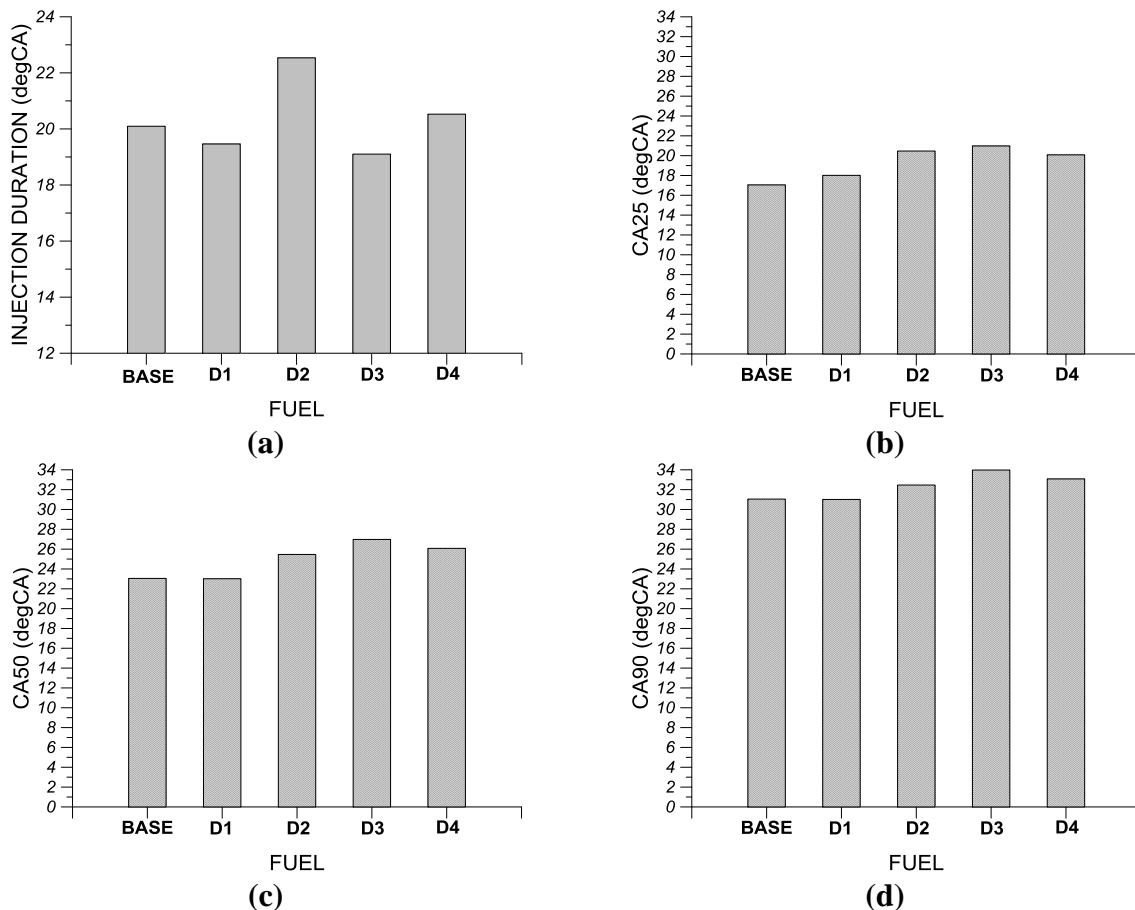


FIGURE 19. Comparative evaluation of experimental results for (a) fuel injection duration, (b) combustion duration of the 25% of fuel injected mass per engine cycle (CA25), (c) combustion duration of the 50% of fuel injected mass per engine cycle (CA50) and (d) combustion duration of the 90% of fuel injected mass per engine cycle (CA90) for test fuels BASE, D1, D2, D3 and D4. Experimental results are given for the high-speed single-cylinder DI diesel engine “Lister LV1” at 2500 rpm and at 80% of full load

Figure 20(a) shows comparative experimental results for the Start of Injection (SOI) of fuels BASE, D1, D2, D3 and D4 at 2500 rpm and at 80% of full load from the “Lister LV1” single-cylinder diesel engine. The observation of Figure 20(a) shows that fuels BASE, D2 and D4 demonstrate an earlier initiation of fuel injection (i.e. higher values of SOI) compared to fuels D1 and D3. The earlier initiation of fuel injection observed in the case of fuels D3 and D4 compared to fuels D1 and D2 can be attributed to the lower values of compressibility factor of

fuels D3 and D4 compared to the ones of fuels D1 and D2. Figure 20(b) shows comparative experimental results for the ignition angle for fuels BASE, D1, D2, D3 and D4 at 2500 rpm and at 80% of full load from the “Lister LV1” single-cylinder diesel engine. From the observation of Figure 20(b) it appears that BASE fuel has a higher ignition angle (earlier start of combustion) than the fuels D1, D2, D3 and D4. It is also observed that fuel D2 has a higher ignition angle, i.e. ignites slightly faster than the fuel D1, mainly due to its relatively higher cetane number compared to fuel D1. The transition from fuel D3 to D4 fuel is accompanied by a small decrease in the ignition angle (a small delay in the start of combustion), which is related to differences in the rate of injection between the two fuels.

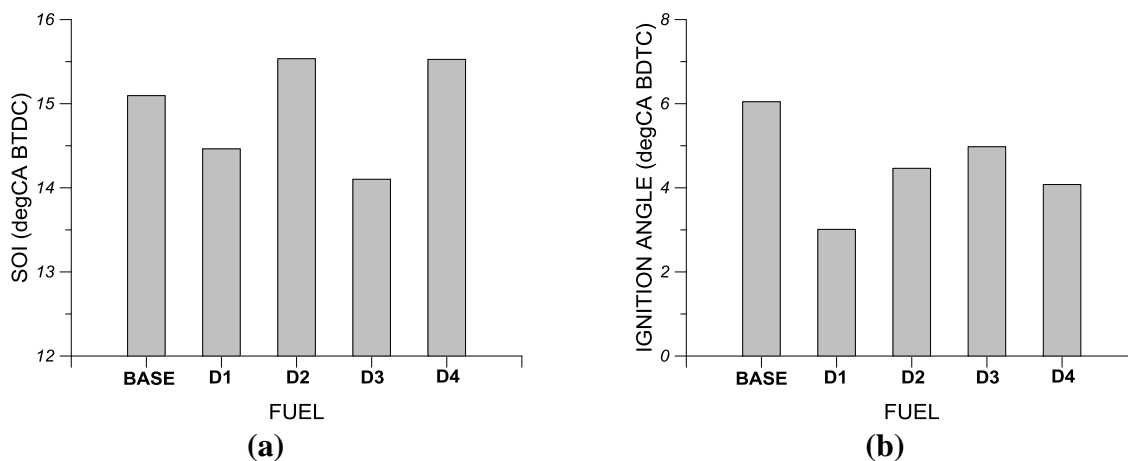


FIGURE 20. Comparative evaluation of experimental results for (a) fuel injection timing i.e. Start of Injection (SOI) and (b) ignition angle for test fuels BASE, D1, D2, D3 and D4. Experimental results are given for the high-speed single-cylinder DI diesel engine “Lister LV1” at 2500 rpm and at 80% of full load

Figure 21(a) shows comparative experimental results of the ignition delay for fuels BASE, D1, D2, D3 and D4 at 2500 rpm and at 80% of full load for the “Lister LV1” single-cylinder diesel engine. From the observation of Figure 21(a) it appears that fuels D1 and D2 have approximately the same ignition delay, which is greater than the ignition delay of fuels BASE, D3 and D4. The transition from fuel D3 to D4 is accompanied by a small decrease in ignition delay due to increased density and viscosity and a decrease in compressibility factor, which these parameters influence the start of injection and the small increase in cetane number, which influences the reduction of the ignition angle (earlier start of combustion). Figure 21(b) shows comparative experimental results for the maximum combustion pressure of fuels BASE, D1, D2, D3 and D4 at 2500 rpm and at 80% of full load for the “Lister LV1” single-cylinder diesel engine. No significant fluctuations, in the maximum combustion pressure among the BASE, D1, D2, D3 and D4 fuels, are observed. The worthy observation is that the transition from fuel D3 to D4 fuel is accompanied by a small increase in the maximum combustion pressure as a result of earlier combustion start, which is attributable to the small increase of the cetane number.

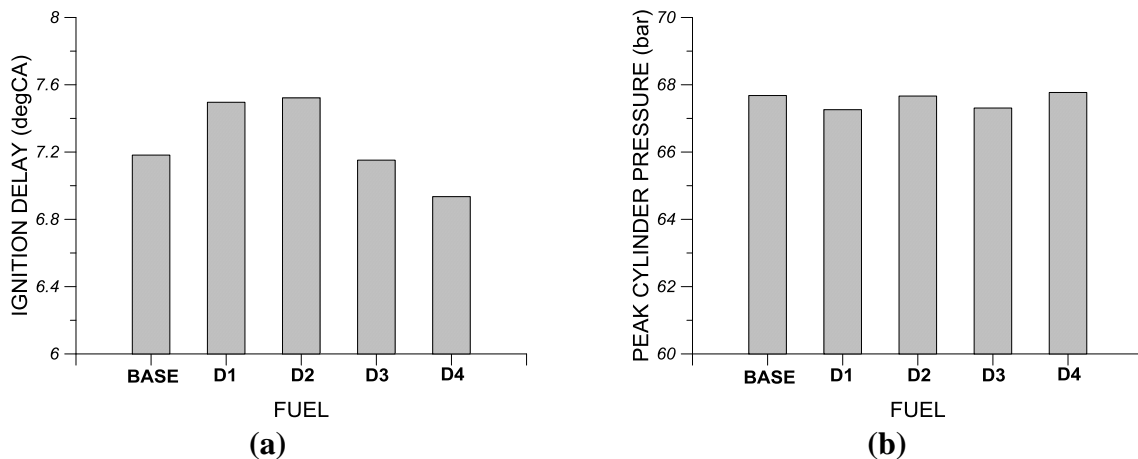


FIGURE 21. Comparative evaluation of experimental results for (a) ignition delay and (b) peak cylinder pressure for test fuels BASE, D1, D2, D3 and D4. Experimental results are given for the high-speed single-cylinder DI diesel engine “Lister LV1” at 2500 rpm and at 80% of full load.

CONCLUSIONS

In the present study a detailed computational model was developed for processing experimental data for cylinder pressure, fuel injection pressure and TDC position. The developed model is a general purpose one, which can be used for experimental data processing and for calculating DI diesel engine performance and combustion characteristics in both four-stroke and two-stroke DI diesel engines. The developed computational model was used for analyzing raw experimental data for cylinder pressure, injection pressure and TDC position obtained from a previous experimental investigation performed in a single-cylinder DI diesel engine (“Lister LV1”) using five different conventional diesel fuels with variable fuel properties. During the analysis of the experimental results emphasis was given to the examination of the effect of fuel physical properties such as fuel density, viscosity and compressibility factor on the examined diesel engine performance characteristics and combustion parameters. Utilizing the experimental results and the fuel properties the following conclusions were extracted regarding the variation of fuel properties between examined fuels and regarding their influence on the performance and combustion characteristics of the examined “Lister LV1” engine:

- The increase of distillation temperature and the partial replacement of paraffins from naphthenes resulted primarily in the increase of fuel viscosity and in the increase of the cetane number and secondarily, in the increase of fuel density and in the decrease of the fuel compressibility factor.
- The increase of fuel density and viscosity and the increase of fuel cetane number in combination with the reduction of fuel compressibility factor resulted in:
 - Earlier initiation of combustion
 - Reduction of ignition delay due to increase of fuel cetane number
 - Increase of injection pressure rise rate and in slightly higher peak injection pressures
 - Small decrease of specific fuel consumption

REFERENCES

1. T.C. Zannis and D.T. Hountalas, *Energy & Fuels* 18(3), 659-666 (2004).
2. G. Lepperhoff, H. Baecker, A. Pungs and K-D. Petters, "The influence of diesel fuel composition on the particulate and NOx emission under steady state and transient engine operation conditions", 9th Int. Symposium for Transport and Air Pollution, Avignon, France, 2000.
3. H. Baecker, A. Pungs, S. Pischinger and K-D. Petters and G. Lepperhoff, "The influence of fuel composition on the soot formation in diesel engines", 3rd Int. Fuels Colloquium, Esslingen, Germany, 2001.
4. B. Martin, P. Aakko, D. Beckman, N. Del Giacomo and F. Giavazzi, "Influence of Future Fuel Formulations on Diesel Engine Emissions - A Joint European Study", Society of Automotive Engineers (SAE), SAE Technical Paper 972966, 1997.
5. K. Nakakita, H. Ban, S. Takasu, Y. Hotta, K. Inagaki, W. Weissman and J.T. Farrell, "Effect of Hydrocarbon Molecular Structure in Diesel Fuel on In-Cylinder Soot Formation and Exhaust Emissions", Society of Automotive Engineers (SAE), SAE Technical Paper 2003-01-1914, 2003.
6. K. Nakakita, S. Takasu, H. Ban, T. Ogawa, H. Naruse, Y. Tsukasaki and L.I. Yeh, "Effect of Hydrocarbon Molecular Structure on Diesel Exhaust Emissions Part 1: Comparison of Combustion and Exhaust Emission Characteristics among Representative Diesel Fuels", Society of Automotive Engineers (SAE), SAE Technical Paper 982494, 1998.
7. Y. Takatori, Y. Mandokoro, K. Akihama, K. Nakakita, Y. Tsukasaki, S. Igushi, L.I. Yeh and A.M. Dean, "Effect of Hydrocarbon Molecular Structure on Diesel Exhaust Emissions Part 2: Effect of Branched and Ring Structures of Paraffins on Benzene and Soot Formation", Society of Automotive Engineers (SAE), SAE Technical Paper 982495, 1998.
8. H. Song, K-S. Quinton, Z. Peng, H. Zhao and N. Ladommatos, *Energies* 9, 28 (2016)
9. M. Hublin, P.G. Gadd, D.E. Hall and K.P. Schindler, "European Programmes on Emissions, Fuels and Engine Technologies (EPEFE) - Light Duty Diesel Study", Society of Automotive Engineers (SAE), SAE Technical Paper 961073, 1996.
10. C.J.J. Den Ouden, W.W. Lange, C. Maillard, R.H. Clark, L.T. Cowley and R.J. Strandling, "Fuel Quality Effects on Particulate Matter Emissions from Light- and Heavy-Duty Diesel Engines" Society of Automotive Engineers, No. 942022 (1994).
11. C. Beatrice, C. Bertoli, N. Del Giacomo, M. na Migliaccio and C. Guido, "Potentiality of the Modern Engines Fed by New Diesel Fuels to Approach the Future European Emission Limits", Society of Automotive Engineers (SAE), SAE Technical Paper 2002-01-2826, 2002.
12. T.L. Ullman, R.L. Mason and D.A. Montalvo, "Effects of Fuel Aromatics, Cetane Number, and Cetane Improver on Emissions from a 1991 Prototype Heavy-Duty Diesel Engine", Society of Automotive Engineers (SAE), SAE Technical Paper 902171, 1990.
13. N. Miyamoto, H. Ogawa, M. Shibuya, K. Arai and O. Esmilaire, "Influence of the Molecular Structure of Hydrocarbon Fuels on Diesel Exhaust Emissions", Society of Automotive Engineers (SAE), SAE Technical Paper 940676, 1994.
14. Y. Kidoguchi, C. Yang and K. Miwa, "Effects of Fuel Properties on Combustion and Emission Characteristics of a Direct-Injection Diesel Engine", Society of Automotive Engineers (SAE), SAE Technical Paper 2000-01-1851, 2000.
15. E.J. Sienicki, R.E. Jass, W.J. Slodowski, C.I. McCarthy and A.L. Krodel, "Diesel Fuel Aromatic and Cetane Number Effects on Combustion and Emissions From a Prototype 1991 Diesel Engine", Society of Automotive Engineers (SAE), SAE Technical Paper 902172, 1990.
16. N. Miyamoto, H. Ogawa, M. Shibuya, and T. Suda, "Description of Diesel Emissions by Individual Fuel Properties", Society of Automotive Engineers (SAE), SAE Technical Paper 922221, 1992.
17. T. Ogawa, T. Araga, M. Okada and Y. Fujimoto, "Fuel Effects on Particulate Emissions from D. I. Engine - Chemical Analysis and Characterization of Diesel Fuel", Society of Automotive Engineers (SAE), SAE Technical Paper 95235, 1995.

18. N. Ladommatos, Z. Xiao and H. Zhao, Proc. Instn. Mech. Engrs, J. of Automobile Engineering, 214(D), 779-794 (2000).
19. H. Richter and J.B. Howard, Prog. Energy Combust. Sci. 26, 565-608 (2000).
20. T.C. Zannis and D.T. Hountalas, J. Energy Institute 77, 16-25 (2004).
21. NEDENEF, "New Diesel Engines and New Diesel Fuels", GROWTH Programme, Final Technical Report, (2003).
22. T.C. Zannis, "Thermodynamic Analysis and Experimental Investigation of the Effect of Liquid Fuels on Diesel Engines", PhD Thesis, School of Mechanical Engineering, National Technical University of Athens, Greece, 2006.
23. D.T. Hountalas and A. Anestis, Energy Conv. Management 39, 589-607 (1998).
24. S.C. Draper and T.Y. Li, Journal Aerospace Science 16, 593-610 (1949).
25. R.S. Benson and R. Pick, "Recent Advances in Internal Combustion Engine Instrumentation with Particular Reference to High-Speed Data Acquisition and Automated Test Bed", Society of Automotive Engineers (SAE), SAE Technical Paper 740695, 1974.
26. J.W. Alyea, "The Development and Evaluation of an Electronic Indicated Horsepower Meter", Society of Automotive Engineers (SAE), SAE Technical Paper 690181, 1969.
27. W.L. Brown, "The Caterpillar imep Meter and Engine Friction", Society of Automotive Engineers (SAE), SAE Technical Paper 730150, 1973.
28. H.I.S. Alwood, G.A. Harrow and L.J. Rose, "A Multichannel Electronic Gating and Counting System for the Study of Cyclic Dispersion, Knock and Weak Mixture Combustion in Spark Ignition Engines", Society of Automotive Engineers (SAE), SAE Technical Paper 700063, 1970.
29. R.V. Fischer and J.P. Macey, "Digital Data Acquisition with Emphasis on Measuring Pressure Synchronously with Crank Angle", Society of Automotive Engineers (SAE), SAE Technical Paper 750028, 1975.
30. A.V. Bueno, J.A. Velásquez and L.F. Milanez, "Internal Combustion Engine Indicating Measurements", in Applied Measuring Systems, InTech, 2012.
31. A.V. Bueno, J.A. Velásquez and L.F. Milanez, Mechanical Systems and Signal Processing 25, 3209-3210 (2011)
32. A.V. Bueno, A.V., J.A. Velásquez and L.F. Milanez, Applied Thermal Engineering 29, 1657-1675 (2009)
33. A.V. Bueno, A.V., J.A. Velásquez and L.F. Milanez, Energy 36, 3907-3916 (2010)
34. MATLAB and Statistics Toolbox Release 2014a, The MathWorks, Inc., Natick, Massachusetts, United States.
35. D.R. Lancaster, R.B. Krieger and J.H. Lienesch, "Measurement and Analysis of Engine Pressure Data", Society of Automotive Engineers (SAE), SAE Technical Paper 750026, 1975.
36. M. Lapuerta, O. Armas and V. Bermúdez, Applied Thermal Engineering 20, 843-861 (2000)
37. S.C. Chapra and R.P. Canale, Numerical Methods for Engineers, Sixth Edition, McGraw-Hill, 2010
38. B. Hahn and D.T. Valentine, Essential MATLAB for Scientists and Engineers, Third Edition, Butterworth-Heinemann, 2007.
39. J.B. Heywood, Internal Combustion Engine Fundamentals, New York: McGraw-Hill, 1988.
40. J.E. Dec, SAE Trans., J. Engines 106, 1319-1348 (1997).
41. R.B. Krieger and G.L. Borman, "The Computation of Apparent Heat Release for Internal Combustion Engines", ASME paper 66-WA/DGP-4, 1966.

Atmospheric Corrosion of Carbon Steel, Aluminum, Copper and Zinc in a Coastal Military Airport in Greece

Charalampos Titakis*, Panayota Vassiliou and Ioannis Ziomas†

* Corresponding author. E-mail address: *c.z.titakis@gmail.com, ctitakis@central.ntua.gr (Major C. Titakis).*

Laboratory of Physical Chemistry, School of Chemical Engineering National Technical University of Athens, 9 Heroon Polytechniou, 15780, Athens, Greece

Abstract. The effects of relative humidity (RH), temperature (T), sulphur dioxide (SO₂) concentration and chlorides deposition rate on the corrosion of Carbon Steel, Aluminum, Copper and Zinc at the rural and coastal environment of Pachi military airport, after 2 years of outdoor exposure, are presented. A classification of the corrosivity of the airport atmosphere was based both on environmental data and the corrosion rate measurements of carbon steel and aluminum standard specimens, after the first year of exposure, according to ISO standards and ASTM norms. A systematic investigation is carried out for the two-year outdoor exposure period for all the tested metals based on corrosion rates determination and corrosion products characterization. The findings underline the necessity of field studies results, in order to locally optimize the cost-benefit ratio in all steps of the aircrafts life-cycle.

Keywords: Atmospheric corrosion; corrosion management; military airport; corrosion damage algorithm

INTRODUCTION

Atmospheric corrosion constitutes a major problem with regard to the deterioration of construction materials, especially metals. The importance of the phenomenon of corrosion, as a consequential factor in the protection of human constructions is firstly understood by the economic implications and also the intensity of the efforts being made locally and internationally to mitigate it. Several studies have concluded that corrosion costs at about 3-6% of the Gross Domestic Product of the industrialized nations, where atmospheric corrosion plays a main part [1-5]. Organized attempts to understand the phenomena of atmospheric corrosion and at the same time to develop prediction models of environmental corrosivity began in 1980, when three programs studying atmospheric corrosivity worldwide were initiated. With the participation of countries on four continents, Europe, America, Asia and Oceania, the ISOCORRAG, ICP/UNECE and MICAT programs were launched. Despite their differences there were a number of similarities of the basic methodologies. The main goals were to establish the Dose Response Functions (DRF) based on the acquired experimental data: meteorological (Temperature (T), Relative Humidity (RH), Precipitation (P), and Time Of Wetness (TOW)), pollution (SO₂ and NaCl) and the determination of a methodology in order to be used for the classification for the atmospheric corrosivity. As a result in 1992, the publication of ISO 9223-9226 [6-9] was a major step for the atmospheric severity methodology, evaluation and

classification from the viewpoint of outdoor exposure of metal specimens considering a relatively small spectrum of climatological and pollution conditions. Additionally, an extensive research has been carried out on the damage response functions and corrosion severity. In the work of Morcillo et al [10] the corrosion data obtained in the ISOCORRAG and MICAT programs analyzing the corrosivity categories are compared to those estimated on the basis of ISO standard 9223 [6] for the four reference metals. The correlation coefficients obtained for the damage functions of the 4 metals were hardly improved.

Many systematic research works that followed, suggest that the most significant changes, from the atmospheric corrosion point of view, was the decrease in the SO₂ pollutant concentration, the increase in other types of air pollution and the increase of the average annual precipitation and temperature over the course of the 20th century. Carbon steel corrosion rate has decreased exponentially at non-marine sites (urban, industrial and rural) and specifically by 50% about each 12-year period for industrial and urban sites and each 16-year period for rural sites [1], during the last decades, mostly due to the reduction of sulphur dioxide's emissions globally. A study of the atmospheric corrosion of the copper, zinc and aluminum exposed outdoors on a coastal, an urban-industrial and a rural environment for 18 months concluded that the interaction between the chloride deposition rate with the time of rainfall effects the corrosion of the three non-ferrous metals in the most dominant way [2]. A future dominant role of chloride deposition in atmospheric corrosion of metals in Europe's coastal and near-coastal areas is also expected [11].

There are other studies that record and evaluate the long-term trends of corrosion and the functional life of manufactured products. Pourbaix [12] and McCuen et al [13] suggest that a 4-year corrosion versus time function is required in order to estimate the 20-30 year corrosion behavior of metals in a certain atmosphere, or 10 years in order to predict the infrastructures or the manufactured products life-cycle. Summitt and Fink in 1980 [14] developed the Corrosion Damage Algorithm (CDA) for the United States Air Force (USAF). The CDA considers first the distance to the salinity factor (sea salt water) leading either to the very severe (AA) grade or judging by the moisture parameters. The CDA was recommended to USAF, by NATO Research and Technology Organization (2011), as a basic tool in order to succeed an initial estimation of the classification of atmospheric severity and as a guide to maintenance and logistic decisions [15]. The last call to set the appropriate maintenance intervals remains in the capability and the experience of the local management, based on the field measured meteorological and pollutant parameters and of the atmospheric corrosivity [14,15]. The models usually employed in order to predict the corrosion damage are statistical regression models, which have been demonstrated as being locally accurate [16,17], but limited when the available environmental and corrosion data are characterized as highly non-linear [18-20]. Artificial Neural Network (ANN) method for metals is also used for modeling non-linear multi-parametric systems [18,19] usually employing the data from (i) the literature of long term exposure tests of metals and (ii) at least five atmospheric corrosion stations. Jianping et al [21] employing the data from literature for long term exposure tests presented an ANN modeling which is, under certain conditions, successful and is not as trustworthy for very long term data. Their results are also better, than those of Feliu et al [18,19,21]. No significant results were obtained by the described artificial neural network models using data collected from less than five atmospheric corrosion stations, after a research in the relevant literature. The ANN can be designed and trained to estimate corrosion rates of metals using meteorological and pollutants data, the exposure time as the input and the experimental metal loss as the output vector, with a relatively small error. An ANN model

designed and trained in order to predict steel corrosion loss after long-term exposure in the Czech Republic calculated the models error at 6% [22]. Despite the fact that all the earlier methodologies (ISOCORRAG, ICP/UNECE and MICAT programs, ISO methodology etc.) have some limitations and new atmospheric corrosion models, which take into consideration the nonlinearity of the accelerating effect of meteorological and pollution variables instead of the mean values of these factors are proposed [23], the ISO standards [6-9] are still regarded as the only reliable and globally accepted methodology to assess the corrosivity by measuring the corrosion rates of standard metal samples and defining the corrosivity category of the atmosphere [24].

In order to succeed a more accurate regional corrosion mapping with high correlation coefficient -which is the main aim of all the relevant programs and researches- and to assess the severity of complex corrosion environments such as coastal industrial establishments, airports, military infrastructure, new approaches in atmospheric corrosion modeling should emerge. The results of site-specific case studies could contribute in existing models improvement or could be utilized in new algorithms training. East Mediterranean countries, such as Greece, have poorly or not at all participated in this global effort. Greece has around 2,800 islands [25] and 13,676 kilometers of coastline [26]. Additionally, the proximity to the sea at the major part of its continental region is a strong indication for relatively high chlorides deposition rate, also, as well as inland. In Greece, an extensive corrosion damage of metal based constructions has been observed. These costs are present in all steps of every infrastructure or product life-cycle, from material selection, design and installation to maintenance intervals and repair.

The present work stems from the need to effectively reduce the corrosion-related damage costs of military aircrafts helicopters and infrastructure. It also aims to optimize the maintenance management and to increase service life of the aircrafts. In order to optimize the corrosion management and select the appropriate protection method a proper understanding of the local corroding system is required. Therefore, commercially pure aluminum, unalloyed carbon steel, zinc and copper have been employed for a long-term atmospheric corrosion study, according to ISO and ASTM norms [6-9,27-31] and a literature review on relevant sources was undertaken [32-39], in the rural and coastal site of a military airport in an effort to assess corrosion impact on aviation installations near the seashore. A classification of the corrosivity of the airport atmosphere was performed both on environmental data and the corrosion rate measurements of carbon steel and aluminum standard specimens, after the first year of exposure, according to these ISO standards and ASTM norms. A systematic investigation -for all tested metals- is also carried out for a two-year outdoor exposure period, based on corrosion rates determination and corrosion products characterization. This approach did not use sensitive information or confidential data.

REGIONAL ENVIRONMENTAL PARAMETERS

Meteorological Data

The mean monthly rainfall, mean monthly wind speed and the prevailing wind at Elefsina and Pachi areas were analytically investigated and presented in [40] with the data that had been provided by the National Observatory of Athens (Megara station), the Ministry of Environment and Energy and the Hellenic Meteorological Service (station of Elefsina) [41-43]. In brief: The

wettest month (with highest rainfall) is December. The driest months (with lowest rainfall) are July and August. The mean annual rainfall amount of the area, during the period 1958-97, has been estimated around 37.29 cm. The mean annual wind speed of the area, during the period 2009-11, has been estimated at approximately 11.22 km/h (3.17 m/s), marginally greater than the threshold value of 11 km/h which is the “minimum wind speed (MWS) or threshold required for the entrainment of marine aerosols over a salt-water body” [34]. The monthly prevailing wind at Megara Area is presented at the Table below:

TABLE 1. Monthly prevailing wind at Megara Area (period: 1975 – 1991) [40,43]

Month	Prevailing Wind	Month	Prevailing Wind
JAN	NORTHWEST (NW)	JUL	NORTHWEST (NW)
FEB	NORTHWEST (NW)	AUG	NORTHWEST (NW)
MAR	NORTHWEST (NW)	SEP	NORTHWEST (NW)
APR	NORTHWEST (NW)	OCT	NORTHWEST (NW)
MAY	NORTHWEST (NW)	NOV	NORTHWEST (NW)
JUN	NORTHWEST (NW)	DEC	NORTHWEST (NW)
CALM: 31%			

Pollutants

By taking into consideration the yearly evolution of the mean concentration values of gas pollutants over the Attica region for the decade 2000–2009, there is an almost constant presence of O₃, with a mean concentration of 55 µg m⁻³ [44]. In the industrial area of Elefsina, where the country’s industrial core is sited and in a distance of 20 km from Pachi airport, the annual mean concentration of SO₂ is at about 7 µg/m³ [40,45,46].

No pollutant measurements have ever been made in the airport area. The concentration of sulfur dioxide at the airport is estimated, according to the European Monitoring and Evaluation Programme (EMEP) [47] and several sources [40,45-52]. Regarding the existence of pollutant SO₂, namely the airport’s area has been studied and the annual maximum concentration of the pollutant estimated at [SO₂]_{max} = 2µg/m³ [40,48].

EXPERIMENTAL PROCEDURE

Materials

Aluminum, zinc, copper and unalloyed carbon steel specimens have been exposed in outdoor atmospheric conditions, at the roof of a maintenance hangar, at a distance of approximately 0.2 km from the seashore at Pachi military airport respectively for a two-year exposure period. Exposure started in 2014 at two different periods of the year, in summer and in winter, in order to determine the seasonal effects on the initial corrosion stage and eventually the long term effects on the metal surface as well as the evolved corrosion rates. The standard specimens of commercially pure aluminum (>99.5%min), unalloyed carbon steel, zinc and copper are flat specimens of size 100 mm×100 mm×1 mm of current fabrication, as described in ISO 9226 [9]. Table 2 shows the detailed composition of the tested carbon steel samples as analyzed by an ARL3460 automatic Optical Emission Spectrometer (OES) at Halyvourgiki Inc. laboratories.

TABLE 2. Average chemical composition (wt.%) of unalloyed carbon steel specimens

Fe	C	Mn	S	P	Si	Ni	Cr	Cu	V	Al	Sn	Mo	Co	As	Ca	Nb	N	O	Pb
99.44	0.07	0.32	0.03	0.0069	0.007	0.02	0.02	0.04	0.0007	0.01	0.004	0.003	0.003	0.0017	0.0006	0.001	0.004	0.016	0.0008

Selection of Exposure Site

The military airport of Pachi, Megara, Greece was selected as exposure site due to (i) the macroscopic observation of the corrosion in aircraft subassemblies and of the construction materials in helicopters, after technical inspection, (ii) the high costs in all steps of the aircrafts life-cycles worldwide and (iii) to the proximity of the rural test site to the seacoast and to the surrounding industrial area of Elefsina.

Preparation of the Specimens and of the Installation at the Exposure Site

Four test pieces were used for each metal and period of exposure on a rack at 45° to the horizontal facing south, as seen in Figures 1 and 2. The metal structures were designed with the use of “3D CAD Design Software SOLIDWORKS”, according to standard ISO 9225 [8], and constructed in the Laboratory of the Manufacturing Technology of NTUA. Three specimens, for each metal and period of exposure, were weighted before and after the exposure in order to measure the weight loss. The preparation, cleaning of the metal coupons (and the mass loss of the exposed metal samples was determined after sequential pickling as per ISO 8407 [28] and the ASTM norm, G1-90 [29]. Chemical cleaning procedures for the removal of the corrosion products are described in Table 3.

TABLE 3. Chemical cleaning procedures for removal of corrosion products after the exposure

Metal	Chemical	Time	Temperature
Aluminum	50 ml phosphoric acid, 30 gr chromium trioxide, distilled water to make 1lt.	10 min	80°C to boiling
Steel	250 ml hydrochloric acid with inhibitor, distilled water to make 1000 ml.	10 min	20-25°C
Zinc	150 ml ammonium hydroxide, distilled water to make 1000 ml.	5 min	20-25°C
Copper	500 ml hydrochloric acid, distilled water to make 1000 ml.	3 min	20-25°C



FIGURE 1. Outdoor exposure of the flat metal specimens at the airport. On the frame, the Tinytag PLUS 2 data logger with Temperature/Relative humidity probe



FIGURE 2. Device used for “Determining Atmospheric Chloride Deposition Rate by Wet Candle Method” at the airport. Facing the sea in a distance of 150 m from the seacoast

Corrosion Evaluation Methodology

Three test specimens for each metal and period of exposure were used for gravimetric analysis. The fourth test specimen for each metal was used for the analysis of the corrosion products formed on the metal surface. All samples were weighed before and after exposure. Test work was carried over 2 years, with samples taken for analysis after 3, 6, 12 and 24 months during the two periods of exposure. “TableCurve 2D v5.01.01” and “Microsoft Excel” programs were used for the determination of the power equations and for plotting the data relative to the corrosion loss. Corrosion rates were determined from the weight loss of specimens in accordance

with ISO 9226 [9]. The obtained data were used for the classification of atmospheric corrosivity according to ISO 9223 [6]. The corrosion products formed on the metal surfaces have been characterized by: (i) The FEI Quanta 200 Scanning Electron Microscope/Energy Dispersive Spectrometer (SEM/EDS) coupled with Energy Dispersive X-Ray Analysis (EDAX). The SEM images were analyzed by means of the computer program EDGE.EXE [53]. (ii) The Siemens D-500 X-ray diffractometer (with a graphite crystal monochromator and a Cu anticathode) based on an automatic adjustment and analysis system, with Diffract-EVA quality analysis software [54]. (iii) A Leica DMR Optical Microscope (OM). (iv) The aluminum surface morphology examination was by an Atomic Force Microscope Scanner (AFM) DUALSCOPE 95-50 of DME.

Carbon steel and aluminum specimens are also exposed each year since 2014 for a 1-year exposure period, during winter (the worst case scenario as concerns the direct corrosion of the 2 metals at Pachi Airport region), in order to examine the reliability of the Corrosion Damage Algorithm at the airport's region.

Recording of T and RH at the Test Site

The parameters of air temperature (T °C) and of relative humidity (RH%) were obtained by a temperature and RH data logger «Tinytag» PLUS2 (TGP-4500) for a year at the exact field sites, as seen in the frame of Figure 1. T and RH were also used for calculating the Time of Wetness (TOW) using the procedure given in ISO 9223 [6].

Airborne Salinity Determination

Airborne salinity by chloride is in the process to be measured by the Wet Candle Method for the airport according to ISO 9225 [8] and ASTM G140-02 [27] standards. Sampling is performed every 30 days, while a new sample is positioned for further exposure. The amount of chlorides, in every sample, is measured by both the Mohr and Volhard titration methods, as well as by AgNO_3 test.

RESULTS AND DISCUSSION

In-situ Measurement of Airport's Meteorological Conditions

The monthly variation of the temperature-humidity data and the time of wetness are presented on Figure 3.

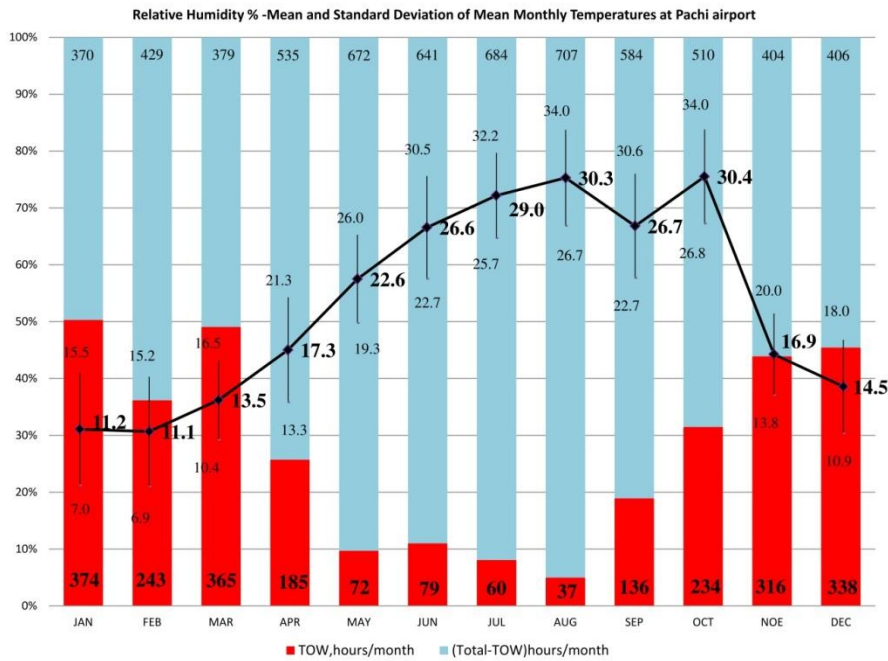


FIGURE3. Monthly variation of T (°C) and RH (%) data at the Airport Area

The Time of Wetness expressed in hours per year is estimated in 2,439 hours/a. The RH-TOW factor is expected to affect the atmospheric corrosion of metals in a major degree. The influence of temperature on the atmospheric corrosion of many metals has a maximum at about 9-11 °C. The mean annual temperature at the airport is 20.9°C. According to a previous study [40], the concentration of sulphur-containing substances represented by SO₂ is smaller than 12 µg/m³. Due to the NW prevailing wind at Megara area, from inland to the seashore and the mean annual wind speed [40] the salinity is expected to affect the corrosion of metals to a lesser degree than what is generally expected for a coastal site.

The 2-Year Corrosion Evolution of the Tested Metals and Classification of the Corrosivity of Pachi Airport Atmosphere

The 2-Year Corrosion Evolution of the Tested Metals

For modeling the data relative to the corrosion loss, the (power) kinetic equation (1) in the form:

$$y = a \times t^b \tag{1}$$

where a: a constant, t: time of exposure in days; and b: time exponent. The validity of the equation and its reliability to predict long-term corrosion has been demonstrated by many authors [19,55-62].

The constant “a” represents the corrosion loss during the first year, while the time exponent “b” represents the multi-year loss yield [63]. The lower the time exponent “b” term the more protective the corrosion product layer on the metal surface [64]. Both a and b constants are dependent on the type of metal and on the climatic parameters. The statistical correlation coefficient, R, is a measure of the grade of fit of the environment regression, and R², the

coefficient of determination, expresses the fraction of total variance of the data explained by the regression [63]. Regression analyses of the time exponent “b” and “a” values against the environmental factors of TOW, sulfation and salinity, by SW Dean and DB Reiser [63], indicated that for all four metals, the time exponent regressions were barely or not at all significant with environmental variables and on the other hand, the “a” regressions were very significant in most cases.

The representation of the corrosion data versus time in a power plot are depicted at Table 4 and Figures 4-7 for each one of the tested metals. Figures 4-7 show the experimental gravimetric curves, when exposure starts during winter (upper curve) and during summer (lower curve), and the fitted model equations obtained for carbon steel, aluminum, copper and zinc metal specimens for the coastal site of Pachi for the two initial time of exposure (initial corrosion stage). Table 4 shows the mass loss data for 1 and 2 years determined experimentally and the model equation parameters and the estimation of 4-year corrosion by the projection of the model equations.

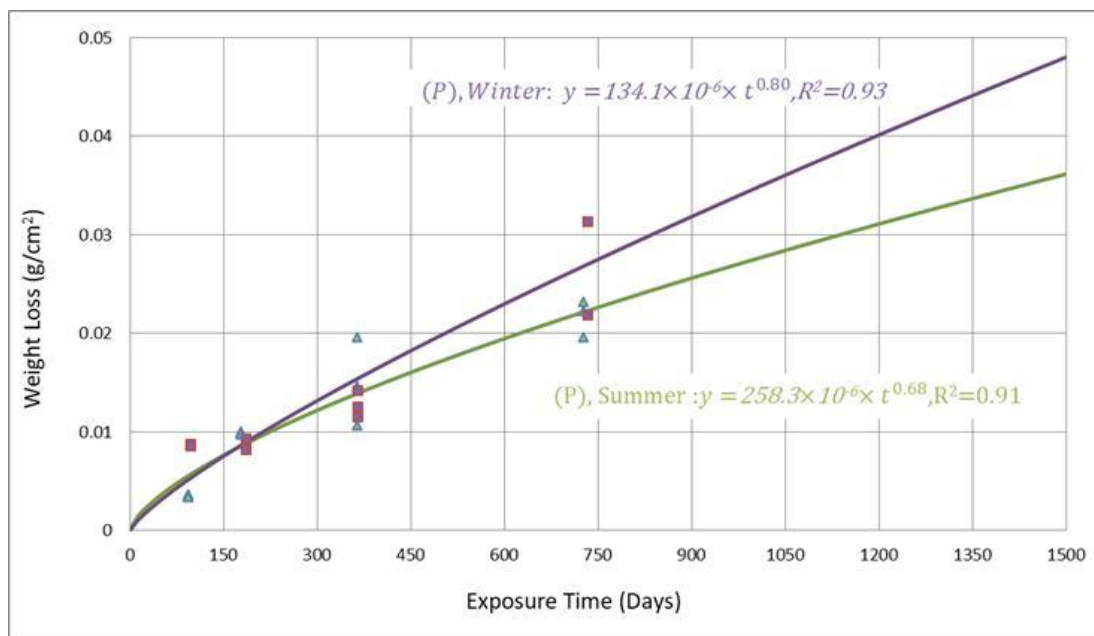


FIGURE 4. Experimental gravimetric curves, with exposure starting during winter (upper curve) and summer (lower curve), for unalloyed carbon steel and the fitted model equations.

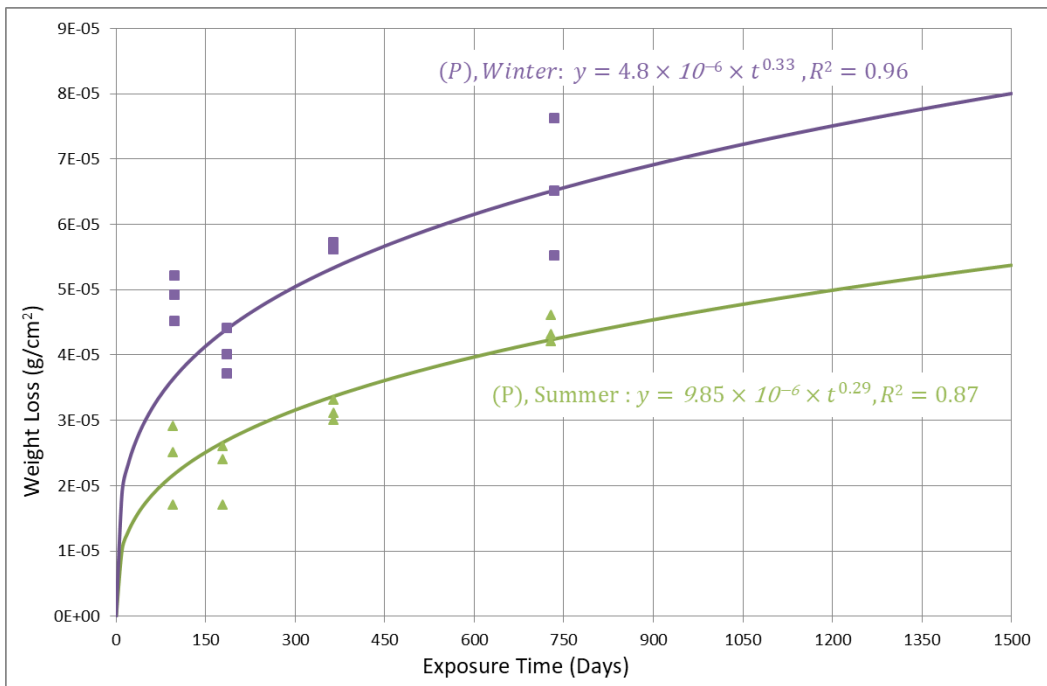


FIGURE 5. Experimental gravimetric curves, with exposure starting during winter (upper curve) and summer (lower curve), for Aluminum Alloy 1050 and the fitted model equations.

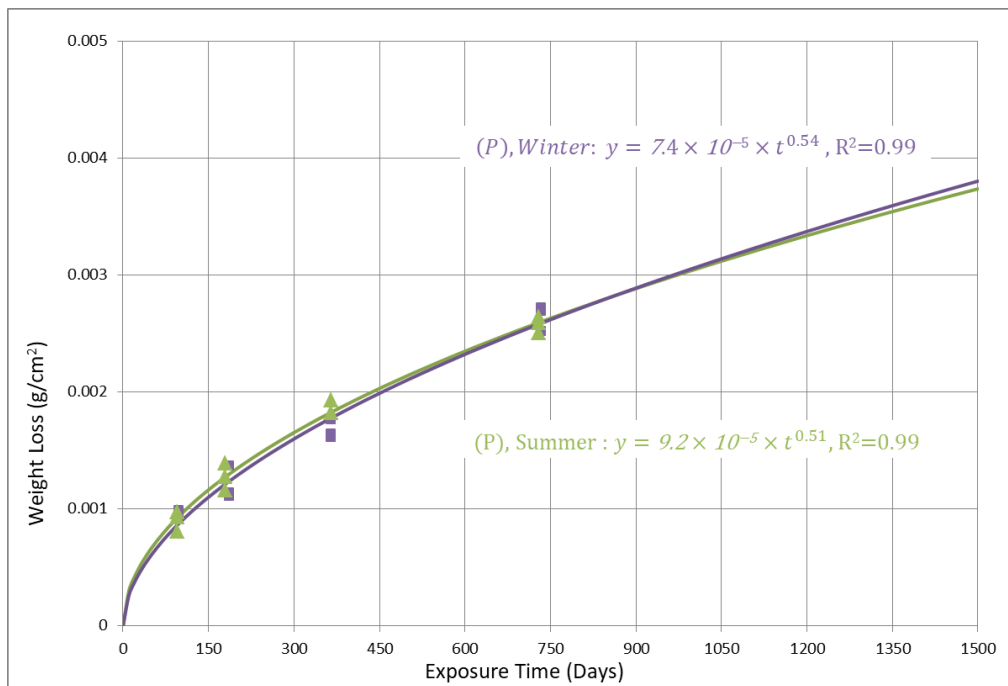


FIGURE 6. Experimental gravimetric curves, with exposure starting during winter (upper curve) and summer (lower curve), for Copper and the fitted model equations.

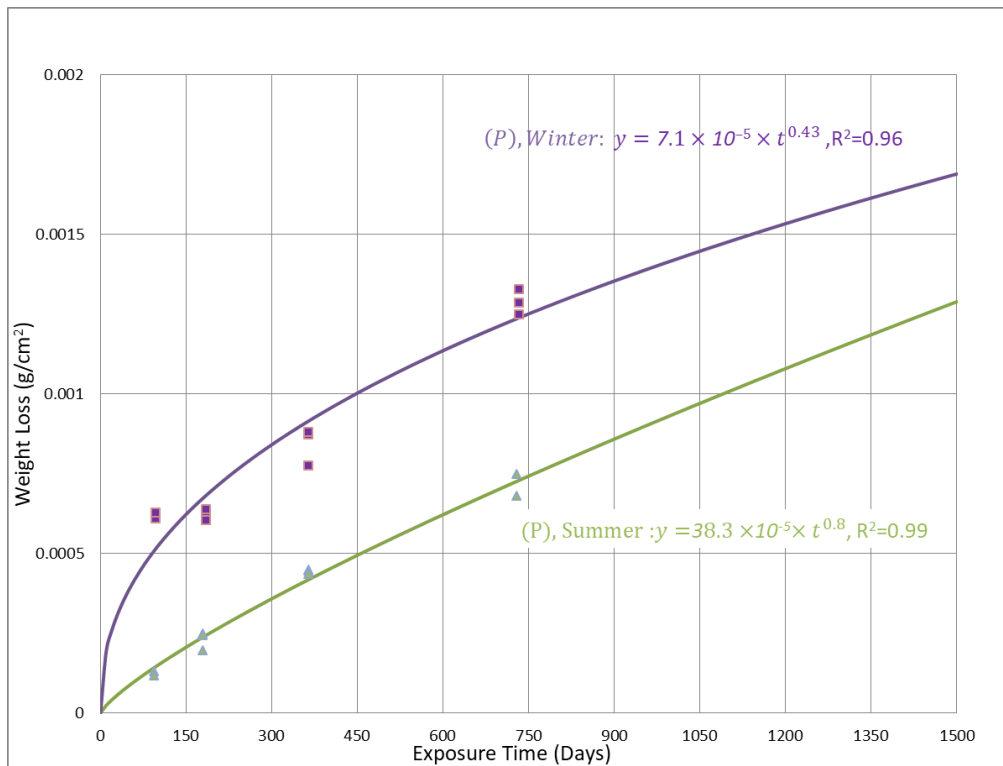


FIGURE 7. Experimental gravimetric curves, with exposure starting during winter (upper curve) and summer (lower curve), for Zinc and the fitted model equations

TABLE 4. Mass loss data for 1 and 2 years experimentally determined and the model kinetic parameters. Estimation of 4-year corrosion by the projection of the model equations

Metal	Exposure Start	Average Mass Loss (g/m ²)			Calculated Kinetic Equations Constants		
		1 Year	2 Years	4 Years	a	b	R ²
Carbon Steel	Summer	149.1	216.4	355	258.3×10^{-6}	0.68	0.91
	Winter	126.5	281	470	134.1×10^{-6}	0.80	0.93
Aluminum	Summer	0.31	0.44	0.53	9.85×10^{-6}	0.29	0.87
	Winter	0.57	0.66	0.79	4.8×10^{-6}	0.33	0.96
Copper	Summer	20.9	25.8	36.9	9.2×10^{-5}	0.51	0.99
	Winter	16.7	26.4	37.5	7.4×10^{-5}	0.54	0.99
Zinc	Summer	4.4	7.1	12.6	38.3×10^{-5}	0.80	0.99
	Winter	8.4	12.9	16.7	7.1×10^{-5}	0.43	0.96

In the case of carbon steel, the relatively small value of the time exponent agrees with the TOW observed at the airport environment. The value of the carbon steel time exponent in an atmosphere with higher TOW would be higher. Sulfation and salinity strongly affect the “a” constant [63]. The «a» values at the airport are relatively high due to the effect of sulphur-containing substances and salinity (due to the proximity to the sea). The “a” value is higher during summer at the airport probably due to the maximization of the frequency of aircraft technical tests and as a result the maximization of aircrafts fuel emissions (sulfation) in combination with the lower wind speeds which results to higher SO₂ and sea-salt deposition on the metal surfaces [63]. During the first year of exposure, steel exhibits an almost identical

corrosion rate and is independent of the period (summer or winter) initially exposed. Multi-year corrosion evolution shows that the synergistic effect of sea chlorides, from natural airborne salinity, with SO₂ plays a significant role in determining the corrosion rate of steel [65,66]. High RH-TOW, during the period December-March, and the decisive influence of temperature, during January and February increase the corrosion of steel specimens. Unalloyed carbon steel, exposed during winter, showed increased corrosion among the tested metals. The O₃ pollutant has little effect in steel corrosion rate and there is no synergistic effect of O₃ with the SO₂ pollutants [67].

In the case of aluminum, the “b” values are not strongly affected by environmental variations, due to the Al₂O₃ spontaneous formation upon exposure in the environment, which protects the metal substrate. Sulfation and salinity affect the “a” value much less than the other three metals [41]. Aluminum exhibits the lowest “a” and time exponent “b” values than the other tested metals. The corrosion values found less than 0.30 g/m²a, during the multi-year corrosion evolution, are mainly the result of metal attack by the chemical reagent used during cleaning for gravimetric weight loss calculation rather than by the severity of the atmosphere [66]. The highest corrosion rate of aluminum specimens are observed at winter. That was expected mainly due to the effect of high RH-TOW, in relation to the samples exposed during summer, and secondarily due to the impact of salinity [58], because of the proximity to the sea. High RH-TOW, during the period December-March, and the mean monthly temperature, during January and February, also guide to the relatively increased corrosion attack. Aluminum corrosion rate is the lowest among the tested metals.

In the case of copper, salinity and TOW strongly affect both the time exponent and the “a” values. [63]. During the first year of exposure, copper corrosion rate is an order of magnitude lower than that of steel and independent of the initial period of exposure. Copper has a low corrosion rate because of its low thermodynamic tendency to react (low potential compared to iron). Copper also exhibits the highest coefficient of determination value (R²=0.99).

In the case of zinc, the environmental variables do not affect the protectiveness of the corrosion product to a great degree. TOW and chlorides affect the time exponent values to a small degree. Higher TOW reduces the protective capacity of corrosion layer. Sulfation strongly affects the “a” value, but not as strongly as steel [63]. When the zinc chloride is formed and there is no washing out by rain the layer does not increase, unless there is a continuous layer of electrolyte induced by the humidity which at night will form a water layer on the surface. From the first year of exposure, zinc exhibits corrosion rate dependent of the period initially exposed and an order of magnitude lower than steel, a fact that has been found by other researchers [68]. Higher RH-TOW play the catalytic role in corrosion rate of zinc [68]. The synergistic effect of the relative high moisture with sulphur dioxide [52] and relative high ozone concentration [69] in the atmosphere increases its corrosion rate. As it is observed, high concentration of SO₂ or high concentration of chlorides in the atmosphere leads to the dissolution of the protective corrosion layer and creates water-soluble corrosion products that lead to high corrosion rates of zinc [70-72]. Zinc corrosion rate decreases with time and that leads to the fact of relatively low concentration of both pollutants (SO₂ and chlorides), that confirms the results of this study and the classification analyzed below. In the marine atmosphere (P₀) of the airport the corrosion of zinc is a direct function of TOW and the chloride pollution level [73]. The multi-year corrosion evolution shows that zinc specimens exposed during winter exhibit steadily higher corrosion rate, by at least 45%, than those exposed during summer.

Gravimetric data for the winter season: During the first 3 months of exposure higher weight loss values are obtained for aluminum, steel and zinc causing deviations from fitted

curves. This can be attributed to the water-solubility of the initial corrosion products. From the 6-month experimental data it is evident that both corrosion film dissolution and water-insoluble corrosion products accumulation take place.

Classification of the Corrosivity of the Pachi Airport Atmosphere

Data on the corrosivity of the atmosphere are essential for the development and specification of optimized corrosion resistance for manufactured products. The corrosivity category is a technical characteristic which provides a basis for the selection of materials and consequently protective measures in atmospheric environments subject to the demands of the specific application particularly with regard to service life [9].

The airport atmosphere is classified by sulphur-containing substances represented by SO₂, in accordance with ISO 9223 [6], in pollution category P₀ ([SO₂] < 12 µg/m³), which is accounted to be background pollution by SO₂ and insignificant from the point of view of corrosion attack. The Time of Wetness expressed in hours per year is estimated in 2439 hours/a. As a result, the atmosphere is classified of TOW as «T3», according to ISO9223:1992 [6]. The characterization of an outdoor test site with respect to its corrosivity can be accomplished by determining the corrosion rate of standard specimens exposed for one year to the atmosphere at the respective location (direct corrosivity evaluation). The corrosion rate for the first year of exposure for the different corrosivity categories is presented at Table 5.

TABLE 5. Corrosion rates for the first year of exposure for the different corrosion categories according to ISO:9223 [6].

Corrosion Category	carbon steel (g/m ² a)	Aluminum (g/m ² a)
C1	≤10	Negligible
C2	11 – 00	≤0.6
C3	201 – 400	0.6 – 2
C4	401 – 650	2 – 5
C5	651 – 1500	5 – 10

The average chemical composition of commercially pure aluminium (>99.5% min) and of the unalloyed carbon steel (Cu 0.03% to 0.10%, P<0.007%) specimens used at this study meets the requirements described by ISO 9226. In contrast, zinc and copper, according to the commercial supplier, does not meet the requirements described by ISO 9226 [9]. As a result, the classification of the atmospheric corrosivity, for carbon steel and aluminum is presented at Table 6.

TABLE 6. First-year of exposure corrosion rate of carbon steel and aluminum and ISO classification of the atmosphere severity at the airport according to ISO:9223 [6].

Exposure Start	Metal (g/m ²)	
	Carbon Steel	Aluminum
Pachi/Summer	149.1	0.31
Pachi/Winter	126.5	0.57
ISO Classification of Corrosivity of Atmospheres	C2 «LOW»	C2 «LOW»

The higher first-year corrosion rate of carbon steel specimens, exposed during summer, is primarily caused by the background pollution of the area (SO₂ and salinity) and the high conductivity of the steel specimens surface due to the existing Particulate Matters (PMs) in the area augmented by the North African dust (PM₁₀) during the initial time of exposure.

According to the classification of the corrosivity of atmosphere, the airport atmosphere, with regard to pollution by airborne salinity, according to ISO 9223 [6], is expected to be classified as pollution category S₀ (deposition rate of chloride ≤ 3 mg/(m²d)) or S₁ (deposition rate of chloride in mg/m²d: 3<S<60). In relation with the corrosion products development and the atomic concentration of chloride observed on copper specimens (presented below), the chloride deposition rate is not insignificant, regarding the atmospheric corrosion, and it cannot be considered as background pollution. As a result the pollution category S₁ appears to be better related to the observed corrosive environment. This estimation is expected to be confirmed or rejected by the results of the wet candle methodology.

After a comparison of the results of the meteorological and pollution data, and of the gravimetric analysis on carbon steel and aluminum specimens exposed at the coastal site of Pachi, so far, to the expected corrosion damage, estimated by the CDA, there are indications that the CDA does not provide a good correlation between the predicted and the actual corrosion damage at the Pachi Military Airport (Figure 8).

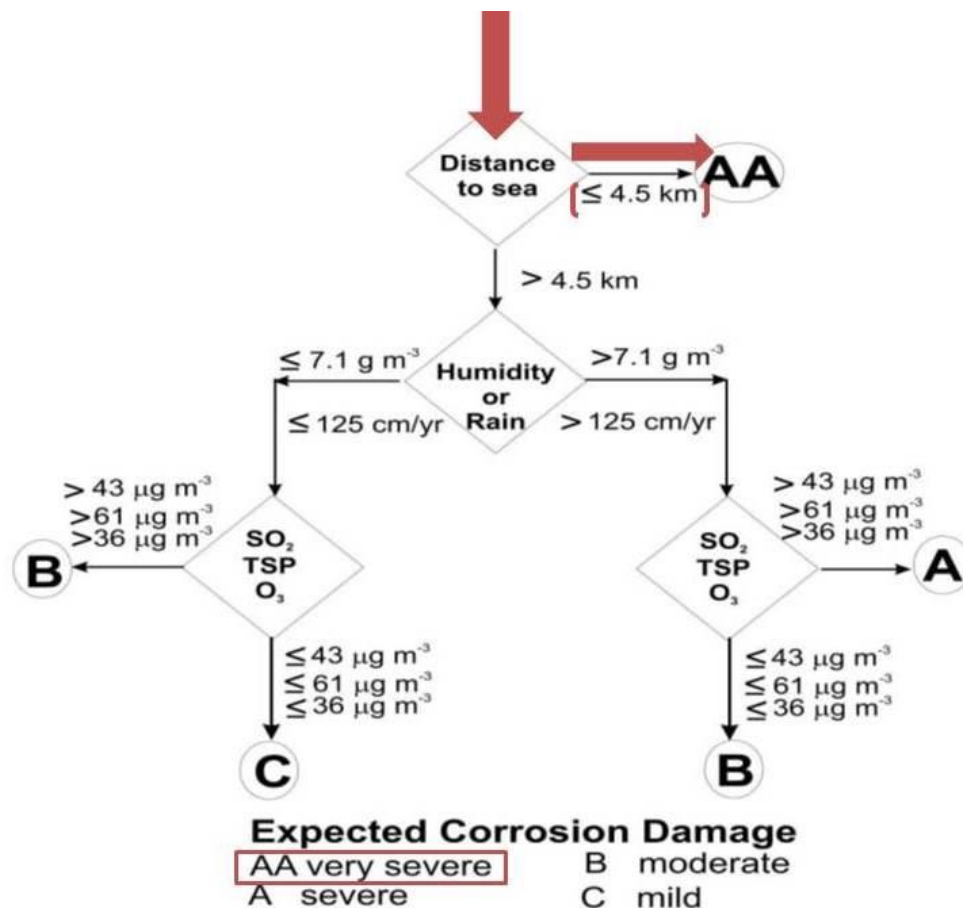


FIGURE 8. Section of the Corrosion Damage Algorithm that Considers Distance to Salt Water, Leading Either to the Very Severe AA Rating or a Consideration of the Moisture and the Pollutants and the Expected Corrosion Damage to Carbon Steel and Aluminum Components of the Aircrafts at the Airport (Red Path) Site [14, 15]

The comparison of the classification of atmospheric corrosivity, according to the ISO classification system, to the expected corrosion damage by the CDA at the airport is presented at Table 7.

TABLE 7. Comparison of the classification of Atmospheric Corrosivity, According to the ISO Classification System, to the Expected Corrosion Damage by the (CDA) at the Pachi Airport.

Pachi airport	Metal	
	Unalloyed Carbon Steel	Commercially Pure Aluminum
ISO Classification of Corrosivity of Atmospheres	C2 “LOW	C2 “LOW
CDA Classification of Corrosivity of Atmospheres	AA “very severe”	

Characterization of the Metals Surfaces after 2 Years of Exposure

In the case of unalloyed carbon steel traces of sulphur, carbon and chloride, attributed to the aircrafts fuel emissions and the proximity to the sea (0.2 Km) respectively, are detected from the carbon steel specimens surface analysis by Scanning Electron Microscope/Energy Dispersive Spectrometer (SEM/EDS). Indications of hydroxychlorides and sulfides formation are also detected on both sides probably because of the small thickness of the corrosion layers or the water solubility of the corrosion products. Carbon Steel exhibits the highest concentration of oxygen among the tested metals due to the oxides and hydroxides formed. Growth of oxides, hydroxides and hydroxychlorides are observed, both in skyward and downward sides, already out of the 1st semester of exposure by X-ray Diffraction (XRD). Lepidocrocite and traces of goethite were identified after two years of exposure of carbon steel specimens surface in the atmosphere independently from the initial time of exposure (summer or winter) and the side of the specimens (skyward or downward). Magnetite is identified on the specimens’ skyward surface, exposed during winter, after 2 years of exposure. The corrosion products development on steel surface observed by Optical Microscope (OM) and by X-ray Diffraction (XRD), during the 2-year exposure period, for both initial time of exposure, is presented at the Figures 9 and 10 below.



FIGURE 9. Corrosion products developments on steel surface observed by OM.

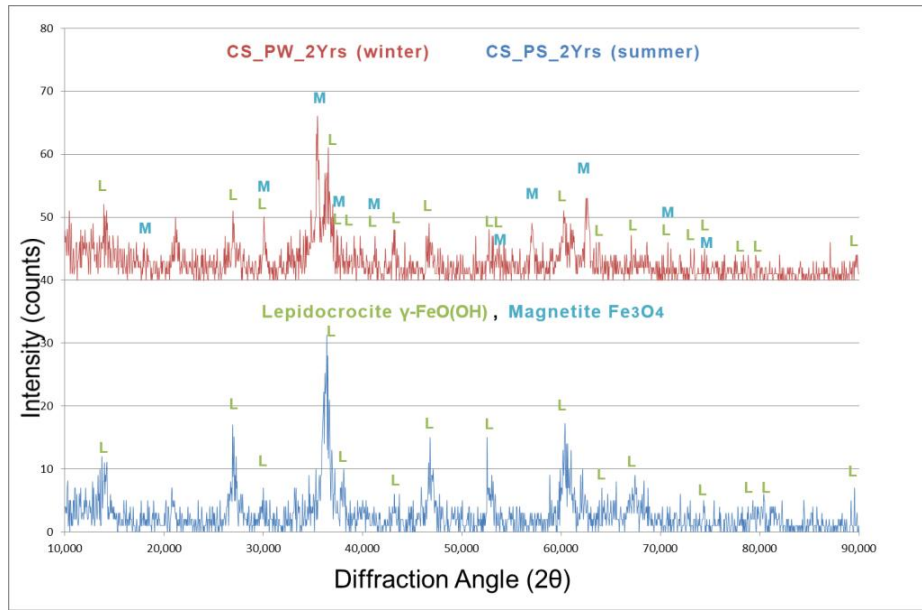


FIGURE 10. Corrosion Products Developments on Steel Surface (Skyward Side) Identified by X-ray Diffraction (XRD) After a 2-Year Exposure Period.

The corrosion products development on the copper surface observed by Optical Microscope (OM), during the 2-year exposure period, is presented at Figure 11.

		Before the exposure	After 1 Year of Outdoor Corrosion		After 2 Years of Outdoor Corrosion	
			Summer	Winter	Summer	Winter
Skyward side						
Downward side						

FIGURE 11. Corrosion products developments on copper surface

In the case of copper, increased concentrations of oxygen and chlorides are detected by SEM/EDS. Copper exhibits the highest concentration of chlorides among the tested metals. On the skyward side of copper specimens (x100), after 2 Years of exposure (exp. start: Winter and Summer) the % atomic concentration of oxygen, sulphur and chloride were 57% O, 0.5% S and 6-9% Cl, respectively. On the zoomed in area of the Back Scattered Electron image of copper specimen by SEM/EDS (area on the frame of Figure 12), after 2 years of exposure, the % atomic concentration of oxygen, sulphur and chloride detected by SEM/EDS was 61.5% O, 0.5% S and 8.35% Cl respectively).

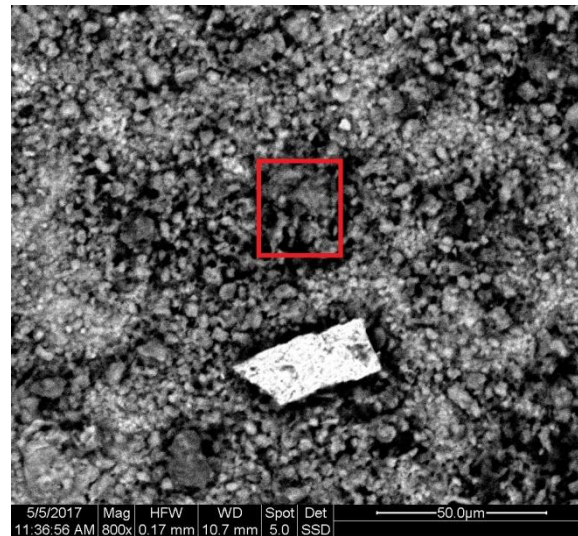


FIGURE 12. Back Scattered Electron Image (BSE) of Copper Specimen (Skyward Side) x800, After 2 Years of Exposure (Exp. Start: Winter), with detected local chloride attack

Growth of oxides and hydroxides both in skyward and downward sides, already out of the 1st semester of exposure, has been observed by XRD. Cuprite (Cu_2O) is identified as the main corrosion product, at both sides of the specimens, after the 2-year outdoor exposure.

In the case of zinc, no visual significant corrosion impact is observed. Local traces of sulphur, due to aircrafts fuel emissions, are observed. No chloride compounds are detected. The high TOW favors the dissolution of zinc chlorides in moisture film. On the skyward side of zinc specimens (x800), after 2 Years of exposure (exp. start: Winter and Summer) the % atomic concentration of sulphur and oxygen were 0.49% S and 34.9% O respectively.

In the case of aluminum, no visual significant corrosion impact is observed. Oxygen, traces of sulphur & chlorides are only locally detected by SEM, after a 2-year exposure period, despite the aircrafts fuel emissions, the proximity to the sea, and the aluminum susceptibility to pitting corrosion. Pitting is macroscopically and microscopically detected on aluminum specimens surface, but in a much smaller extent than theoretically expected and only after 2 years of exposure, due to (i) the pollution of the area (SO_2 and salinity), (ii) the existing PMs in the area (augmented seasonally by the North African dust), (iii) the meteorology of the area during summer (low RH-TOW and precipitation) and (iv) the presence of the aircrafts in the area. During the transition spring and autumn periods the impact of African dust reaches its peak and increases the particulate matters (PM_{10}) concentrations in the Greek region [74]. It was also observed that the driest months, with lowest rainfall and RH, are July and August [40]. The continuous take-offs/landings and technical tests, during summer, provoke the maximization of the deposition of sulphur dioxide locally, the continuous resuspension and dry re-deposition of the contaminated with sulphur dioxide particulate matters (PMs), on their peak concentration, that guide to relative higher pitting, in density and depth, to the aluminum exposed during summer, as it is presented at Table 8. The surface morphology development of the skyward side of the Aluminum 1050 by AFM, after two years of exposure is presented in Figure 13.

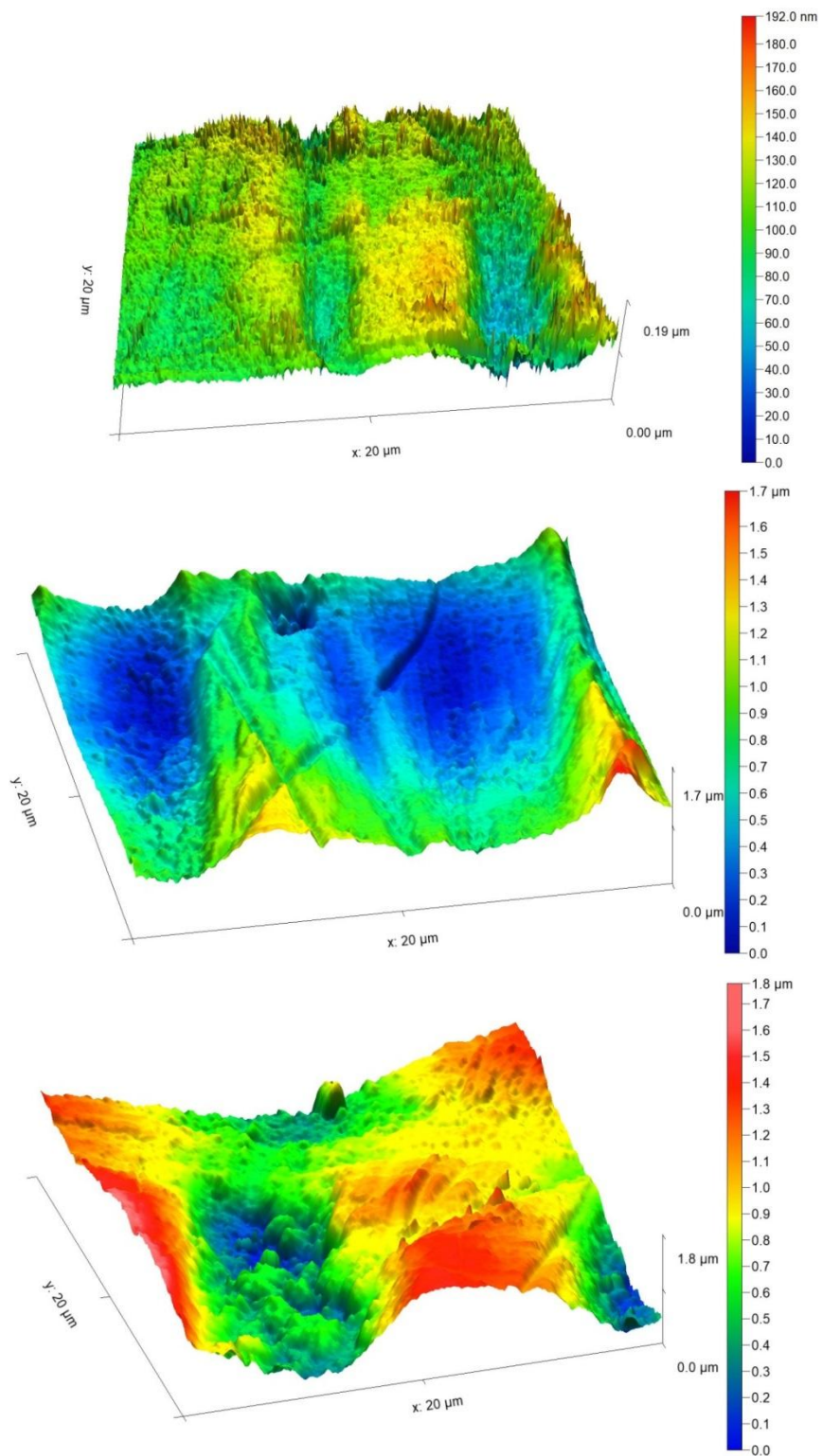


FIGURE 13. Surface morphology of the skyward side of the Aluminum 1050 by AFM, before and after 2 years of exposure during summer and winter respectively

The mean roughness (S_a) of the $400 \mu\text{m}^2$ projected areas of the skyward side of the aluminum 1050, before and after 2 years of exposure during summer and winter, was: 65.2, 131 and 136 nm, respectively. After two years of exposure the mean roughness doubles and the grinding lines appear to be filled with corrosion products. No seasonal deviations are observed regarding the roughness evolution of the aluminum surface at Pachi airport. The rating system for the evaluation of pitting corrosion on aluminum was performed in accordance with ISO 8993[75], after 2 years of exposure. The ISO rating has been done visually and the estimation of the average pitting depth in μm by OM.

TABLE 8. Depth of Pits Observed on the Surface of the Aluminum Samples and Evaluation of Pitting Corrosion on Aluminum by OM in accordance with ISO 8993:1989 [75]

Exposure Start	Average Pitting Depth in μm	Rating	Percentage of Area of Defects
Summer (S)	2	E6	>0.07 and <0.100
Winter (W)	1.5	E1	

A synopsis of the corrosion products formed on metal surfaces, at both sides, and identified by X-ray Diffraction (XRD) is presented at Table 9.

TABLE 9. Corrosion products formed on metal surfaces, after a 2-year exposure period

Metal	Pachi/Summer	Pachi/Winter	Observations	
Aluminum	-	-	No products, at both sides of the specimens, are identified by X-ray diffraction analysis due to the small thickness of the corrosion layers.	
Carbon Steel	Skyward	Lepidocrocite $\gamma\text{-FeO(OH)}$	Lepidocrocite $\gamma\text{-FeO(OH)}$ Magnetite Fe_3O_4	Traces of goethite identified after 2 years of exposure. Formation of hydroxide chlorides and sulfides were not identified probably because of the small thickness of the corrosion layers or the water solubility of the corrosion products.
	Downward	Lepidocrocite $\gamma\text{-FeO(OH)}$		
Zinc	-	-	No products, at both sides of the specimens, are identified by X-ray diffraction analysis due to the small thickness of the corrosion layers.	
Copper		Cuprite Cu_2O	Cuprite (Cu_2O) is identified as the main corrosion product, at both sides of the specimens, after 2-year outdoor exposure.	

Due to the combustion of fossil fuels at the airports region, an atomic concentration of 15-25% of carbon is detected to all metal specimens surfaces by SEM, after 2 years of exposure.

CONCLUSIONS

- Pachi military airport atmosphere is classified on TOW as T3, according to the ISO9223. Relative Humidity is identified as the major factor of corrosion of metals in the airport. Depending on the metal, the RH in conjunction with:
 - (i) the high PMs concentration, especially during autumn, increases aluminum pitting depth and density and leads to higher corrosion rate of the aluminum exposed during summer,
 - (ii) the airborne salinity and the high concentration of O₃ pollutant leads to relative high corrosion rate of copper,
 - (iii) the effect of sulphur-containing substances and of salinity leads to higher corrosion rate of steel and
 - (iv) the effect of sulphur-containing substances leads to a higher corrosion rate of zinc.
- Regarding the existence of SO₂ pollutant, the area has been classified in pollution category P₀, which is considered to be background pollution by sulphur dioxide and insignificant from the point of view of corrosion attack.
- According to the experimental findings the chloride deposition rate on carbon steel and aluminum specimens is expected to be between the values 3<S<60, in mg/m²d.
- After a comparison of the results of gravimetric analysis on carbon steel and aluminum specimens exposed at the coastal site of Pachi, so far, to the expected corrosion damage estimated by the CDA, there are indications that the CDA does not provide a good correlation between the predicted and the actual corrosion damage at the Pachi Military Airport.
- The ISO classification methodology provides a good correlation among corrosivity of atmospheres and actual carbon steel and aluminum corrosion damage in the specific atmosphere. The atmospheric corrosivity regarding carbon steel and aluminum has been classified as C₂ «Low». These results could contribute to the optimization of the local maintenance management.
- The effects on the metal surfaces from the first-year weight losses underline the necessity of field studies when possible, since the corrosion rate proved to be less than originally expected for all the tested metals, due to the regional topography and the environmental characteristics.
- The 2-year weight loss curves and the 4-year corrosion estimation, show that: carbon steel, zinc and aluminum specimens exposed during winter show significantly higher corrosion rates than those exposed during summer. Zinc in particular, exhibits a corrosion rate one order of magnitude lower than steel. No seasonal deviations are observed regarding the corrosion rates of copper specimens, during the 2-year exposure. The corrosion rates at the coastal site of Pachi are relatively low and are ranked in order of decline: carbon steel>copper>zinc> aluminum.

ACKNOWLEDGEMENTS

Authors express their gratitude to Hellenic Army/Technical Corps Directorate - Depots Administration - 301 & 307 Depot Commanders **and especially to Major General (Ret.) Mr. Misail Papadakis** for their support. We would also like to acknowledge the valuable assistance provided by 301 Depot's personnel: G. Somos, D. Kontis, N. Tempelis, by the PhD Candidates of the Laboratory of Physical Chemistry of NTUA: O. Papadopoulou and M. Delagrammatikas and by the mechanical engineers Evangelos Brembos and Konstantinos Mylonas.

REFERENCES

1. H. Simillion, O. Dolgikh, H. Terryn and J. Deconinck, *Corrosion Reviews* (2014).
2. G. H. Koch, M.P.H Brongers, N.G. Thompson, Y.P. Virmani and J.H. Payer, *Corrosion Cost and Preventive Strategies in the United States*. trid.trb.org, 2002.
3. M. V. Biezma and J.R. San Cristobal, “Methodology to Study Cost of Corrosion”, Maney Publishing, 2013.
4. N.G. Thompson, M. Yunovich and D. Dunmire, *Corrosion Reviews*, 25 (3-4) (2007).
5. N.X. Xu, L.Y. Zhao, C.H. Ding, C.D. Zhang, R.S. Li, and Q.D. Zhong, *Corrosion Science*, 44(1), 163-170 (2002).
6. EN ISO 9223:1992. Corrosion of metals and alloys: Corrosivity of atmospheres: Classification, determination and estimation.
7. EN ISO 9224:1992. Corrosion of metals and alloys: Corrosivity of atmospheres: Guiding values for the corrosivity categories.
8. EN ISO 9225:1992: Corrosion of metals and alloys: Corrosivity of atmospheres; Measurement of Pollution.
9. EN ISO 9226:1992. Corrosion of metals and alloys: Corrosivity of atmospheres: Methods of determination of corrosion rates of standard specimens for the evaluation of corrosivity.
10. M. Morcillo, E. Almeida, B. Chico and D. de la Fuente, *Analysis of ISO Standard 9223 (Classification of Corrosivity of Atmospheres) in the Light of Information Obtained in the Ibero-American Micat Project; Outdoor Atmospheric Corrosion*, ASTM 1421, H. E. Townsend, Ed., Ed., American Society for Testing and Materials International, West Conshohocken, PA, 2002.
11. J. Tidblad, *Atmospheric Environment* 55 1-6 (2012).
12. Pourbaix, *Atmospheric corrosion*, John Wiley & Sons, 107 – 121, 1982.
13. McCuen et al. *ASTM STP 1137* 46-76 (1992).
14. S.R. Summitt, F.T. Fink, *Pacer Lime: An Environmental Corrosion Severity Classification System (AFWAL-TLER-80-4102 Part I)*, Metallurgy, Mechanics, and Materials Science, Michigan State University, 1980.
15. NATO Research and Technology Organization, *Corrosion Fatigue and Environmentally Assisted Cracking in Aging Military Vehicles (AG-AVT-140)*, 2011.
16. E.D. Kenny, E.J. Esmanhoto, *Tratamento estatvstico do desempenho de materiais metalicos no estado do Parana*, in: XVII Congresso Brasileiro de Corrosão, Rio de Janeiro, Anais, ABRACO, T-24, 297-308, 1993.
17. E.D. Kenny and E.J. Esmanhoto, *Corrosão do aço-carbono por intemperismo natural no Estado do Parana*, in: IV Seminário de Materiais no Setor Elétrico, Curitiba, Anais, Copel/UFPR, 1994, pp. 377–382.
18. S. Feliu, M. Morcillo and S. Jr. Feliu, *Corrosion Science* 34 403-414 (1993).
19. S. Feliu, M. Morcillo and S. Jr. Feliu, *Corrosion Science* 34 415-422 (1993).
20. L. Mariaca, M. Morcillo, *Funciones de dapo (dosis/respuesta) de la corrosion atmosferica en Iberoamerica: Programa CYTED. Seccion B-7, Gráficas Salu, Madrid*, 629-660, 1998.
21. J. Cai, R.A. Cottis and S.B. Lyon. *Corrosion Science* 41 2001-2030 (1999).
22. Z. Jančíková, O. Zimný and P. Košťal, *Metabk* 52(3) 379-381 (2013).
23. Y. Caia, Y. Zhaob, X. Maa, K. Zhouc and Y. Chenc, *Corrosion Science* 137 163-175 (2018).
24. A. A. Mikhailov, J. Tidblad, and V. Kucera, *Protection of Metals*, 40(6) 541-550 (2004).
25. University of the Aegean, Department of Environment http://www1.aegean.gr/lid/internet/elliniki_ekdosi/TEL_DIMOSI/Paper_Periferiakotita.pdf
26. Coastline lengths, <http://world.bymap.org/Coastlines.html>.

27. EN ASTM International. Designation:G140-02. Standard Test Method for Determining Atmospheric Chloride Deposition Rate by Wet Candle Method.
28. EN ISO 8407:1991. Corrosion of metals and alloys: Corrosivity of atmospheres: Removal of Corrosion Products from Corrosion Test Specimens.
29. EN ASTM International. Designation G1-90:1999. Standard Practice for Preparing, Cleaning, and Evaluating Corrosion Test Specimens.
30. EN ISO 4221:1980. Air quality Determination of mass concentration of sulphur dioxide in ambient air; Thorin spectrophotometric method.
31. EN ASTM International. Designation: G4458-94 (Reapproved 1999). Standard Test Method for Chloride Ions in Brackish Water, Seawater and Brines.
32. R.D. Klassen and P.R. Roberge, "The Effects of Wind on Local Atmospheric Corrosivity," Corrosion 2001, NACE International, Houston, 2001, Paper # 544.
33. Dean SW, Reiser DB. Analysis of data from ISO CORRAG Program. Corrosion 1998, Paper #340. Houston, TX: NACE International, 1998.
34. S.W. Dean and D.B. Reiser, Comparison of the atmospheric corrosion rates of wires and flat panels. Corrosion 2000, Paper #455. Houston, TX: NACE International, 2000.
35. S.W. Dean, Classifying atmospheric corrosivity - a challenge for ISO. Mater Perform 32(10) 53-58 (1993).
36. P.R. Roberge, R.D. Klassen and P.W. Haberecht, Mater. Design, 23 321–330 (2002).
37. S.W. Dean, Corrosion testing of metals under natural atmospheric conditions. In: Baboian R, Dean SW, editors. Corrosion testing and evaluation: silver anniversary volume. Philadelphia, PA: ASTM, 1990:163176.
38. D. Knotkova and F.N. Speller, Corrosion, 61 723-738, (2005).
39. C. Leygraf and T.E. Graedel, Atmospheric Corrosion, New York, NY, USA, John Wiley and Sons, 2000.
40. C. Titakis, "Quantitative chemical composition of Pachi airport atmosphere and effect of pollutants in aeronautical materials", Diploma thesis, National Technical University of Athens, Greece, 2013.
41. B.E. Psiloglou; Meteorological Data 2009-11, National Observatory of Athens, Institute for Environmental Research and Sustainable Development.
42. Climatology of Elefsina, http://www.hnms.gr/hnms/english/climatology/climatology_region_diagrams_html?dr_city=Elefsina
43. Hellenic Meteorological Service, http://www.emy.gr/hnms/english/index_html?
44. H.D. Kambezidis and G. Kalliampakos, Water Air Soil Pollution 224 1463 (2013).
45. Ministry of Environment and Energy, Air Quality Department, Annual Report of Air Pollution, 2016: <http://www.ypeka.gr/LinkClick.aspx?fileticket=81Y3zyY9w%2BU%3D&tabid=490&language=el-GR> (greek).
46. European Environmental Agency/ Sulphur Dioxide (SO₂): annual mean concentrations in Europe; site: <http://www.eea.europa.eu/themes/air/interactive/so2>.
47. EMEP MSC-W modeled air concentrations and depositions, http://webdab.emep.int/cgi-bin/webd2_controller.pl?State=ydata&reportflag=2015&countries=GR&years=2013&pollutants=total+ox.+sulphur&datatype=grid50_png.
48. EMEP MSC-W modeled air concentrations and depositions, http://webdab.emep.int/cgi-bin/webd2_controller.pl?State=ydata&reportflag=2015&countries=GR&years=2009&pollutants=SO2&datatype=grid50_png.
49. P.D. Kalabokas G. Sideris, M.N. Christolis and N.C. Markatos N.C., Analysis of Air Quality Measurements in Volos, Greece; Presented at the 5th International Exposition and Conference for Environmental Technology, HELECO, 2005.

50. EMEP MSC-W modeled air concentrations and depositions, http://webdab.emep.int/cgi-bin/webd2_controller.pl?State=ydata&reportflag=2015&countries=GR&years=2013&pollutants=O3&datatype=grid50_png.
51. A-N Riga-Karandinos and C. Saitanis, *Chemosphere* 59 1125-1136 (2005).
52. U. Ima, S. Christodoulaki, K. Violaki, P. Zampas, M. Kocak, N. Daskalakis, N. Mihalopoulos and M. Kanakidou, *Atmospheric Environment* 81 6 (2013).
53. V.G. Mossotti and A.R. Eldeeb, MORPH-2, a software package for the analysis of scanning electron micrograph (binary formatted) images for the assessment of the fractal dimension of exposed stone surfaces. U.S. Geological Survey, 2000.
54. H. Xiao, W. Ye, X. Song, Y. Ma and Y. Li, *Materials* 10 1262 (2017).
55. M. Pourbaix, "The linear bilogarithmic law for atmospheric corrosion". In *Atmospheric Corrosion*; Ailor, W.H., Ed.; The Electrochemical Society, John Wiley and Sons: New York, USA, 1982; pp.107–121.
56. EN ASTM G16-95, Standard guide for applying statistics to analysis of corrosion data, ASTM, Philadelphia, PA, USA 1999.
57. EN ASTM G 101-01, Standard guide for estimating the atmospheric corrosion resistance of low alloy steels, ASTM, Philadelphia, PA, USA 2001.
58. J. W. Spence, F. H. Haynie, F. W. Lipfert, S. D. Cramer, L. G. McDonald, *Atmospheric Corrosion Model for Galvanized Steel Structures*, *CORROSION*. 1992;48(12):1009-1019.
59. J. Kobus, *Mater. Corrosion* 51 104 (2000).
60. S. A. Abdul-Wahab, *Toxic Radioactive Waste Management* 7 190 (2003).
61. S. Bhattacharjee, N. Roy, A. K. Dey and M.K. Banerjee, *Corrosion Science* 34 573 (1993).
62. J. J. Santana Rodriguez, F. Javier Santana Hernandez and J. E. Gonzalez, *Corrosion Science* 45 799 (2003).
63. S.W. Dean and D.B. Reiser, *Analysis of Long-Term Atmospheric Corrosion Results from ISO CORRAG Program*, *Outdoor Atmospheric Corrosion*, STP 1421, H.E. Townsend, Ed., American Society for Testing and Materials, 2002, p 3–18
64. H. E. Townsend, *Corrosion* 57(6), 497-501 (2001).
65. M. Morcillo, B. Chico, D. de la Fuente, and J. Simancas, *Int. J. Corrosion* 12 (2012).
66. R. Ericsson, *Werkstoffe und Korrosion*, 29(6), 400–403, (1978).
67. S. Oesch, *Corrosion Science* 38, 1357 (1996).
68. S.C. Chung, A.S. Lin, J.R. Chang, H.C. Shih, *Corrosion Science* 42, 1599-1610 (2000).
69. J.E. Svensson, L.G. Johansson, *J. Electrochem. Soc.* 140, 2210 (1993).
70. X. Odnevall and C. Leygraf, *Corros. Sci.* 36, 1551 (1994).
71. K.A. van Geteren, *Galvanotechnik* 72, 35 (1981).
72. E. Johansson and J. Gullman, *KI Rapport 7*, Swedish Corrosion Institute, 1991.
73. C. J. Slunder and W. K. Boyd, *Zinc: Its Corrosion Resistance*, ILZRO, New York, NY, USA, 1983.
74. C. Mitsakou, G. Kallos, N. Papantoniou, C. Spyrou, S. Solomos, M. Astitha, and C. Housiadas. Saharan dust levels in Greece and received inhalation doses. *Atmos. Chem. Phys.*, 8, 7181-7192, 2008.
75. EN ISO 8993:1989. Anodized aluminium and aluminium alloys - rating system for the evaluation of pitting corrosion – Chart method.

Thermodynamic Analysis of the Effect of Compression and Injection Quality Faults on DI Diesel Engine Combustion and Performance Characteristics

John S. Katsanis^a, Marios I. Kourampas^a, Elias A. Yfantis^a, Efthimios G. Pariotis^a and Theodoros C. Zannis^a

*^aNaval Architecture and Marine Engineering Section, Hellenic Naval Academy,
End of Hatzikiriakou Ave. 18539 Piraeus, Greece*

Abstract. In the present study a closed-cycle diesel engine simulation code based on a multi-zone combustion model was used to simulate three diesel engine faulty operation cases i.e. reduction of mean injection pressure, reduction of fuel injected mass per engine cycle and reduction of compression ratio. The multi-zone combustion model upon successful experimental validation was used to generate theoretical results for cylinder pressure, fuel evaporation rate and bulk gas temperature for each one of the previously mentioned engine faulty operation cases. The predicted cylinder pressure profiles were supplied to a computational model developed in MATLAB under a diploma thesis conducted in Hellenic Naval Academy in order to perform a heat release rate analysis and to derive the main performance characteristics of the examined diesel engine. The MATLAB model was used to derive results for heat release rate, heat losses rate, ignition angle and ignition delay and premixed phase, diffusion-controlled and total combustion durations. The assessment of all theoretical results for combustion parameters and engine performance characteristics showed that the reduction of mean injection pressure and the pertinent reduction of compression ratio affected negatively the diesel engine combustion mechanism by decreasing ignition angle and thus, shifting combustion event to the expansion stroke and, by increasing total combustion duration. The reduction of fuel consumption resulted in noticeable reduction of engine power and efficiency due to reduction of engine supplied heating power whereas, it did not affect seriously the time evolution of the combustion event inside the combustion chamber.

Keywords: diesel engine; injection pressure; fuel consumption; compression ratio; performance

INTRODUCTION

Diesel engine is world-known for its superior thermal efficiency among all other thermal engines [1]. The evolution of electronically-controlled fuel injection systems and the pertinent advances in turbocharging systems have led in the development of advanced technology diesel engines for various applications i.e. automotive, marine, electric power generation etc. with considerably lower brake specific fuel consumption (BSFC) and increased power density compared to recent past. As a characteristic example today marine four-stroke medium-speed

diesel engines have a minimum BSFC of 170 g/kWh whereas, the pertinent minimum BSFC of modern two-stroke slow-speed diesel engines is close to 156 g/kWh. Besides the need for minimization of specific fuel consumption and maximization of power density, there is a continuous requirement from diesel engines in all the fields of their application for high availability and reliability. The requirement for high availability from diesel engines is directly related with the minimization of the time that the engine is out of operation due to maintenance issues or in other words, is directly related with the unexpected faults of a diesel engine. Hence, it is of utmost importance not only the reduction of maintenance time by developing effective maintenance techniques but also the development of sophisticated techniques for the continuous monitoring and assessment of diesel engine operation and the utilization of monitoring data for the development of effective diagnostic techniques. Successful implementation of diagnostic techniques in diesel engines can lead to the tracking of a faulty operation cause by proposing specific measures for the healing of the specific problem and there are reported cases that diesel engine diagnosis have led to the prevention of catastrophic damages reducing thus, substantially the corresponding maintenance cost [2,3].

Studies performed in the past have demonstrated the multiple virtues of diesel engine monitoring and preventive maintenance technologies and have sorted the relative importance of various faulty situations often appeared in diesel engines [4,5]. Published studies have also exposed the beneficial effect of diesel engine continuous monitoring not only to the identification of faulty operation cases but also to diesel engine optimized operational and environmental behaviour [2,3,6]. Various technologies have been proposed in the literature for the monitoring and diagnosis mainly of large-type two-stroke slow-speed and heavy-duty four-stroke medium-speed marine diesel engines, which differ on the type of measuring data obtained from the engine and the pertinent technique used for their processing and assessment. One of the most prominent and world-known monitoring and diagnostic techniques is the one proposed by Hountalas et al. [2,3,7], which is based on the measurement of the cylinder pressure and the development of a sophisticated thermodynamic method for tracking TDC without measuring equipment and for processing the measured cylinder pressure data for assessing current diesel engine operational status, tracking the cause of unpleasant faulty situations and in such case proposing specific healing measures and for projecting its performance trends in the future. Another category of diesel engine diagnostic technique concerns the measurement of torsional vibrations and the processing the obtained torsional vibration data for tracking mainly the cylinder that does not contributing equally to the torsional vibration profile of the crankshaft [8,9]. The measurement and processing of torsional vibration data through that it can track faulty cylinder it cannot identify, unlike the previously mentioned thermodynamic method, the cause of faulty cylinder operation. Another technology proposed for diesel engine monitoring and diagnosis is the measurement and processing of mechanical vibration data obtained from various positions on the engine i.e. turbocharger, crankcase, camshaft case etc. [10,11]. The processing of vibration data is based on the derivation of RMS and the vibration spectrum for each diesel engine component and then the comparison of the derived vibration spectrum with exemplary vibration spectrums corresponding to specific faulty conditions such as shaft misalignment. Hence, though that the analysis of measured vibration data can identify the mechanical problem of a faulty engine component it cannot directly identify the potential thermo-fluid cause of this mechanical problem. Also, after-engine technologies such as diesel engine oil analysis have been extensively used for characterizing engine operational status [12]. The advancement of information

technology during recent years have also led to the implementation of information fusion techniques for diesel engine condition monitoring and fault diagnosis [13].

All the previously mentioned monitoring and diagnostic techniques have predominantly been implemented in large-type diesel engines such as marine two-stroke slow-speed engines, where the slow evolution of combustion event and high inertias of reciprocating and rotating masses facilitate the tracking of a faulty engine operating situation by either thermodynamic or mechanical cause. Also, most of the already published thermodynamic diagnostic studies have emphasized on the assessment of engine performance data without elucidating completely the effects of a faulty situation or engine component on the combustion mechanism. For this reason, in the present study an effort is made to shed light into the effect of specific faulty operating cases on the combustion mechanism and the pertinent performance characteristics of a small light-duty high-speed direct injection (DI) diesel engine. Specifically, it is theoretically examined the effect of faulty fuel injection system operation, which is modelled either as reduction of mean fuel injection pressure compared to its nominal value at a specific operating point or as reduction of fuel injected mass per engine cycle compared to its nominal value. Also, it is theoretically investigated the impact of faulty compression quality, which is modelled as reduction of compression ratio compared to its nominal value for the examined DI diesel engine. An engine closed-cycle simulation model is used to simulate the operation of a four-stroke high-speed DI diesel engine (“Lister LV1”) under various mean injection pressures, fuel consumptions and compression ratios generating theoretical results for cylinder pressure, fuel evaporation rate and bulk gas temperature. Predicted cylinder pressure profiles are then supplied to a computational model developed in MATLAB under a diploma thesis conducted in Hellenic Naval Academy in order to perform a heat release rate analysis and to calculate main engine performance parameters. The evaluation of all theoretical results for combustion parameters and engine performance characteristics revealed that either the reduction of mean injection pressure or the reduction of compression ratio affected negatively the diesel engine combustion mechanism by delaying combustion initiation and, by increasing total combustion duration. The reduction of fuel injected mass per engine cycle resulted in significant reduction of engine power and efficiency due to reduction of engine supplied heating power whereas, it did not affect seriously commencement and the duration of the combustion event inside the combustion chamber.

DIESEL ENGINE DESCRIPTION

The diesel engine considered in the present study (“Lister LV1”) is a four stroke, air cooled single-cylinder high-speed DI diesel engine, which is equipped with a bowl-in-piston. “Lister LV1” diesel engine has a cylinder bore of 0.08573m, a piston stroke of 0.08255 m and the connecting rod length is 0.1885m [14,15]. The compression ratio of “Lister LV1” diesel engine is 17:1 and its nominal speed range varies from 1000 to 3000 rpm. Diesel fuel is injected in “Lister LV1” engine through a three-hole injector (nozzle orifice diameter 250 μ m), which is located at the center of the combustion chamber and its opening pressure is 180 bar. “Lister LV1” engine is coupled with a Heenan & Froude hydraulic dynamometer at the premises of the Internal Combustion Engines Laboratory of National Technical University of Athens, Greece [14,15].

DESCRIPTION OF THE DIESEL ENGINE CLOSED-CYCLE SIMULATION MODEL

A two-dimensional multi-zone combustion model was used to simulate the physical and chemical phenomena that take place inside combustion chamber during closed cycle operation (intake and exhaust valves are closed). This model has been previously developed under a PhD thesis using the long-standing experience developed in the Laboratory of Internal Combustion Engines of National Technical University of Athens [16-20]. According to this model, the fuel jet coming out from each nozzle orifice during injection process is divided into distinctive control volumes, which are called “zones”. Each fuel jet zone is treated as an open thermodynamic system, which exchanges energy and mass with its surroundings. The division of each fuel jet into zones allows the prediction of the temperature and the chemical composition of each zone at each crank angle integration step. In Figure 1 is given a representative schematic vies of the division of one fuel jet into zones at the axial and at the radial direction. It is given also in Figure 1 the effect of swirled air flow field on the formulation of the fuel jet shape [14,16-20].

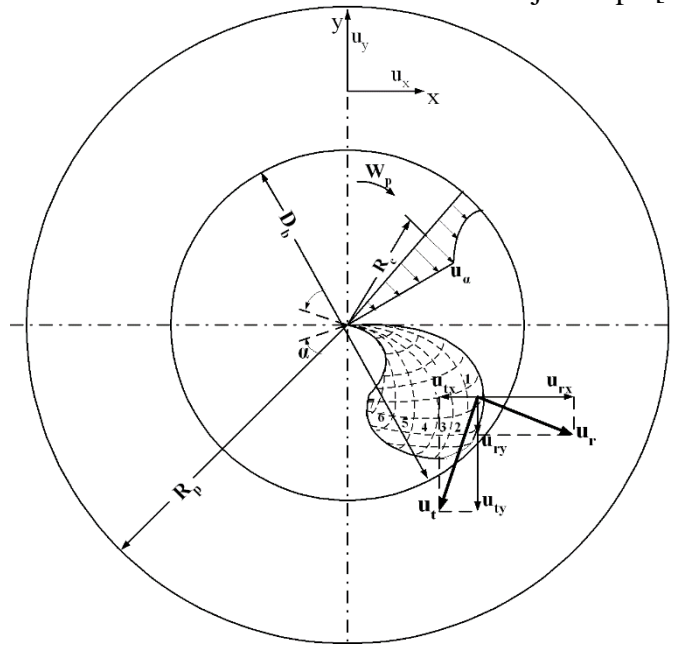


FIGURE 1. Schematic view of the swirled air flow field and one of the fuel jets on a plane perpendicular to the cylinder axis [14,19,20]

The thermodynamic conditions in each zone are calculated using the first law of thermodynamics and the mass and momentum conservation laws whereas the pressure inside the cylinder is considered uniform. Fuel jet zone temperature rate of variation depends directly from the energy released inside the zone due to the vaporized fuel and entrained air, zone heat losses, zone gas mixture internal energy and elementary technical work variation. Combining all these equations a final ordinary differential equation (ODE) is derived, which is numerically solved using a predictor – corrector scheme for predicting the cylinder pressure variation inside the cylinder. After numerically solving the ODE for cylinder pressure, several ODEs are also numerically solved using a predictor – corrector explicit method for predicting the instantaneous gas temperature inside each fuel jet zone [14,19,20].

Modeling of the Physical and Chemical Processes of the Four-Stroke Diesel Engine Closed Cycle

In-cylinder Heat Losses Modeling

The heat loss rate between the in-cylinder gas and the combustion chamber walls is calculated using the following relation [21]:

$$\dot{Q} = A \left[h(T_g - T_w) + c\sigma(T_g^4 - T_w^4) \right] \quad (1)$$

where:

- A is the instantaneous heat transfer area of the cylinder walls.
- T_w is the mean temperature of the cylinder walls, which is assumed to be invariable in space and time.
- σ is Stefan – Boltzmann constant
- c is a constant equal to 1.5.
- T_g is the bulk in-cylinder gas temperature at each crank angle step, which is predicted from the following equation:

$$T_g = \frac{\sum_{i=1}^{n+a} m_i c_{vi} T_i}{\sum_{i=1}^{n+a} m_i c_{vi}} \quad (2)$$

The first term in Eq. (1) corresponds to the heat losses of in-cylinder gas due to convection whereas, the second term in Eq. (1) corresponds to the radiation losses of the in-cylinder working medium. The instantaneous heat transfer rate calculated by Eq. (1) is distributed in fuel jet zones according to their individual temperature, mass and specific heat capacity as follows [22,23]:

$$\frac{d\dot{Q}_{i,w}}{d\varphi} = \dot{Q}(m_i c_{vi} T_i) / \sum_{i=1}^{n+a} m_i c_{vi} T_i \quad (3)$$

Convection heat transfer coefficient h is given by the following relation assuming the existence of in-cylinder heat and fluid flow conditions like the ones of fully developed flow over a flat plate [24]:

$$h = c_h Re^{0.8} Pr^{0.33} (\lambda / \ell_{char}) \quad (4)$$

where Re is the dimensionless Reynolds number, Pr is the dimensionless Prandtl number, λ is the thermal conductivity of the in-cylinder gaseous medium and ℓ_{char} is the characteristic length. The characteristic mean velocity of the in-cylinder bulk gas used for the calculation of the Reynolds number is given by:

$$\bar{u} = (u^2 + u_T^2 + u_p^2)^{0.5} \quad (5)$$

where u_p is the instantaneous piston velocity, which is a function of cylinder geometrical dimensions [1]. Reynolds and Prandtl numbers are calculated as follows:

$$Re = \frac{\bar{u} \ell_{char} \rho}{\mu}, \quad Pr = \frac{\mu c_p}{\lambda} \quad (6)$$

A dimensionless turbulent kinetic energy (k-ε) model is used for the prediction of u and u_t velocities [25].

Air Swirl Model – Prediction of Intake Air Angular Velocity

Air angular velocity inside the combustion chamber is calculated by solving the angular momentum conservation law. It should be noted here, that in many cases, intake air is inducted in the engine combustion chamber with angular momentum as a result of its rotation around cylinder vertical axis. This motion of the intake air is called “Swirl” and it is usually in small-bore diesel engines, which are equipped with bowl-in-piston. Swirl motion is applied to prevent the fuel jet impingement to the bowl-in-piston walls and thus, to avoid the temporarily cooling of impinged fuel due to its heat loss to piston bowl walls. In most of the cases, the amount of impinged fuel cannot be burned completely enhancing thus, the formation rate of unburned hydrocarbons. In general, intake air swirled induction inside the cylinder promotes air entrainment inside fuel jet improving thus, local fuel-air mixing.

The solution of the angular momentum conservation equation requires the knowledge of the swirled intake air tangential velocity. Hence, it is assumed that the tangential intake air profile on a plane perpendicular to the cylinder longitudinal axis is a hybrid scheme comprised of a solid core, which is surrounded by a flow field. This hybrid scheme considers the air viscosity, which creates a boundary layer close to the combustion chamber walls [26]. The tangential air velocity profile is given by the following relation [1]:

$$\left. \begin{aligned} u_t &= W_p R & \gamma \alpha & 0 \leq R \leq R_c \\ u_t &= W_p R_c (R_c/R)^n & \gamma \alpha & R_c \leq R \leq R_p \end{aligned} \right\} \quad (7)$$

where u_t is the tangential air velocity, W_p is the angular air velocity, n is an exponent which varies from 0 to 0.1 and R_c is the air solid core rotation radius, which is calculated as follows:

$$R_c = R_m (D_b/2R_p) \quad (8)$$

Consequently, for a given combustion chamber geometry and known angular air velocity W_p, the tangential air velocity profile can be calculated using Eqs (7) and (8).

For the calculation of the angular air velocity W_p, a simple scheme of “air solid core rotation” is used, where the angular momentum conservation equation is applied for the combustion chamber gaseous content [27]. The value of air angular velocity when the intake valve is closed corresponds to the initial value of air angular velocity and it is an input value of the closed-cycle simulation model expressed as the ratio of air angular velocity to the engine rotational speed (i.e. swirl ratio). This value is obtained from relevant experimental data. The conservation law of angular momentum in differential form is given by:

$$\frac{d(IW)}{dt} = I \frac{dW}{dt} + W \frac{dI}{dt} = -M_r \quad (9)$$

The rotating moment of inertia I of the in-cylinder gas is calculated as follows:

$$I = \frac{1}{2} m_a \frac{R_p^2 S_p + (D_b/2)^4 S_b}{R_p^2 S_p + (D_b/2)^2 S_b} \quad (10)$$

where m_a is the mass of the trapped in-cylinder gas. The resulting rotating torque M_r , which act on the fluid is:

$$M_r = M_{cyl} + M_{p-c} \quad (11)$$

where M_{cyl} is the resistance torque to the in-cylinder fluid flow due to its contact with combustion chamber walls and M_{p-c} is the generating torque due to the friction of the in-cylinder gas with the piston crown and the cylinder head. Fluid resistance torque is given by the expression:

$$M_{cyl} = \tau_{cyl} A_{cyl} R_p = \left(\frac{1}{2} f_{cyl} \rho_a u_{tRp}^2 \right) 2\pi R_p^2 S_p \quad (12)$$

Where u_{tRp} is the tangential air velocity at radius R_p , which, according to Eq (7), is calculated as follows:

$$u_{tRp} = W_p R_c \left(R_c / R_p \right)^n \quad (13)$$

Combining Eqs (12) and (13) it is finally obtained:

$$M_{cyl} = f_{cyl} \pi W_p^2 R_p^2 R_c^2 \left(R_c / R_p \right)^{2n} S_p \quad (14)$$

Friction coefficient f_{cyl} of the in-cylinder gas motion is calculated assuming again the same conditions with the ones of the fully developed fluid flow over a flat plate:

$$f_{cyl} = 0.058 Re^{-0.2} \quad (15)$$

The cylinder bore (equal to $2R_p$) and the air velocity u_{tRp} are used as characteristic length and as characteristic velocity respectively to calculated Reynolds number. The rotating torque due to air friction at the piston top head and at the cylinder head is assumed that it acts on the cylinder mean radius ($R_p/2$) and that it is the same with the one calculated as fluid friction between two flat plates. According to this assumption, the torque M_{p-c} is calculated using the following equation [1]:

$$M_{p-c} = 2 \left(\tau_{p-c} A_{p-c} R_p / 2 \right) = \left(\frac{1}{2} f_{p-c} \rho_a u_{tRp/2}^2 \right) \pi R_p^3 \quad (16)$$

where $u_{tRp/2}$ is the tangential air velocity at radius $R_p/2$, which is calculated as follows:

$$u_{tRp/2} = W_p \left(R_p / 2 \right) \quad (17)$$

Finally, the generating torque M_{p-c} due to the friction of the in-cylinder gas with the piston crown and with the cylinder head is estimated according to the following relation:

$$M_{p-c} = f_{p-c} \pi \rho_a W_p^2 \left(R_p^5 / 8 \right) \quad (18)$$

Friction coefficient f_{p-c} is calculated from Eq. (15) using radius R_p as characteristic length and air velocity $u_{tRp/2}$ for the calculation of the pertinent Reynolds number.

Fuel Jet Development Model

Fuel injected mass per crank angle integration step is divided into n_f zones through fuel jet, where n_f is an odd number. Hence, fuel jet zones are arranged proportionally on either side of the

longitudinal axis of the fuel jet. Fuel injected mass m_f per engine cycle is distributed into zones as follows [14,16-18,20]:

$$m_{f,i} = \frac{A_{ho,i}}{A_{ho}} m_f \quad (19)$$

Where $A_{ho,i}$ is a predefined portion of the total injector nozzle area A_{ho} . At next, as a certain crank angle degree step $\Delta\phi$ has passed from the beginning of the fuel injection process, a new group of “n” fuel jet zones is formed following the same path as previously described. This process is continued until the completion of the fuel injection process. The axial velocity of each fuel jet zone is calculated by adopting the following semi-empirical relation [14,16-18,20]:

$$\begin{cases} u_{x,i} = \left(\frac{\Delta X_0}{\Delta X_{x,i}} \right)^{n_i}, & \gamma \alpha \Delta X_{x,i} > 6.57 d_{ho} = \Delta X_0 \\ u_{inj} & \\ u_{x,i} = u_0, & \gamma \alpha \Delta X_{x,i} \leq 6.57 d_{ho} \end{cases} \quad (20)$$

where $i = 1$ and $i = n_r$ represent the leading and the trailing zone respectively. A linear distribution with respect to number of radial jet zones is used for the calculation of exponent n_i , which varies from 0.7 to 0.9 from the internal to the external zones. The initial value of the radial component of the fuel jet velocity is estimated as follows:

$$u_{r,i} = u_{inj} \tan \left(\frac{\theta_0}{r_0} r_i \right) \quad (21)$$

where r_0 is the radius of the injector nozzle as presented in Figure 2 and r_i is the radial distance of fuel jet zone “i” from the central lines.

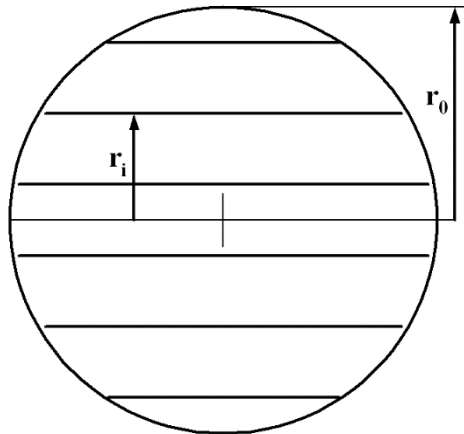


FIGURE 2. Fuel jet distribution into radial zones [14,20]

The fuel jet cone angle at the exit of the injector nozzle is calculated using the following relation [1,28]:

$$\theta_0 = 0.05 \left(\frac{d_{inj}^2 \rho_a \Delta P}{\mu_a^2} \right)^{0.25} \quad (22)$$

The local fuel jet cone angle is calculated afterwards from the fuel jet geometry as it results from the local radial and axial velocities of the external fuel jet zones. Calculating the local air velocity components in both radial and axial directions and using the momentum conservation

equations in both axes, the effect of air swirl on fuel jet geometry can be considered. From the procedure it results that the axial fuel jet penetration is reduced leading to a rapid deceleration of the fuel jet and thus, to the increase of the air entrainment rate. Due to air swirl inside the combustion chamber, fuel jet zones deviate from the initial direction and as result an increase of air entrainment rate is observed inside fuel jet zones. Fuel jet zone deviation from the initial direction is calculated considering local air velocities as follows:

$$\left. \begin{aligned} u_{tx,i} &= u_{x,i} + u_t \sin(\theta_i) \\ u_{tr,i} &= u_{r,i} - u_t \cos(\theta_i) \end{aligned} \right\} \quad (23)$$

Where u_t is the local air swirl velocity and θ_i is the angular position of each fuel jet zone inside the combustion chamber. The above-mentioned equations are implemented for the cases before and after the fuel jet impingement to the combustion chamber walls. The well-tested theory of Glauert for the interaction of fuel jet and combustion chamber walls [29,30] is used for the determination of the time evolution of the fuel jet zones after the jet impingement to the combustion chamber walls. According to this theory, fuel jet zone velocity after impingement is given by the following equation:

$$w_i = w_{0,i} \left(\frac{r_{0,i}}{r_i} \right) \quad (24)$$

Where $r_{0,i}$ is the initial radial zone position with respect to the jet axis after impingement and $w_{0,i}$ is the initial velocity. It is assumed that the fuel jet zone follows a path alongside the combustion chamber walls, where its radial distance “ δ ” from the wall determines the thickness of the fuel jet boundary layer on the combustion chamber wall and is given from the relation [22,23,29]:

$$\delta_i = \delta_{0,i} \left(\frac{r_i}{r_{0,i}} \right) \quad (25)$$

where $\delta_{0,i}$ is the initial zone distance from the combustion chamber wall after the impingement. Before the jet impingement the velocities are divided into two components: One perpendicular and one parallel to the combustion chamber walls. After this, the part of fuel jet zone, which corresponds to the parallel velocity deviates completely whereas, the perpendicular part of zone is divided into two parts: The right and left part. Hence, the zone part, which has velocity opposite to the parallel velocity component is considered to create a new zone. The initial values for $w_{0,i}$ and $\delta_{0,i}$ are determined by applying the mass and the energy conservation laws taking also into consideration the local fuel jet geometry [22].

Air entrainment rate into zones is determined using the momentum conservation law for the injected fuel. Air entrainment rate is obtained from the following expression [28,31]:

$$m_f u_{inj} = (m_f + m_a) u \quad (26)$$

The left-side part of the previous equation is equal to the initial zone momentum whereas, the right-side part corresponds to the zone momentum after time “ t ”. Differentiating both sides of the previous equation is obtained the following differential equation for the air entrainment rate:

$$u \frac{dm_a}{dt} = -(m_a + m_f) \frac{du}{dt} \quad (27)$$

Hence, having given the instantaneous total air mass entrained into zones from the beginning, is calculated the air entrainment rate at each integration crank angle degree step. It should be mentioned that the entrained air into fuel zones results in their deceleration.

Fuel Atomization Model

Inside each fuel jet zone, fuel is split into packages (i.e. groups), in which all fuel droplets have the same “Mean Sauter Diameter – SMD”. The “Mean Sauter Diameter (D_{SM})” is obtained from the following semi-empirical relation, which has been derived from experimental data analysis [31]:

$$D_{SM,1} = 0.38 Re_{inj}^{0.25} We_{inj}^{-0.32} \left(\frac{\nu_l}{\nu_a} \right)^{0.37} \left(\frac{\rho_l}{\rho_a} \right)^{-0.47} d_{inj} \quad (28)$$

$$D_{SM,2} = 4.12 Re_{inj}^{0.12} We_{inj}^{-0.75} \left(\frac{\nu_l}{\nu_a} \right)^{0.54} \left(\frac{\rho_l}{\rho_a} \right)^{0.18} d_{inj}$$

Where the indices “1” and “2” denote complete and incomplete fuel jets respectively. In the previous relation, We is the dimensionless Weber number, ν_l , ρ_l are the kinematic viscosity and the density of the liquid fuel droplet, ν_a , ρ_a are the kinematic viscosity and the density of the surrounding air and d_{inj} is the injector nozzle orifice diameter. The mean droplet diameter is obtained as the maximum of these two values. By this modelling approach is taken into consideration the effect of fuel physical properties.

Fuel Vaporization Model

The well-known model of Borman and Johnson [32] is used for the modeling of the vaporization process of the liquid fuel inside each jet zone. This model succeeds in describing effectively the fuel vaporization phenomenon taking into consideration the coupled heat and mass transport phenomena that take place at the fuel droplet – air interface. According to the model of Borman and Johnson the reduction rate of a fuel droplet radius due to vaporization is given by the following relation:

$$\frac{dr}{dt} = -\frac{\rho_a}{\rho_l} \frac{D_{af}}{2r} Sh \ln \left[1 + \left(\frac{y_s - y}{1 - y_s} \right) \right] \quad (29)$$

where:

- ρ_a is the air density in kg/m^3 .
- ρ_l is liquid fuel density in kg/m^3 .
- D_{af} is the liquid diffusion coefficient to the gas phase in m^2/s .
- r is the fuel droplet radius in m .
- y is the fuel mass concentration of the gas phase zone around the droplet.
- y_s is the fuel mass concentration at the droplet surface, which is calculated as follows:

$$y_s = \frac{MB_f p_{vp}}{MB_f p_{vp} + MB_a (p - p_{vp})} \quad (30)$$

where:

- MB_f is the fuel molecular weight.
- MB_a is the air molecular weight.
- p is the in-cylinder pressure at each crank angle degree integration step.
- p_{vp} is the fuel vapor pressure, which at the droplet surface is considered equal to the corresponding fuel partial pressure.

It should be mentioned that analytical correlations based on experimental data for the n-dodecene ($C_{12}H_{24}$) were used for the calculation of the liquid fuel thermophysical properties [14].

The energy balance between liquid droplet and surrounding air taking into consideration the latent heating of the liquid droplet and its mass reduction due to evaporation is expressed as follows [32,33]:

$$m_l c_{pl} \frac{dT_l}{dt} - 4\pi r^2 \rho_l \Delta h_v \frac{dr}{dt} = 4\pi r^2 \dot{q} \quad (31)$$

The first term of the Eq. (31) express the required heat for the droplet sensible heating and becomes zero when the droplet temperature becomes equal to saturation temperature T_s . The second term of the Eq, (31) expresses the latent heat of vaporization. This means that droplet temperature remains constant and equal to saturation temperature T_s . The second part of the Eq. (31) expresses the total heat, which is offered from the droplet surrounding environment (gaseous mixture of surrounding air and gaseous fuel) for its heating and evaporation. It is assumed that all fuel droplets of each jet zone (at the time instant each jet zone is injected) have initially the same diameter equal to the Sauter Mean Diameter (SMD). Each jet zone fuel evaporation rate relates to fuel droplet evaporation rate as follows [16,18]:

$$\frac{dm_{ev,i}}{dt} = N_{d,i} \frac{dm_{ev,d,i}}{dt} \quad (32)$$

where the index “i” denotes the increasing zone number, the index d refers to droplet whereas, $N_{d,i}$ is the number of droplets of fuel jet zone “i”. Hence, fuel jet zone evaporation rate is calculated as follows:

$$\frac{dm_{ev,i}}{dt} = N_{d,i} \left[2\pi \rho_a D_{af} Sh \ln \left[I + \left(\frac{y_s - y}{I - y_s} \right) \right] \right]_i \quad (33)$$

The heat flux \dot{q} absorbed by each droplet is calculated according to the following relation:

$$\dot{q} = \frac{\lambda_a (T - T_l)}{2r} Nu \frac{\ln \left[I + \left(\frac{y_s - y}{I - y_s} \right) \right]}{\left(\frac{y_s - y}{I - y_s} \right)} \quad (34)$$

Hence, the total amount of heat offered to fuel jet zone “i” for its heating and evaporation is:

$$\frac{d\dot{Q}_{ev,tot,i}}{dt} = N_{d,i} (4\pi r^2 \dot{q}) \quad (35)$$

Consolidating all above-mentioned information, the total fuel evaporation rate is:

$$\frac{dm_{ev,tot}}{dt} = \sum_{i=1}^n \frac{dm_{ev,i}}{dt} \quad (36)$$

Integrating Eqs (29), (31) and (33) for each zone it is calculated the droplet radius, the droplet temperature, which is equal to jet zone fuel temperature, and the fuel evaporated mass. Calculated droplet temperature T_1 is further used for the prediction of the mean temperature T_m of the gaseous film, which is formed during evaporation around each droplet [16,18,33]:

$$T_m = \frac{T_a + 2T_1}{3} \quad (37)$$

Temperature T_m is the temperature used for the calculation of the thermophysical properties of the gaseous mixture formed due to fuel evaporation around the droplet. Regarding the total heat supplied to the liquid fuel of each jet zone, it is considered that is partially attributed to the jet zone itself and partially to fuel jet surrounding air as follows [16,18]:

$$\frac{d\dot{Q}_{ev,tot,i}}{dt} = \frac{d\dot{Q}_{ev,i}}{dt} + \frac{d\dot{Q}_{ev,a,i}}{dt} \quad (38)$$

where the index “ α ” denotes the air zone. The contribution of each zone $d\dot{Q}_{ev,i}$ and the corresponding contribution of jet surrounding air $d\dot{Q}_{ev,a,i}$ to the total evaporation heat supplied to each jet zone $d\dot{Q}_{ev,tot,i}$ is determined by the following relation:

$$\left. \begin{aligned} \frac{d\dot{Q}_{ev,i}}{dt} &= \frac{m_l T_1}{m_l T_1 + m_a T_a} \frac{d\dot{Q}_{ev,tot,i}}{dt} \\ \frac{d\dot{Q}_{ev,a,i}}{dt} &= \frac{m_a T_a}{m_l T_1 + m_a T_a} \frac{d\dot{Q}_{ev,tot,i}}{dt} \end{aligned} \right\} \quad (39)$$

Ignition Delay Model

For the calculation of the ignition delay the following relation was used, which has been proposed by Assanis et al. [34] and it takes into consideration the value of the local fuel/air equivalence ratio Φ inside the combustion chamber:

$$S_{pr} = \int_0^I \frac{1}{a_{del} p_g^{-2.5} \Phi_{eq}^{-1.04} \exp(5000/T_g)} dt \quad (40)$$

where “ Φ_{eq} ” is the local fuel/air equivalence ratio, T_g is the local gas temperature and p_g is the in-cylinder pressure. Fuel is ignited locally in the jet zone, where the integral of Eq. (40) becomes equal to unity and the time interval between fuel injection timing angle and ignition angle is considered as ignition delay. The selection of this ignition delay model was made since it takes into consideration the local fuel/air equivalence ratio, the local zone temperature and the in-cylinder pressure.

Combustion Rate Prediction Model

The mathematical model used for the prediction of fuel combustion rate takes into consideration the local stoichiometric fuel/air ratio and the local temperature. This model is literally an Arrhenius relationship, which includes the cylinder pressure, the local zone

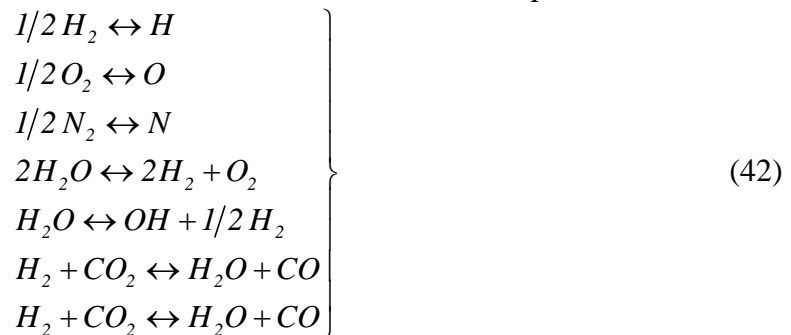
temperature and the local fuel availability with respect to entrained air in each zone. Hence, according to the model of Hodgetts and Shroff [35], the premixed combustion rate is given by the following relation:

$$\frac{dm_{bu,i}}{dt} = c_{bu} P^{0.757} \exp\left(-\frac{4500}{T_i}\right) \times \min\left[m_{f,ev,i}, m_{a,av,i} FA_{st}\right] \quad (41)$$

The term $\min\left[m_{f,ev,i}, m_{a,av,i} FA_{st}\right]$ denotes the dependence of the premixed combustion rate from the fuel vapor and the available entrained air in each jet zone. Equation (41) is implemented for each jet zone and it is numerically integrated for the derivation of the local premixed combustion rate. The model of Eq. (41) is not used for the prediction of diffusion combustion rate since this rate is controlled by the air entrainment rate in each fuel jet zone.

Combustion Products Dissociation – Chemical Equilibrium Scheme

It is well known that due to high in-cylinder temperatures the products of perfect combustion are further dissociating to a number of species, which in most cases is limited to the following 11 ones: N_2 , O_2 , CO_2 , H_2O , CO , H_2 , NO , OH , N , H , O [36-40]. Chemical equilibrium reactions, which describe the formation of the above-mentioned eleven dissociation species are [37]:



where K_{pir} are the equilibrium constants ($ir = 1, 2, \dots, 7$). Various approaches have been proposed in the literature for the numerical solution of the chemical equilibrium equations [36-40]. The common reference point of all numerical methods is the derivation of a non linear 11 x 11 system for the equilibrium concentration of the above-mentioned species using the definition equations of chemical equilibrium constants of the 7 above-mentioned reactions and the C, H, O and N balances between perfect combustion reactants and products. The numerical methods proposed for the solution of the above-mentioned chemical equilibrium scheme differ in terms of the numerical method used for the solution of the non linear algebraic system. In the present study the numerical method of Olikara and Borman [39] was used for the solution of chemical equilibrium equations in each modified version for the 11 species as it was suggested by Rakopoulos et al. [37].

BRIEF DESCRIPTION OF MATLAB MODEL USED FOR HEAT RELEASE RATE ANALYSIS AND FOR THE CALCULATION OF ENGINE COMBUSTION AND PERFORMANCE CHARACTERISTICS

A computational model was developed in MATLAB under a diploma thesis performed in Hellenic Naval Academy for performing heat release rate analysis and for calculating the main

combustion and performance characteristics of the examined diesel engine under varying injection pressure, fuel consumption and compression ratio. The specific model was initially developed for processing raw experimental data for cylinder pressure, injection pressure and TDC position from an experimental diesel engine under various operating conditions and for deriving the mean cylinder pressure and mean injection pressure profile. In the present study the developed MATLAB model was modified in order to use the cylinder pressure profiles generated by the closed-cycle simulation model (i.e. multi-zone combustion model) for different mean injection pressures, engine fueling rates and compression ratios for performing a heat release rate analysis and for calculating the main combustion and performance characteristics of the examined experimental diesel engine. The heat release rate analysis performed by the developed MATLAB model is based on the combination of the first law of thermodynamics for a closed thermodynamic system and the ideal gas equation of state for deriving gross and net heat release rates considering instantaneous in-cylinder gas heat losses, which were calculated using the well-known Annand's heat transfer model. In addition, the MATLAB model calculates the main combustion and performance characteristics of the examined experimental diesel engine such as indicated power, Indicated Specific Fuel Consumption (ISFC), peak cylinder pressure, ignition delay, ignition angle and the combustion durations corresponding to 5%, 25%, 50% and 90% of injected fuel mass burned.

TEST CASES EXAMINED

To examine the effect of the faults related to injection and compression quality the following cases were considered:

- Reduction of injection pressure compared to the nominal value: This investigation was performed to examine the effect of reduced – compared to the nominal injection pressure value, which satisfies the experimental values of cylinder pressure – injection pressure, which appears when for example the fuel injector or the high pressure fuel pump faults and as result the fuel is injected inside the cylinder with lower pressure compared to the one specified for the specific engine operation point. In this case the multi-zone combustion model was used to generate a theoretical cylinder pressure profile for the nominal value of fuel injection pressure i.e. 240 bars. This value of fuel injection pressure is considered during cylinder pressure calibration procedure in order the predicted cylinder pressure data to match experimental cylinder pressure data at 2500 rpm and at 80% of full engine load. The multi-zone combustion model was also used to generate cylinder pressure profiles for the cases of 216 bars, 192 bars and 168 bars fuel injection pressure, which correspond to 90%, 80% and 70% of the fuel injection pressure considered i.e. 240 bars to match experimental cylinder pressure data at 2500 rpm and at 80% of full engine load.
- Variation of total fuel injected quantity per engine cycle i.e. variation of engine fuel consumption: This investigation is performed to examine the effect of variable fuel consumption when for example the injector nozzle orifice has been blocked or the injector nozzle needle has been stacked and as result the fuel injector does not inject the proper fuel quantity per engine cycle. In this case also the multi-zone combustion model was used to generate theoretical cylinder pressure profile for the proper fuel injected quantity per engine cycle i.e. 1.1 kg/h (nominal value at 2500 rpm and at 80% of full load). This value of fuel consumption is not the experimental one, which corresponds exactly to engine operation at 2500 rpm and at 80% of full load but it is the theoretical fuel consumption which provides a

theoretical cylinder profile which matches with the experimental one at this operating case. Additional cylinder pressure profiles were generated using the multi-zone model for values of fuel consumption equal to 1.265 kg/h (115% of the nominal value), 0.99 kg/h (90% of the nominal value) and 0.88 kg/h (80% of the nominal value). The case of 1.265 kg/h is examined to simulate the case when the power of one engine cylinder is higher than the standard one due to excess fuel injected quantity per engine cycle.

- Reduction of compression ratio (CR) due to potentially excessive wear of piston compression rings: The wear of compression rings due to either erosive environment as a result of the fuel oil composition or due to excessive in-cylinder gas temperature results in reduction of the effective compression ratio and results in increased blow-by losses to engine crankcase. The multi-zone combustion model was used also in this case to predict cylinder pressure profile at 2500 rpm and at 80% of full load using a nominal value of CR equal to 17.1:1. This cylinder pressure profile was compared with the corresponding experimentally obtained cylinder pressure profile. Afterwards, the multi-zone combustion model was used to generate cylinder pressure profiles for the three different values of CR namely 16.67:1, 16.25:1 and 15.39:1, which correspond to 97.5%, 95% and 90% of the nominal CR value.

RESULTS AND DISCUSSION

Experimental Assessment of the Diesel Engine Closed-Cycle Simulation Model Predictive Ability

Before the implementation of the theoretical investigation for the examination of the effect of variable injection pressure, fuel consumption and compression ratio on the combustion and performance characteristics of the single-cylinder DI diesel engine “Lister LV1” the ability of the multi-zone combustion model to predict with enough accuracy the cylinder pressure profile should be assessed. For this reason, in Figure 3 is shown a comparison of predicted and experimental cylinder pressure data at 2500 rpm and at 80% of full load. The predicted cylinder pressure values have been generated using the multi-zone combustion model for mean injection pressure equal to 240 bar, fuel consumption equal to 1.1 kg/h, compression ratio equal to 17.1:1 and injection timing equal to 15 degrees before TDC. As evidenced from Figure 3, the multi-zone combustion model succeeds to predict with enough accuracy the measured cylinder pressure both during compression and during combustion and expansion stroke. Hence, it can be assumed with adequate confidence that the predictions for cylinder pressure of the multi-zone combustion model when the mean injection pressure or the fuel consumption or the compression ratio are varying are trustworthy.

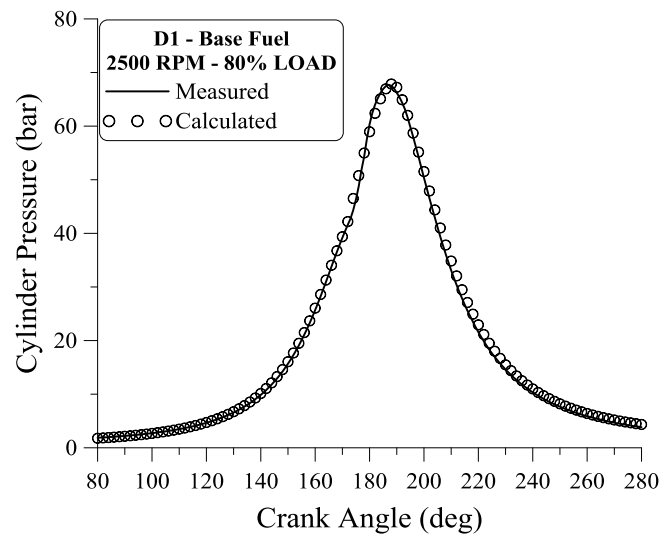


FIGURE 3. Comparison of theoretical and experimental values of cylinder pressure of “Lister LV1” engine at 2500 rpm and at 80% of full load

Effect of Mean Injection Pressure Variation on DI Diesel Engine Performance and Combustion Characteristics

In this paragraph is examined the effect of mean injection pressure variation on the performance parameters and the combustion characteristics of a four-stroke high-speed single-cylinder DI diesel engine “Lister LV1”. More specifically, it is examined the reduction of mean injection pressure compared to its nominal value at 2500 rpm and at 80% of full load for simulating the injection pressure loss when for example the fuel pump does not provide enough compression of the injected fuel. In such case fuel injector needle is lifted at the proper crank angle (i.e. proper injection timing) and the proper fuel quantity is injected at a specific engine speed and load, but fuel injection is not performed with the proper injection pressure due to fuel pump problems such as increased blow-by losses of the reciprocating fuel pump. Hence, it is examined the effect of variable mean injection pressure compared to its nominal value (this value corresponds to the mean injection pressure which provides a theoretical cylinder pressure profile that matches with the corresponding experimental one) to cylinder pressure profile, indicated power, ISFC, instantaneous and cumulative net heat release rate, instantaneous heat loss rate, ignition angle, ignition delay and combustion durations of 5%, 25%, 50% and 90% of total fuel injected quantity per engine cycle.

The values of mean injection pressure examined in the present study are:

- 240 bar – Nominal value of mean injection pressure, which provides a theoretical cylinder pressure profile using the multi-zone combustion model that matches the corresponding experimental cylinder pressure profile at 2500 rpm and at 80% load.
- 216 bar – This value of mean injection pressure corresponds to the 90% of the nominal value.
- 192 bar – This value of mean injection pressure corresponds to the 80% of the nominal value.
- 168 bar - This value of mean injection pressure corresponds to the 70% of the nominal value.

For each one of the above-mentioned mean injection pressures are derived theoretical cylinder pressure profiles using the multi-zone combustion model. It should be mentioned that the fuel injection process in the closed-cycle simulation model is modelled as a rectangular pulse of injection pressure. This means that for the time duration the injector needle is open the fuel injection pressure is constant and equal to its mean value, which is provided to the closed-cycle simulation model as input. Hence, initially a simulation was performed at 2500 rpm and at 80% of full load using mean injection pressure value equal to 240 bar, fuel consumption equal to 1.1 kg/h, compression ratio equal to 17.1:1 and injection timing equal to 15 degCA BTDC. At all other cases of mean injection pressure, the above-mentioned input values of fuel consumption, compression ratio and injection timing remained the same to isolate only the effect of mean injection pressure. Afterwards, the theoretical cylinder pressure profiles derived from the previous computational investigation were supplied to the MATLAB model for performing a heat release rate analysis and for predicting the main combustion parameters and engine performance characteristics at each injection pressure case.

In Figure 4(a) is shown the impact of mean injection pressure reduction on the predicted instantaneous fuel evaporation rate. Specifically, in Figure 4(a) are provided theoretical results for fuel evaporation rate for four values of mean injection pressure i.e. 240 bar, which corresponds to the nominal value of mean injection pressure at 2500 rpm and at 80% load, 216 bar, 192 bar and 168 bar. As witnessed from Figure 4(a), the reduction of mean injection pressure from 240 bar to 168 bar results in reduction of the peak values of fuel evaporation rate and results in elongation of the fuel evaporation process. Hence, the reduction of mean injection pressure results in direct reduction of the velocity of the fuel injected spray at the exit of the injector nozzle and thus, results in significant reduction of the vaporized fuel mass per crank angle degree step. The considerable reduction of fuel evaporation rate results in the significant increase of the fuel evaporation process duration since the total fuel injected quantity remains the same at all cases of fuel injection pressure.

In Figure 4(b) is shown the effect of mean injection pressure variation on the predicted cylinder pressure profiles. Specifically, in Figure 4(b) are given theoretical results for cylinder pressure for four values of mean injection pressure i.e. 240 bar, which corresponds to the nominal value of mean injection pressure at 2500 rpm and at 80% load, 216 bar, 192 bar and 168 bar. As evidenced from Figure 4(b), the reduction of mean injection pressure from 240 bar to 168 bar results in reduction of cylinder pressure around TDC and thus, in significant reduction of peak cylinder pressure. The reduction of mean injection pressure did not affect the cylinder pressure increase during compression stroke whereas, the impact of mean injection pressure reduction on cylinder pressure during expansion stroke is imperceptible. The reduction of cylinder pressure around TDC with decreasing mean injection pressure can be attributed to the reduction of fuel evaporation rate as evidenced in Figure 6(a), which results in reduction of fuel combustion rate during injection process curtailing thus, cylinder pressure around TDC.

The impact of mean injection pressure reduction on predicted in-cylinder bulk gas temperature is shown in Figure 4(c). More specifically, in Figure 4(c) are given theoretical results for bulk gas temperature for four values of mean injection pressure i.e. 240 bar, which corresponds to the nominal value of mean injection pressure at 2500 rpm and at 80% load, 216 bar, 192 bar and 168 bar. As evidenced from Figure 4(c), the reduction of mean injection pressure results in noticeable reduction of in-cylinder bulk gas temperature around TDC as a result of the corresponding reduction of in-cylinder pressure witnessed in Figure 4(b). The effect of mean injection pressure reduction on in-cylinder bulk gas temperature during expansion stroke is rather imperceptible.

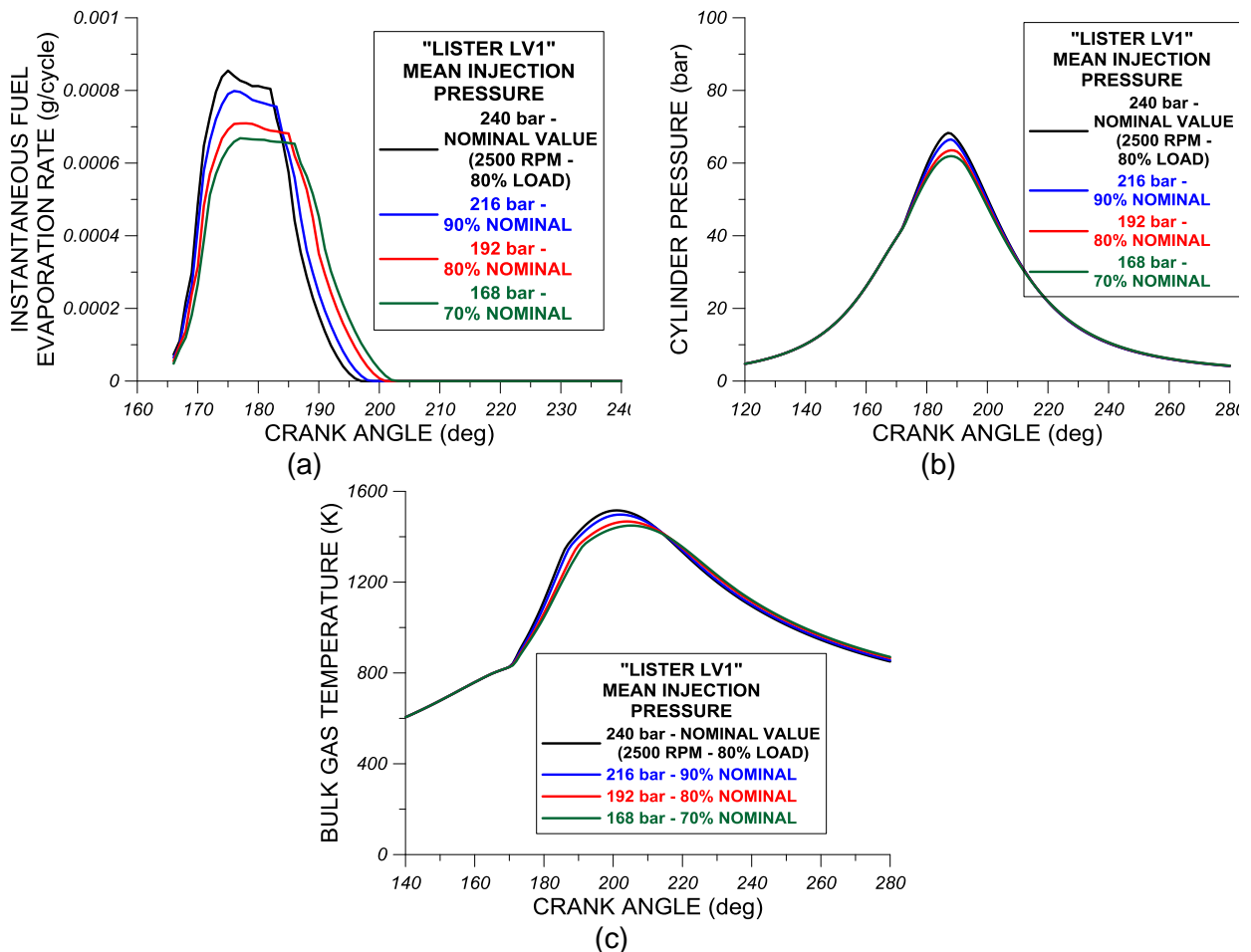


FIGURE 4. Effect of fuel mean injection pressure reduction on theoretical (a) instantaneous fuel evaporation rate, (b) cylinder pressure and (c) in-cylinder bulk gas temperature profiles of “Lister LV1” engine. Theoretical results are presented at 240 bars (nominal value of injection pressure), 216 bars (90% of nominal value of injection pressure), 192 bars (80% of nominal value of injection pressure) and 168 bars (70% of nominal value of injection pressure) of fuel injection pressure. The fueling rate of 1.1 kg/h, 240 bars fuel injection pressure and 17.1:1 compression ratio corresponds to “Lister LV1” engine operation at 2500 rpm and at 80% of full load.

Figure 5 depicts the effect of mean injection pressure variation on calculated instantaneous net heat release rate (Figure 5(a)), instantaneous heat losses rate (Figure 5(b)) and cumulative net heat release rate (Figure 5(c)). Specifically, in Figure 5(a) is shown instantaneous net heat release rate profiles for the following four values of mean injection pressure i.e. 240 bar, which corresponds to theoretical engine operation at 2500 rpm and at 80% load, 216 bar, 192 bar and 168 bar. As evidenced from Figure 5(a), the reduction of injection pressure results in the reduction of premixed combustion phase intensity leading thus, to lower peak premixed net heat release rates. On the other hand, the reduction of mean injection pressure promotes diffusion-controlled combustion phase. Hence, overall it can be stated that the reduction of mean injection pressure for the same fuel injected mass per engine cycle results in reduction of the fuel burned under premixed conditions and in parallel results in the increase of the fuel percentage burned

under diffusion-controlled conditions. This is attributed to the curtailment of fuel evaporation rate with decreasing mean injection pressure, which results in reduction of fuel percentage burned under premixed conditions and shifts the fuel combustion towards diffusion-controlled phase leading thus, to the deterioration of soot emissions primarily generated under diffusion-combustion conditions. From the observation of Figure 5(b), it can be stated that the reduction of mean injection pressure results in reduction of instantaneous heat losses rate during initial stages of expansion stroke and specifically from almost 180 degrees ABDC until 210 degrees ABDC as a main outcome of the corresponding reduction of bulk gas temperature evidenced in Figure 4(c). According to Figure 5(c), the reduction of mean injection pressure results in reduction of cumulative net heat release rate during expansion stroke and specifically, from 175 degrees ABDC until almost 220 degrees ABDC as a result mainly of the variations observed in instantaneous net heat release rate in Figure 5(a).

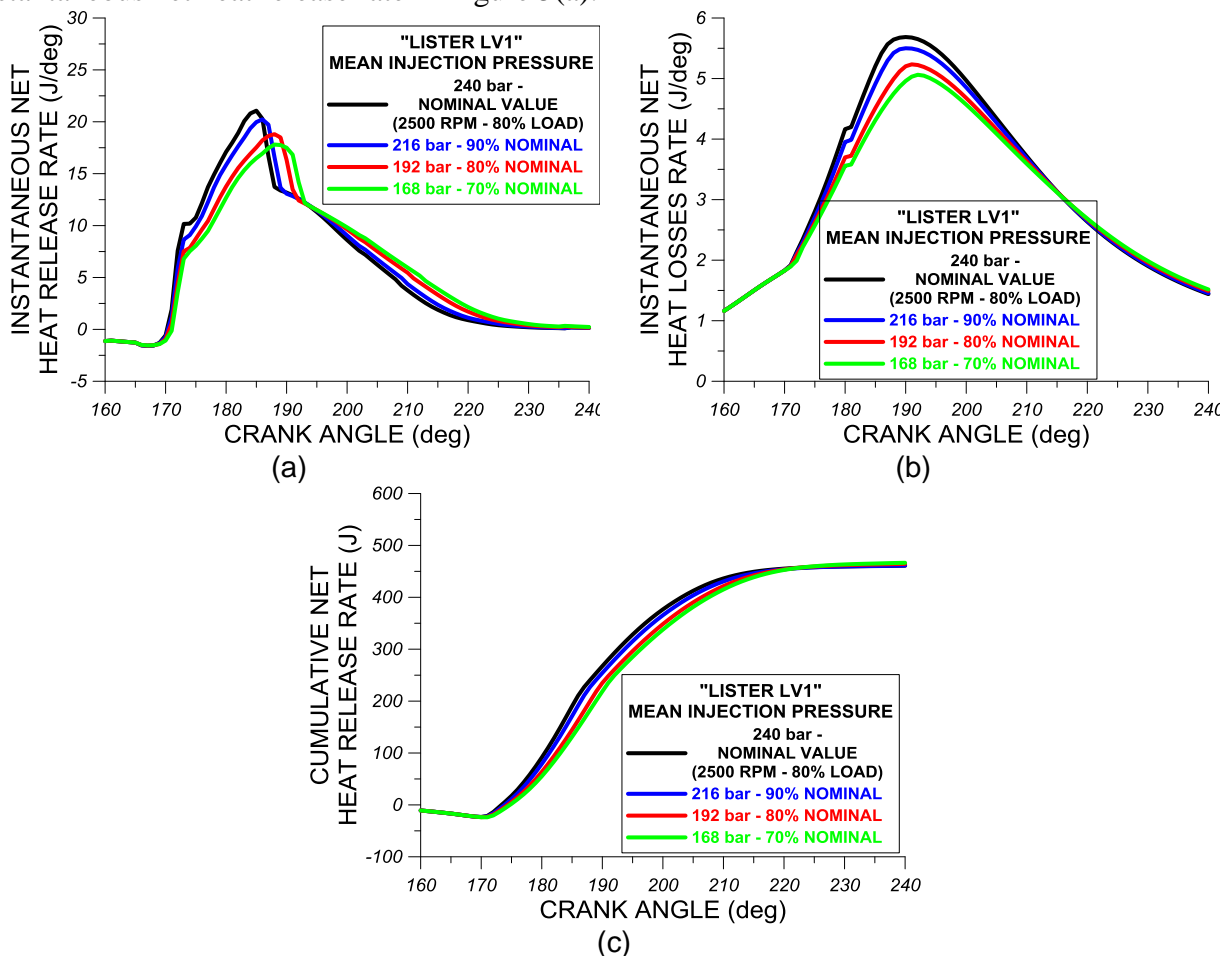


FIGURE 5. Effect of mean injection pressure variation on the predicted (a) instantaneous net heat release rate, (b) instantaneous heat loss rate and (c) cumulative net heat release rate of "Lister LV1" engine. Theoretical results are presented at 240 bars (nominal value of injection pressure), 216 bars (90% of nominal value of injection pressure), 192 bars (80% of nominal value of injection pressure) and 168 bars (70% of nominal value of injection pressure) of fuel injection pressure. The fueling rate of 1.1 kg/h, 240 bars fuel injection pressure and 17.1:1 compression ratio corresponds to "Lister LV1" engine operation at 2500 rpm and at 80% of full load.

Figure 6(a) depicts the effect of varying mean injection pressure on examined engine indicated power. Specifically, results for indicated power are given for four injection pressures namely, 240 bar, 216 bar, 192 bar and 168 bar. As evidenced from Figure 6(a), the reduction of mean injection pressure from 240 to 168 bar results in a very small reduction of indicated power since according to Figure 4(a) the reduction of mean injection pressure does not affect seriously the cylinder pressure during most of the expansion stroke and thus, the reduction of injection pressure has imperceptible influence on main expansion work. The small reduction of indicated power evidenced in Figure 6(a) results, for the same fuel injected mass per engine cycle, in small increase of ISFC. Hence, the reduction of mean injection pressure slightly deteriorates engine power and engine efficiency. According to Figure 6(c) and in relation with the facts observed in Figure 4(a), the reduction of mean injection pressure results in small reduction of peak cylinder pressure primarily due to reduction of cylinder pressure around TDC as a result of the curtailment of the fuel evaporation rate. The small reduction of peak cylinder pressure can be considered as beneficial for the long-term endurance of the examined engine since the reduction of peak cylinder pressure and temperature reduces the thermal and mechanical stress of the cylinder assembly.

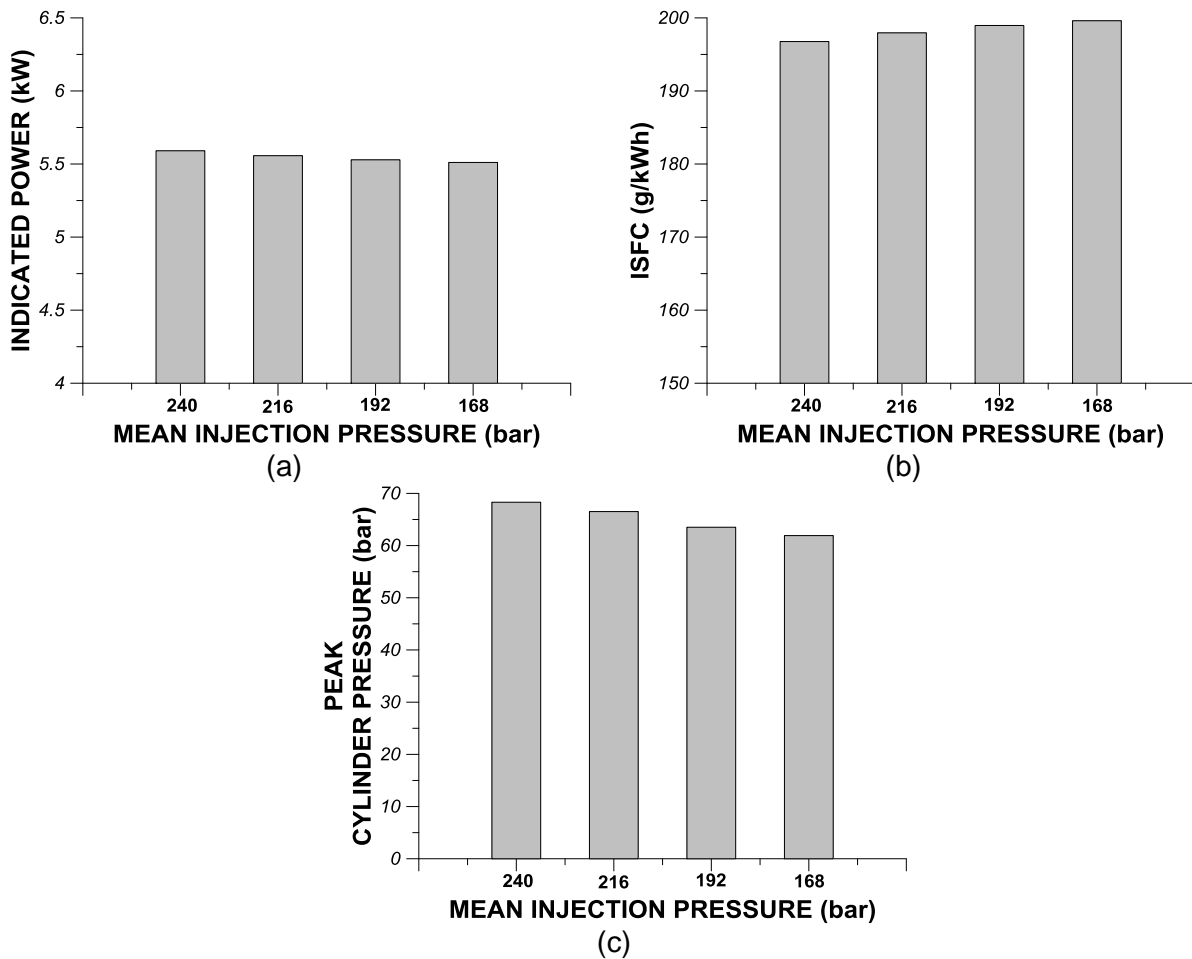


FIGURE 6. Effect of mean injection pressure variation on the predicted (a) indicated power, (b) Indicated Specific Fuel Consumption (ISFC) and (c) peak cylinder pressure of “Lister LV1” engine. Theoretical results are presented at 240 bars (nominal value of injection pressure), 216 bars (90% of nominal value of injection pressure), 192 bars (80% of nominal value of injection pressure) and 168 bars (70% of nominal value of injection pressure) of fuel injection pressure. The fueling rate of 1.1 kg/h, 240 bars fuel injection pressure and 17.1:1 compression ratio corresponds to “Lister LV1” engine operation at 2500 rpm and at 80% of full load.

In Figure 7(a) is shown the variation of ignition angle with mean injection pressure. As evidenced from Figure 7(a), the reduction of mean injection pressure from 240 bar to 168 bar results in a small reduction of ignition angle or in other words, the reduction of mean injection pressure delays the combustion initiation resulting thus, to its shift closer to the TDC. Combustion commencement delay with injection pressure reduction can be ascribed to the delay of combustion pressure rise due to reduction of fuel evaporation rate and subsequently, due to curtailment of premixed combustion rate. Having given that the fuel injection timing remained constant at 15 degrees BTDC for all cases of variable injection pressure, the previously-observed delay of combustion initiation with decreasing injection pressure results, as evidenced from Figure 7(b), in an increase of ignition delay, which reaches up to almost 15% compared to the conventional case of 240 bar mean injection pressure.

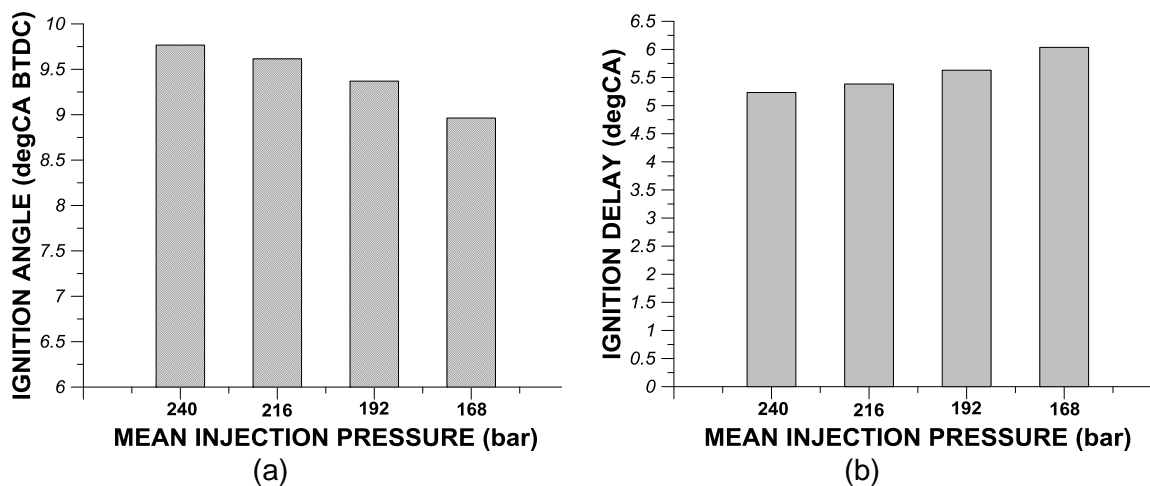


FIGURE 7. Effect of mean injection pressure variation on the predicted (a) ignition angle and (b) ignition delay. Theoretical results are presented at 240 bars (nominal value of injection pressure), 216 bars (90% of nominal value of injection pressure), 192 bars (80% of nominal value of injection pressure) and 168 bars (70% of nominal value of injection pressure) of fuel injection pressure. The fueling rate of 1.1 kg/h, 240 bars fuel injection pressure and 17.1:1 compression ratio corresponds to “Lister LV1” engine operation at 2500 rpm and at 80% of full load.

In Figures 8(a)-(d) is shown the effect of mean injection pressure variation on the combustion durations of 5% (Figure 8(a)), 25% (Figure 8(b)), 50% (Figure 8(c)) and 90% (Figure 8(d)) of total fuel injected mass per engine cycle. According to all Figures 8(a)-(d) the reduction of mean injection pressure from 240 bar to 168 bar results in an increase of all percentages of fuel combustion duration. In the case of combustion durations of 5% and 25% of total injected fuel (Figures 8(a)-(b)), which correspond to premixed combustion phase, their increase with decreasing mean injection pressure can be attributed to the reduction of premixed combustion intensity. Hence, the reduction of mean injection pressure leads to an increase of the premixed combustion duration of the same fuel injected mass per engine cycle i.e. same fuel quantity takes more time to be burned under premixed conditions. Also according to Figure 8(d), the reduction of mean injection pressure does not only increases premixed combustion durations but also increases – and this is more pronounced in the case of the lowest injection pressure i.e. 168 bar – the combustion duration of 90% fuel injected mass per engine cycle. Hence, the same fuel quantity delays to be burned not only under premixed conditions but also under both premixed and diffusion-controlled conditions and thus, overall it can be stated that the reduction of mean injection pressure affects negatively both premixed and diffusion-controlled combustion phase durations and consequently, deteriorates total combustion duration.

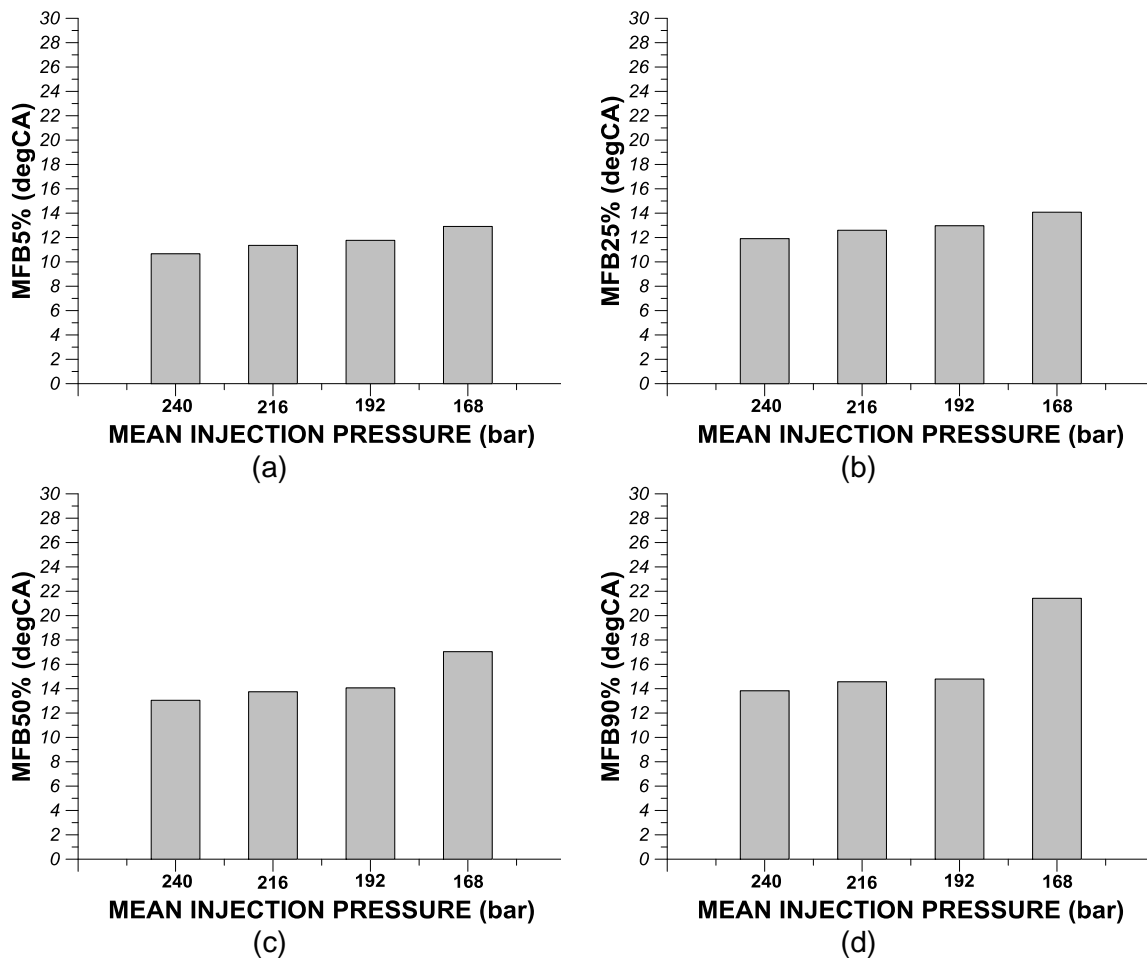


FIGURE 8. Effect of mean injection pressure variation on the predicted combustion duration in crank angle degrees of (a) 5%, (b) 25%, (c) 50% and (d) 90% of fuel injected mass per engine cycle. Theoretical results are presented at 240 bars (nominal value of injection pressure), 216 bars (90% of nominal value of injection pressure), 192 bars (80% of nominal value of injection pressure) and 168 bars (70% of nominal value of injection pressure) of fuel injection pressure. The fueling rate of 1.1 kg/h, 240 bars fuel injection pressure and 17.1:1 compression ratio corresponds to “Lister LV1” engine operation at 2500 rpm and at 80% of full load.

Effect of Fuel Consumption Variation on DI Diesel Engine Performance and Combustion Characteristics

The effect of fuel consumption variation on combustion parameters and performance characteristics of a four-stroke high-speed single-cylinder DI diesel engine (“Lister LV1”) is examined in this paragraph. The objective of this investigation is to simulate diesel engine operation in the case the fuel injector does not inject the proper fuel quantity at a specific engine operating condition either due to injector needle lift problem or due to fuel pump improper operation or due to nozzle orifices blocking. Hence, it is considered fuel consumption variation compared to its nominal value, which provides a theoretical cylinder pressure profile using the closed-cycle simulation model that matches the corresponding experimental one at 2500 rpm and

at 80% of full load. It is examined the impact of fuel consumption variation on predicted fuel evaporation rate, cylinder pressure profile, bulk gas temperature profile, indicated power, ISFC, net instantaneous and cumulative heat release rate, ignition angle, ignition delay and combustion durations of 5%, 25%, 50% and 90% of total fuel injected mass per engine cycle. The following fuel consumption values are examined:

- 1.1 kg/h, which corresponds to the nominal value of fuel consumption that provides a theoretical cylinder pressure profile using the multi-zone combustion model that matches the corresponding experimental cylinder pressure profile at 2500 rpm and at 80% load.
- 1.265 kg/h – This value of fuel consumption corresponds to the 115% of the nominal value.
- 0.99 kg/h– This value of fuel consumption corresponds to the 90% of the nominal value.
- 0.88 kg/h - This value of fuel consumption corresponds to the 80% of the nominal value.

For each one of the above-mentioned fuel consumption values are derived theoretical cylinder pressure profiles using the multi-zone combustion model. Initially a simulation was performed at 2500 rpm and at 80% of full load using fuel consumption value equal to 1.1 kg/h, mean injection pressure equal to 240 bar, compression ratio equal to 17.1:1 and injection timing equal to 15 degCA BTDC. At all other cases of fuel consumption, the above-mentioned input values of mean injection pressure, compression ratio and injection timing remained the same to isolate the effect of fuel consumption. Afterwards, the theoretical cylinder pressure profiles derived from the previous computational investigation were supplied to the MATLAB model for performing a heat release rate analysis and for predicting the main combustion parameters and engine performance characteristics at each fuel consumption case.

In Figure 9(a) is shown the effect of fuel consumption variation on predicted fuel evaporation rate using the multi-zone combustion model. Specifically, in Figure 9(a) are given predicted fuel evaporation rates for four fuel consumptions i.e. 1.1 kg/h, 1.265 kg/h, 0.99 kg/h and 0.88 kg/h. As evidenced from Figure 9, the reduction of fuel consumption results in reduction of the effective fuel evaporation period whereas, no significant changes are observed in the peak evaporation rate. In other words, the increase of fuel consumption, as expected, results in a time elongation of the fuel evaporation process shifting thus, combustion to the expansion stroke. Combustion shift to the expansion stroke is verified from Figure 9(b), which shows the effect of fuel consumption variation on the predicted cylinder pressure profile. As evidenced from Figure 9(b), the reduction of fuel consumption results in reduction of cylinder pressure during the entire expansion stroke and thus, in reduction of expansion work. According to Figure 9(c), the reduction of fuel injected mass per engine cycle results in significant reduction of in-cylinder bulk gas temperatures during expansion stroke i.e. after 190 degCA ABDC as a result of the reduction of the fuel evaporation rate. The reduction of bulk gas temperatures inside the combustion chamber during expansion stroke due to reduction of fuel consumption will lead to the significant reduction of exhaust gas temperature at EVO.

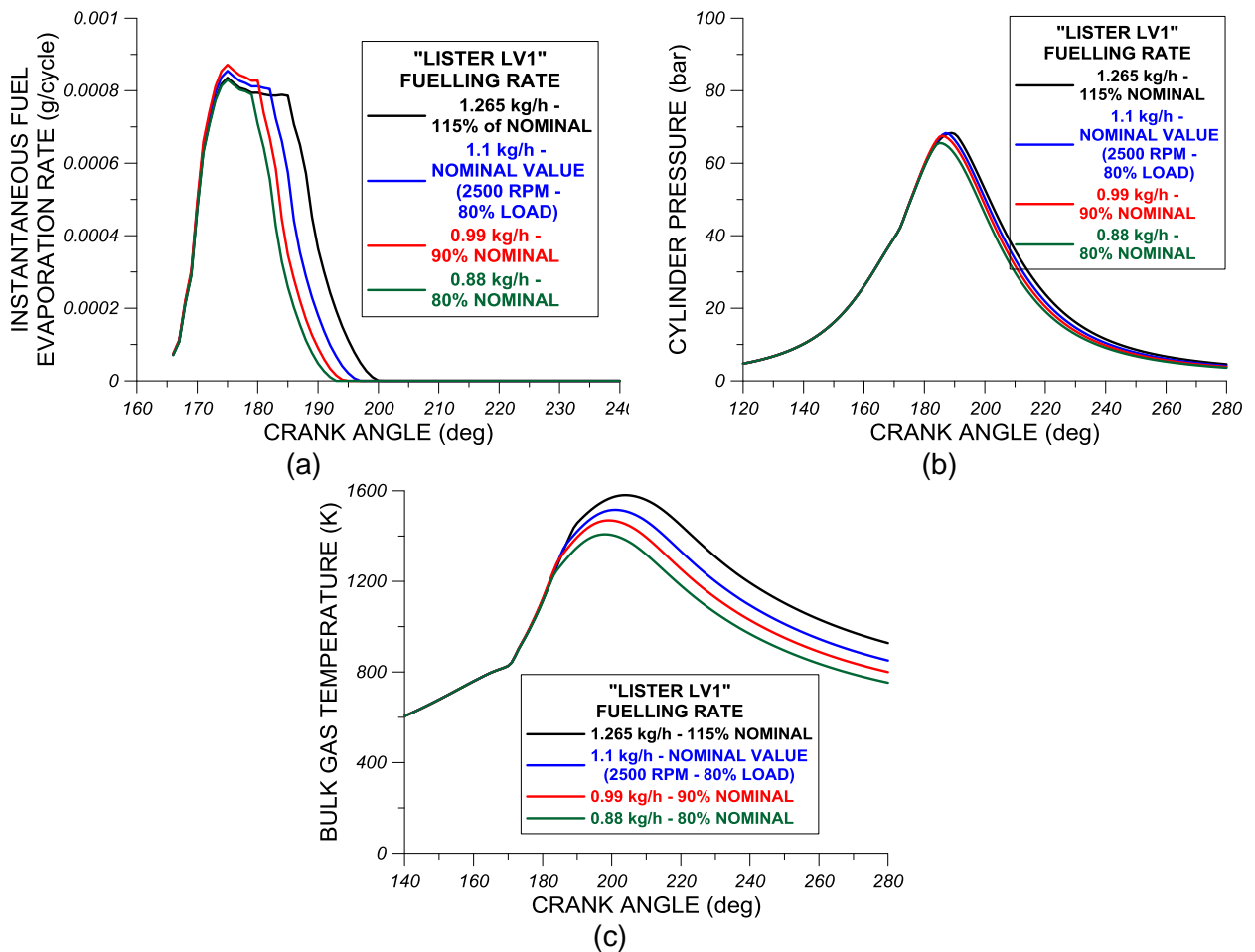


FIGURE 9. Effect of fuel consumption variation on theoretical (a) instantaneous fuel evaporation rate, (b) cylinder pressure and (c) in-cylinder bulk gas temperature profiles of “Lister LV1” engine. Theoretical results are presented at 1.1 kg/h (nominal value of fueling rate), 1.265 kg/h (115% of nominal fueling rate value), 0.99 kg/h (90% of nominal fueling rate value) and 0.88 kg/h (80% of nominal fueling rate value). The fueling rate of 1.1 kg/h, 240 bars fuel injection pressure and 17.1:1 compression ratio corresponds to “Lister LV1” engine operation at 2500 rpm and at 80% of full load.

As evidenced from Figure 10(a), which depicts the effect of fuel consumption variation on instantaneous net heat release rate, the reduction of cylinder pressure and bulk gas temperature during most of the expansion stroke due to the reduction of fuel consumption results in curtailment of combustion intensity during both premixed and diffusion-controlled combustion phases. The highest enhancement of combustion intensity is observed during diffusion-controlled combustion due to the shift of main combustion event to the late expansion stroke. This combustion shift to the late expansion stroke will also result to the considerable increase of in-cylinder generated and exhaust soot emissions. The reduction of fuel consumption and the subsequent reduction of bulk gas temperature results in considerable reduction of instantaneous heat losses rate during expansion stroke as evidenced from Figure 10(b). Finally, the shift of combustion event to the expansion stroke with increasing fuel consumption results in a substantial increase of the cumulative neat heat release rate and thus, to the total net combustion-released thermal energy as expected due to the increase of the supplied fuel heating power.

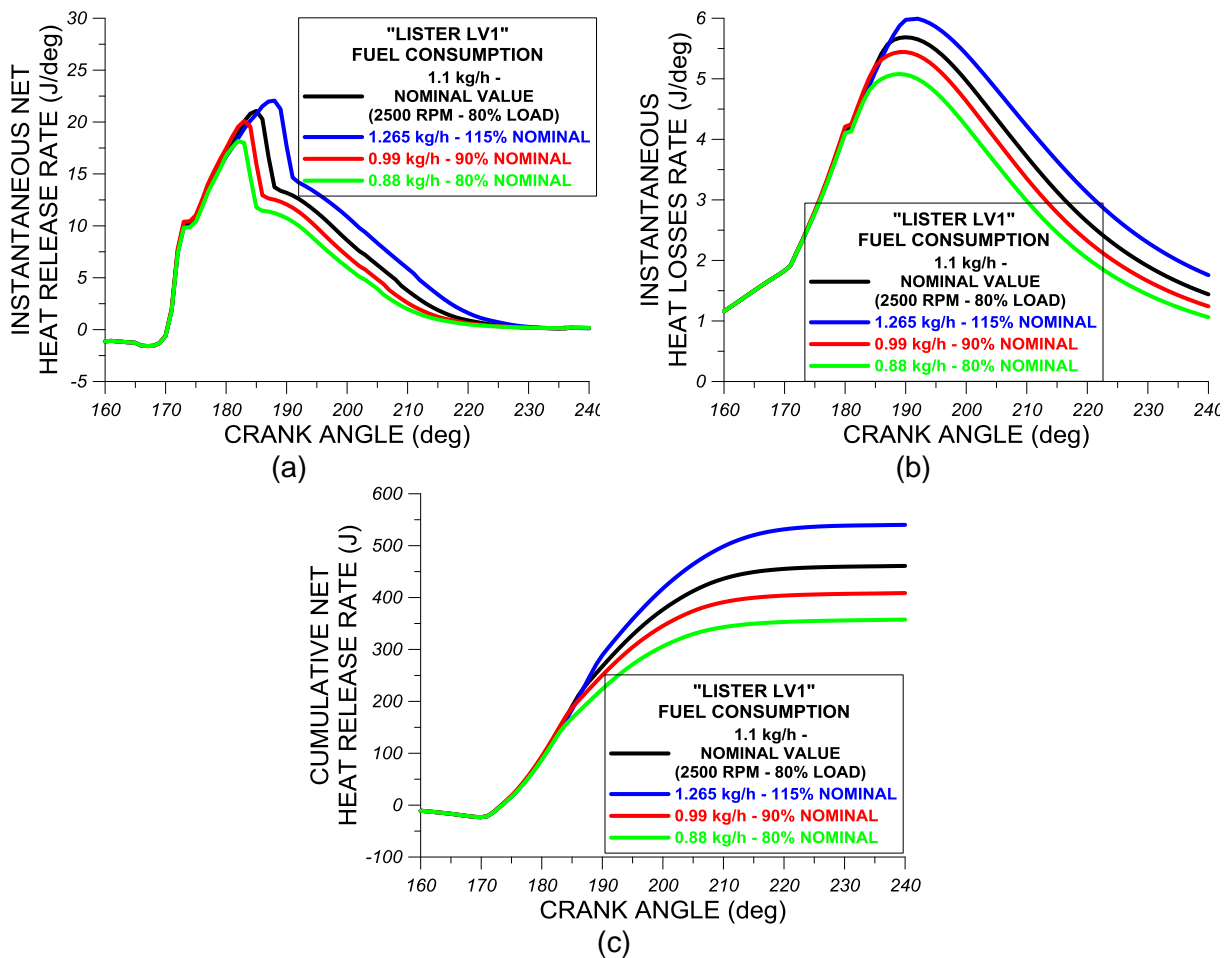


FIGURE 10. Effect of fuel consumption variation on the predicted (a) instantaneous net heat release rate, (b) instantaneous heat loss rate and (c) cumulative net heat release rate of “Lister LV1” engine. Theoretical results are presented at 1.1 kg/h (nominal value of fueling rate), 1.265 kg/h (115% of nominal fueling rate value), 0.99 kg/h (90% of nominal fueling rate value) and 0.88 kg/h (80% of nominal fueling rate value). The fueling rate of 1.1 kg/h, 240 bars fuel injection pressure and 17.1:1 compression ratio corresponds to “Lister LV1” engine operation at 2500 rpm and at 80% of full load.

In Figure 11(a) is shown the effect of varying fuel consumption on the indicated power. As observed from Figure 11(a), the increase of fuel consumption from 1.1 kg/h to 1.265 kg/h results in significant increase of indicated power due to previously-mentioned enhancement of the expansion work. The relative increase of indicated power in this case is 15%. On the other hand, the reduction of fuel consumption from 1.265 kg/h to 0.88 kg/h results in substantial reduction of engine power. The relative reduction of engine indicated power between 1.1 kg/h (i.e. nominal value of fuel consumption) and 0.88 kg/h is 21%. Hence, is proved that the reduction of fuel consumption results in an almost linear reduction of engine power as expected. As evidence from Figure 11(b), the linear reduction of engine power with decreasing fuel consumption results in imperceptible increase of ISFC (i.e. engine efficiency), which reaches up to 1.4% in the case of 0.88 kg/h compared to the nominal case of 1.1 kg/h. According to Figure 11(c), the reduction of fuel consumption results in a small reduction of peak cylinder pressure since the impact of fuel

consumption reduction is less pronounced during premixed combustion phase (i.e. variations in fuel consumption are more evident during diffusion-controlled combustion).

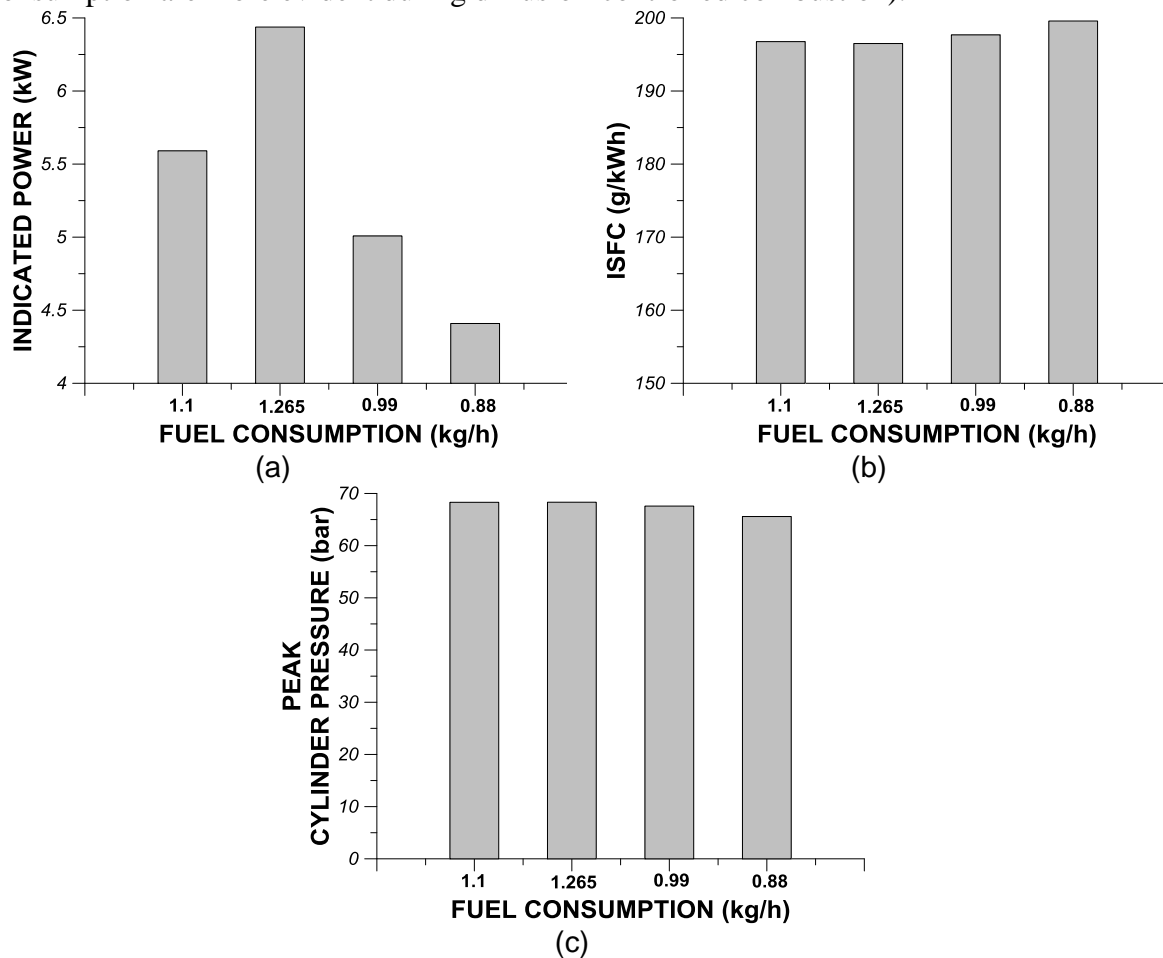


FIGURE 11. Effect of fuel consumption variation on the predicted (a) indicated power, (b) Indicated Specific Fuel Consumption (ISFC) and (c) peak cylinder pressure of “Lister LV1” engine. Theoretical results are presented at 1.1 kg/h (nominal value of fueling rate), 1.265 kg/h (115% of nominal fueling rate value), 0.99 kg/h (90% of nominal fueling rate value) and 0.88 kg/h (80% of nominal fueling rate value). The fueling rate of 1.1 kg/h, 240 bars fuel injection pressure and 17.1:1 compression ratio corresponds to “Lister LV1” engine operation at 2500 rpm and at 80% of full load.

Figure 12(a) shows the effect of fuel consumption variation on ignition angle. As evidenced from Figure 12(a), the reduction of fuel consumption does not bring any noticeable change to the ignition point since the fuel consumption does not affect the physical and chemical preparation pre-combustion mechanism. Consequently, since the injection timing was kept constant at all cases of fuel consumption variation, the invariance of ignition angle with varying fuel consumption results also in imperceptible changes to the ignition delay as evidenced from Figure 12(b).

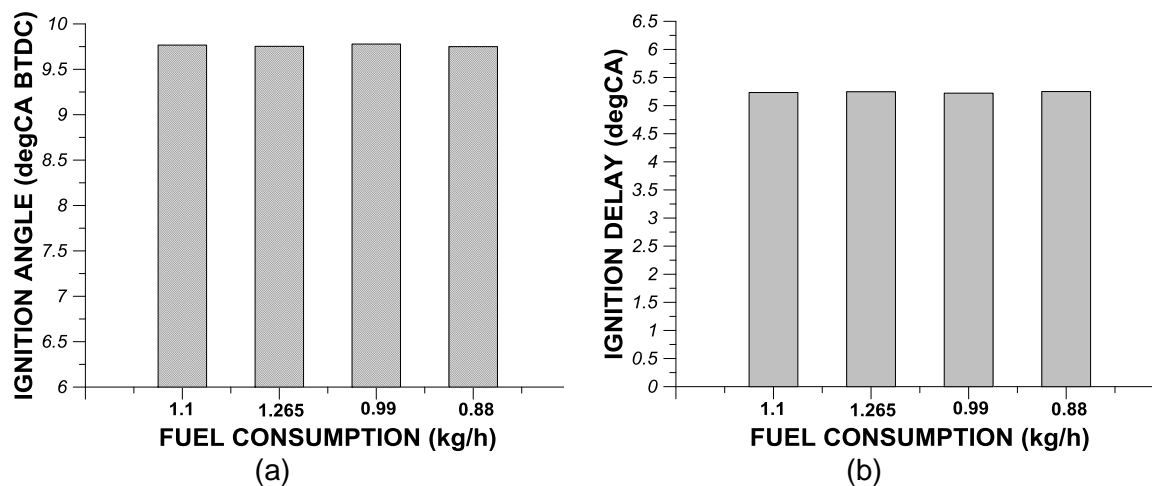


FIGURE 12. Effect of fuel consumption variation on the predicted (a) ignition angle and (b) ignition delay. Theoretical results are presented at 1.1 kg/h (nominal value of fueling rate), 1.265 kg/h (115% of nominal fueling rate value), 0.99 kg/h (90% of nominal fueling rate value) and 0.88 kg/h (80% of nominal fueling rate value). The fueling rate of 1.1 kg/h, 240 bars fuel injection pressure and 17.1:1 compression ratio corresponds to “Lister LV1” engine operation at 2500 rpm and at 80% of full load.

In Figures 13(a)-(d) is shown the effect of fuel consumption variation on the combustion durations of 5% (Figure 13(a)), 25% (Figure 13(b)), 50% (Figure 13(c)) and 90% (Figure 13(d)) of total fuel injected mass per engine cycle. According to Figures 13(a)-(b) the variation of fuel consumption does not bring serious changes to the combustion durations of 5% and 25% of total fuel injected mass per engine cycle. This can be attributed to the fact that the reduction of fuel consumption primarily affects the second diffusion-controlled stage of combustion and not the initial premixed phase of combustion. Hence, the combustion durations of 5% and 25% of total fuel injected mass do not vary noticeably with fuel consumption variation. The considerable reduction of diffusion-controlled combustion intensity with decreasing fuel consumption results in a slight increase of combustion durations of 50% and 90% of fuel injected mass per engine cycle as evidenced from Figures 13(c)-(d). The curtailment of diffusion-controlled combustion intensity with decreasing fuel consumption especially in the cases of 0.99 kg/h and 0.88 kg/h means that it takes more time for the same fuel quantity to be burned under diffusion-controlled conditions and this results in a slight elongation of the combustion durations of 50% and 90% of total fuel injected mass per engine cycle.

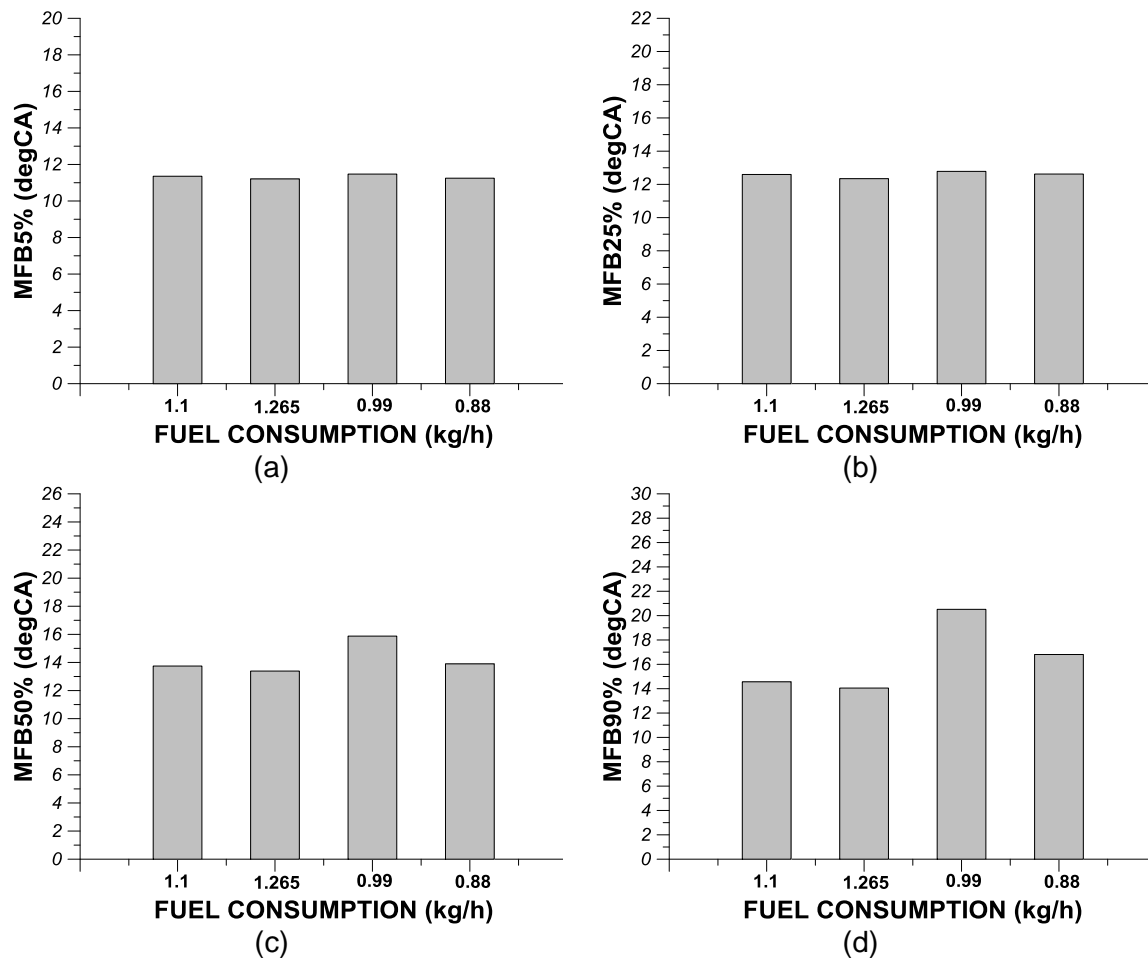


FIGURE 13. Effect of fuel consumption variation on the predicted combustion duration in crank angle degrees of (a) 5%, (b) 25%, (c) 50% and (d) 90% of fuel injected mass per engine cycle. Theoretical results are presented at 1.1 kg/h (nominal value of fueling rate), 1.265 kg/h (115% of nominal fueling rate value), 0.99 kg/h (90% of nominal fueling rate value) and 0.88 kg/h (80% of nominal fueling rate value). The fueling rate of 1.1 kg/h, 240 bars fuel injection pressure and 17.1:1 compression ratio corresponds to “Lister LV1” engine operation at 2500 rpm and at 80% of full load.

Effect of Compression Ratio Variation on DI Diesel Engine Performance and Combustion Characteristics

In this section is examined the impact of compression ratio on engine combustion and performance characteristics of a four-stroke high-speed single-cylinder DI diesel engine (“Lister LV1”). The objective of this investigation is to simulate diesel engine operation in the case of compression loss due to excessive wear of the piston assembly, which is a serious engine fault with direct negative repercussions on engine reliability and availability. Hence, to examine the impact of compression loss on engine combustion mechanism and performance parameters, it was considered four different values of compression ratio i.e. 17.1:1, 16.67:1, 16.25:1 and 15.39:1. The value of 17.1:1 compression ratio in conjunction with 240 bar injection pressure and 1.1 kg/h fuel consumption used as input values to the multi-zone model generate a theoretical cylinder pressure profile that as evidenced in previous section matches the experimental cylinder

pressure profile at 2500 rpm and at 80% load. The other three cases of compression ratio namely 16.67:1, 16.25:1 and 15.39:1 correspond to 97.5%, 95% and 90% of the nominal value of compression ratio (i.e. 17.1:1). Under this investigation, it is examined the impact of compression ratio variation on predicted fuel evaporation rate, cylinder pressure profile, bulk gas temperature profile, indicated power, engine efficiency (i.e. ISFC), instantaneous and cumulative net heat release rate, instantaneous heat losses rate, ignition point and ignition delay and combustion durations of 5%, 25%, 50% and 90% of total fuel injected mass per engine cycle.

Initially a simulation was performed at 2500 rpm and at 80% of full load using fuel consumption value equal to 1.1 kg/h, mean injection pressure equal to 240 bar, compression ratio equal to 17.1:1 and injection timing equal to 15 degCA BTDC. At all other cases of compression ratio, the above-mentioned input values of mean injection pressure, compression ratio and injection timing remained the same to isolate the effect of compression ratio. Afterwards, the theoretical cylinder pressure profiles derived from the previous computational investigation were supplied to the MATLAB model for performing a heat release rate analysis and for predicting the main combustion parameters and engine performance characteristics at each compression ratio case.

In Figure 14(a) is shown the effect of decreasing compression ratio on predicted fuel evaporation rates from the multi-zone combustion model. As observed from Figure 14(a), the reduction of compression ratio does not bring any serious effect on either peak fuel evaporation rates both the duration of fuel evaporation process. On the other hand, the reduction of compression ratio results in reduction of cylinder pressure both during compression stroke and around TDC as evidenced from Figure 14(b). Reduction of cylinder pressure initially during compression stroke and then during the initial stages of combustion can be ascribed to the reduction of peak compression pressure and temperature due to reduction of compression ratio. The variation of cylinder pressure with decreasing compression ratio is reflected on the variation of bulk gas temperature with varying compression ratio. Specifically, according to Figure 14(c), the reduction of compression ratio results in slight reduction of bulk gas temperature during compression stroke and during the initial stages of combustion.

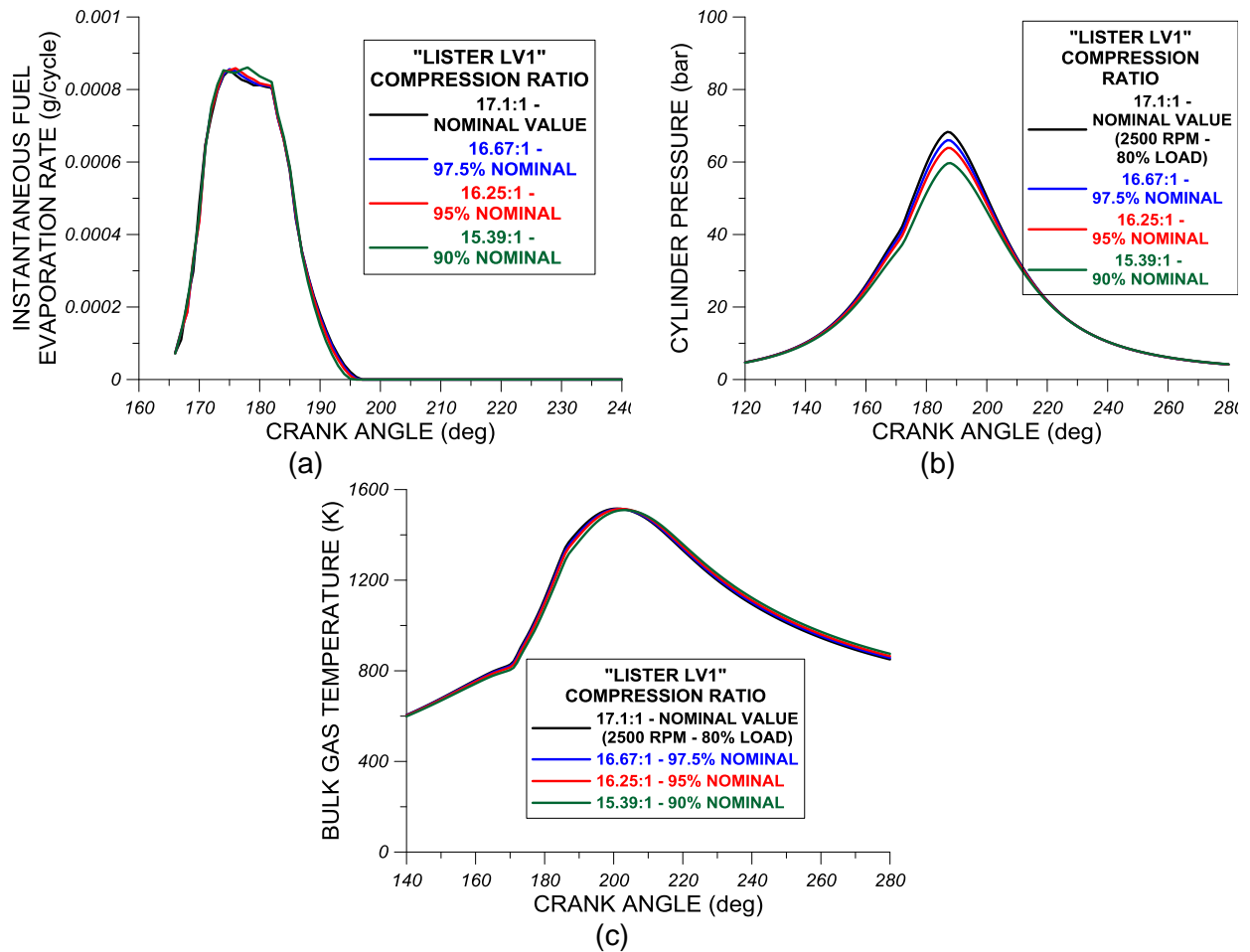


FIGURE 14. Effect of compression ratio variation on theoretical (a) instantaneous fuel evaporation rate, (b) cylinder pressure and (c) in-cylinder bulk gas temperature profiles of “Lister LV1” engine. Theoretical results are presented at 17.1:1 compression ratio (nominal value), 16.67:1 compression ratio (97.5% of nominal value), 16.25:1 compression ratio (95% of nominal value) and 15.39:1 (90% of nominal value). The fueling rate of 1.1 kg/h, 240 bars fuel injection pressure and 17.1:1 compression ratio corresponds to “Lister LV1” engine operation at 2500 rpm and at 80% of full load.

In Figure 15(a) is shown the effect of decreasing compression ratio on the instantaneous net heat release rate. As evidenced from Figure 15(a), the reduction of compression ratio results in a slight reduction of premixed combustion intensity whereas, a slight enhancement of diffusion-controlled combustion intensity is observed with decreasing compression ratio. This means that the reduction of compression ratio results in reduction of total fuel injected mass percentage burned under premixed conditions and in a subsequent slight increase of fuel injected mass portion burned under diffusion-controlled conditions. The reduction of cylinder pressure and most importantly, bulk gas temperature during compression stroke and during the initial stages of combustion results in considerable reduction of instantaneous heat losses rate as observed from Figure 15(b). The reduction of peak compression pressure and temperature due to reduction of compression ratio results in reduction of bulk gas temperature during compression stroke and during the initial stages of combustion affecting thus directly both convection and radiation heat

losses mechanisms. The variations of instantaneous net heat release rate observed with the reduction of compression ratio are reflected to the variation of cumulative net heat release rate. Specifically, as evidenced from Figure 15(c), the reduction of compression ratio results in reduction of cumulative net heat release rate during both stages of diesel combustion mechanism.

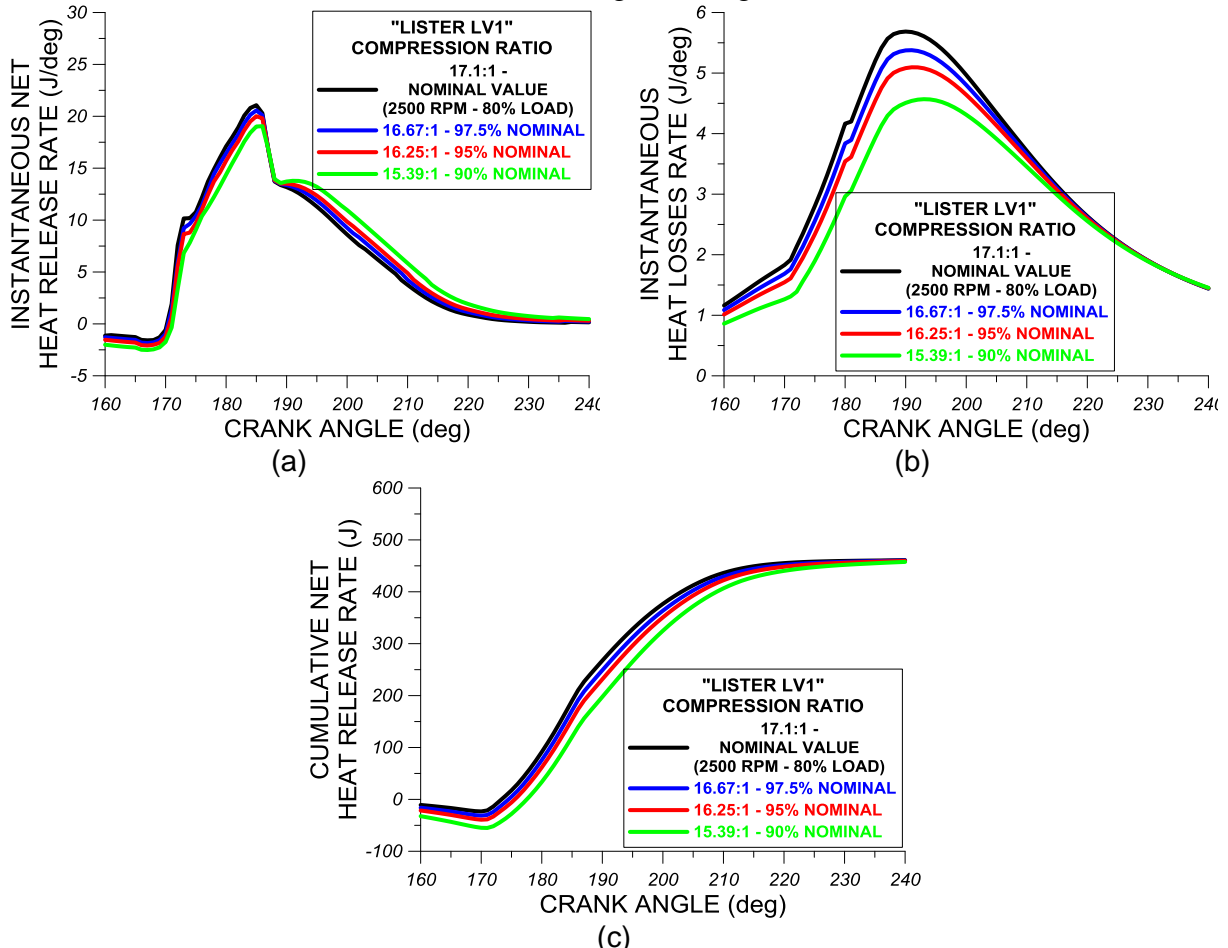


FIGURE 15. Effect of compression ratio variation on the predicted (a) instantaneous net heat release rate, (b) instantaneous heat loss rate and (c) cumulative net heat release rate of “Lister LV1” engine. Theoretical results are presented at 17.1:1 compression ratio (nominal value), 16.67:1 compression ratio (97.5% of nominal value), 16.25:1 compression ratio (95% of nominal value) and 15.39:1 (90% of nominal value). The fueling rate of 1.1 kg/h, 240 bars fuel injection pressure and 17.1:1 compression ratio corresponds to “Lister LV1” engine operation at 2500 rpm and at 80% of full load.

Figure 16(a) shows the effect of compression ratio on engine indicated power. As observed from Figure 16(a), the reduction of compression ratio results in slight decrease of engine indicated power mainly due to the reduction of cylinder pressure during expansion stroke, which potentially overwhelms the slight reduction of compression work during compression stroke. According to figure 16(b), the reduction of compression ratio results in a slight increase of ISFC (i.e. slight deterioration of indicated engine efficiency). The relative deterioration of ISFC between the nominal value of compression ratio (i.e. 17.1:1) and the reduced value of 15.39:1 is 1.5%. The slight reduction of ISFC with decreasing compression ratio is attributed to the slight reduction of indicated power for the same fuel consumption as previously observed. Finally, in

Figure 16(c) is shown the effect of compression ratio on peak cylinder pressure. As evidenced from Figure 16(c), the reduction of compression ratio results in reduction of peak cylinder pressure due to reduction of cylinder pressure profile around TDC as witnessed in Figure 14(b). The relative reduction of peak cylinder pressure caused by the reduction of compression ratio from 17.1:1 to 15.39:1 is 12.6%.

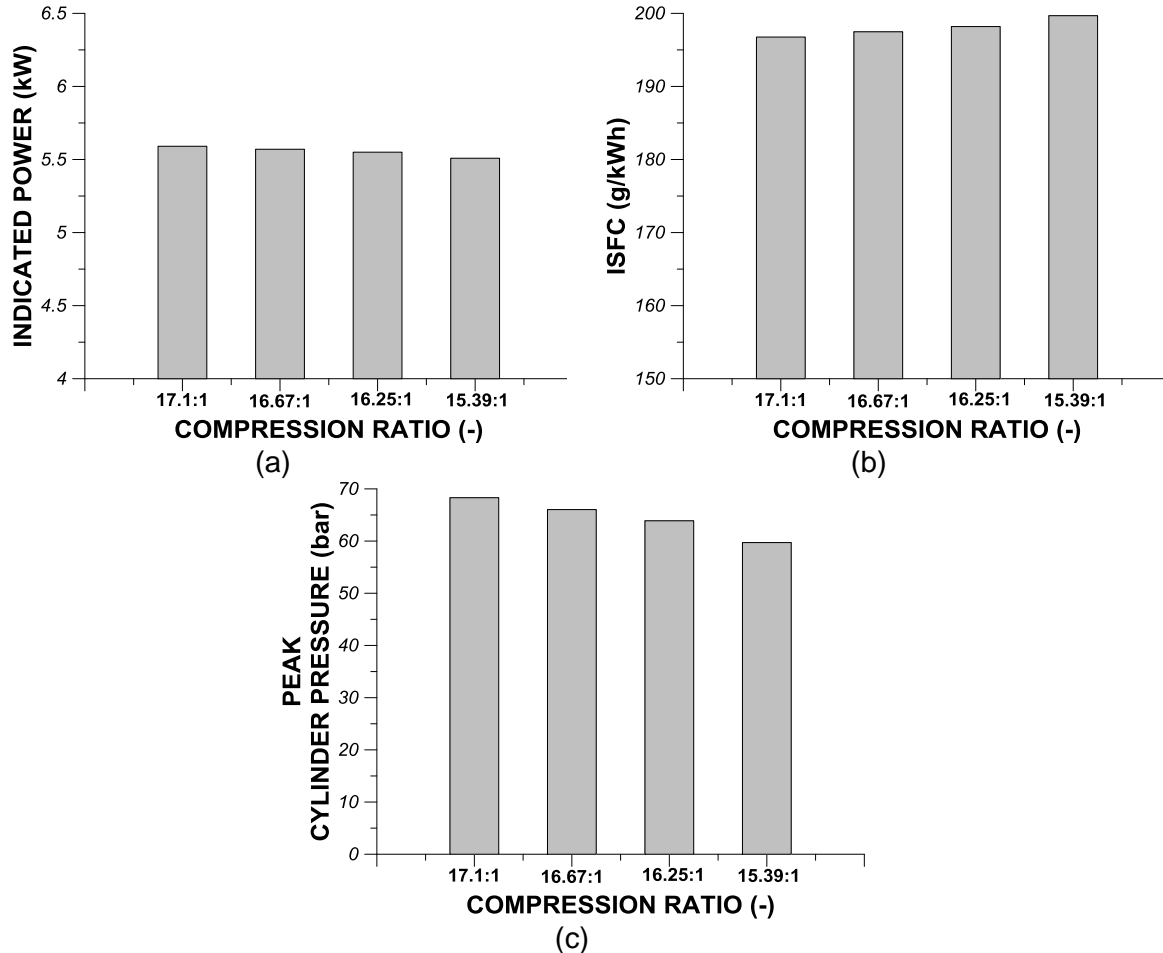


FIGURE 16. Effect of compression ratio variation on the predicted (a) indicated power, (b) Indicated Specific Fuel Consumption (ISFC) and (c) peak cylinder pressure of “Lister LV1” engine. Theoretical results are presented at 17.1:1 compression ratio (nominal value), 16.67:1 compression ratio (97.5% of nominal value), 16.25:1 compression ratio (95% of nominal value) and 15.39:1 (90% of nominal value). The fueling rate of 1.1 kg/h, 240 bars fuel injection pressure and 17.1:1 compression ratio corresponds to “Lister LV1” engine operation at 2500 rpm and at 80% of full load.

Figures 17(a) and 17(b) depict the impact of decreasing compression ratio on ignition angle and ignition delay respectively. As observed from Figure 17(a), the reduction of compression ratio results in reduction of ignition angle or in other words, the reduction of compression of compression ratio shifts combustion initiation closer to TDC. The delay of combustion commencement with decreasing compression ratio can be attributed to the reduction of cylinder pressure and temperature during fuel injection process. This means that fuel physical and chemical preparation processes are less promoted due to lower in-cylinder pressures and temperatures leading thus, to delayed combustion initiation. The delay of combustion

commencement (i.e. reduction of ignition angle) in conjunction with the constant injection timing (i.e. 15 degCA BTDC) at all cases of compression ratio results in an increase of ignition delay as evidenced from Figure 17(b). The relative deterioration of ignition delay with decreasing compression ratio reaches up to 16.4% when comparing the cases of nominal compression ratio (i.e. 17.1:1) and the reduced compression ratio of 15.39:1.

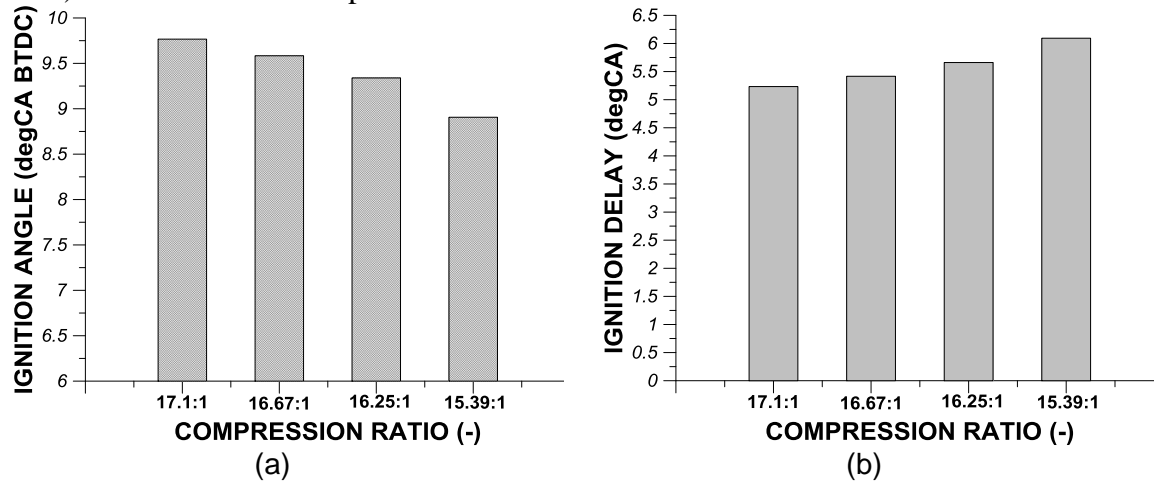


FIGURE 17. Effect of compression ratio variation on the predicted (a) ignition angle and (b) ignition delay. Theoretical results are presented at 17.1:1 compression ratio (nominal value), 16.67:1 compression ratio (97.5% of nominal value), 16.25:1 compression ratio (95% of nominal value) and 15.39:1 (90% of nominal value). The fueling rate of 1.1 kg/h, 240 bars fuel injection pressure and 17.1:1 compression ratio corresponds to “Lister LV1” engine operation at 2500 rpm and at 80% of full load.

Figures 18(a)-(d) illustrate the effect of compression ratio variation on the combustion durations of 5% (Figure 18(a)), 25% (Figure 18(b)), 50% (Figure 18(c)) and 90% (Figure 18(d)) of total fuel injected mass per engine cycle. According to Figures 18(a)-(b) the reduction of compression ratio results in the increase of combustion durations of 5% and 25% of total fuel injected mass per engine cycle. This means that the reduction of compression ratio, which affected negatively the intensity of premixed combustion, results in the elongation of the crank angle duration required for the same fuel injected quantity to be burned under premixed conditions. As evidenced also from Figures 18(c) and mainly from Figure 18(d), the reduction of compression ratio results in the increase of the combustion durations of 50% and 90% of total fuel injected mass per engine cycle. Hence, not only the premixed combustion phase is prolonged but also the highest portion of combustion duration (i.e. 90%) is prolonged with decreasing compression ratio underlying that both diesel combustion phases (i.e. premixed and diffusion-controlled) are prolonged with decreasing compression ratio. In other words, it takes more time in crank angle degrees for the same fuel injected mass to be burned under both premixed and diffusion-controlled conditions.

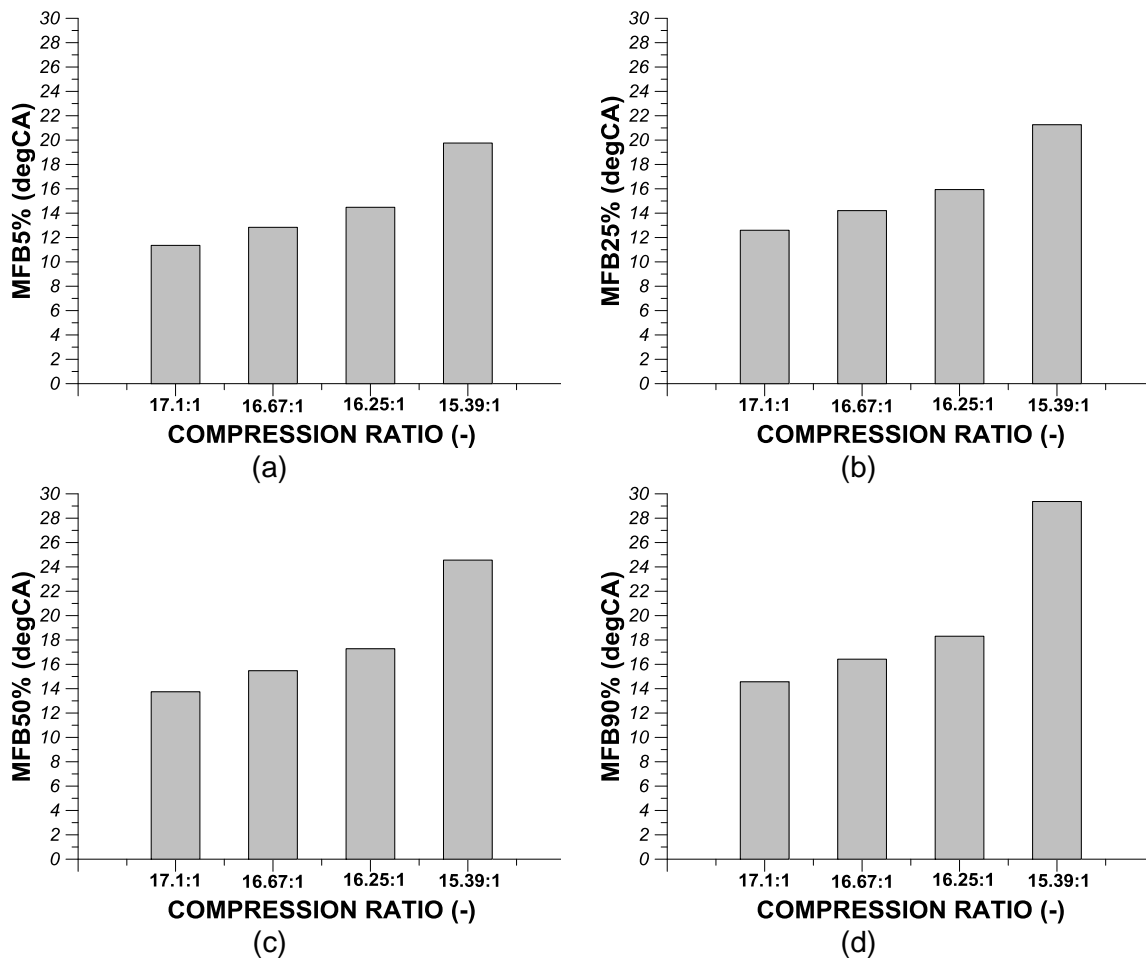


FIGURE 18. Effect of compression ratio variation on the predicted combustion duration in crank angle degrees of (a) 5%, (b) 25%, (c) 50% and (d) 90% of fuel injected mass per engine cycle. Theoretical results are presented at 17.1:1 compression ratio (nominal value), 16.67:1 compression ratio (97.5% of nominal value), 16.25:1 compression ratio (95% of nominal value) and 15.39:1 (90% of nominal value). The fueling rate of 1.1 kg/h, 240 bars fuel injection pressure and 17.1:1 compression ratio corresponds to “Lister LV1” engine operation at 2500 rpm and at 80% of full load.

CONCLUSIONS

In the present study a multi-zone combustion model was used to simulate the close-cycled operation of naturally aspirated single-cylinder DI diesel engine (“Lister LV1”) under various values of mean injection pressure, fuel consumption and compression ratio. The main objective of this investigation was to simulate diesel engine operation in the case of faulty operation of the fuel injection system simulated by reduced mean injection pressure and reduced fuel injected mass per engine cycle compared to the corresponding nominal values at a certain engine operating point (i.e. 2500 rpm and 80% load). Also, another objective of this examination was to simulate diesel engine operation in the case of degraded compression quality, which was modelled as compression ratio reduction compared to the corresponding nominal value at 2500 rpm and at 80% load. The multi-zone combustion model after experimental verification was used to derive theoretical results for fuel evaporation rate, cylinder pressure and bulk gas temperature

for each examined case of mean injection pressure, fuel consumption and compression ratio. Afterwards, the predicted cylinder pressure profiles were supplied to a computational model developed in MATLAB under a diploma thesis for performing a heat release rate analysis and for deriving corresponding engine combustion characteristics and performance parameters for all cases of diesel engine faulty operation examined. The assessment of the theoretical results for combustion parameters and performance characteristics at all diesel engine faulty operation cases examined lead to the derivation of the following conclusions:

The reduction of mean injection pressure resulted in:

- Reduction of fuel evaporation rate and elongation of fuel evaporation process.
- Decrease of cylinder pressure around TDC and subsequent reduction of peak cylinder pressure.
- Reduction of bulk gas temperature around TDC.
- Curtailment of premixed combustion intensity and enhancement of diffusion-controlled combustion intensity.
- Reduction of instantaneous heat losses rate due to reduction of bulk gas temperature.
- Slight reduction of engine indicated power and small deterioration of indicated engine efficiency (i.e. ISFC).
- Increase of ignition delay due to shift of combustion initiation closer to TDC.
- Increase of durations of both premixed and diffusion-controlled combustion phases.

The reduction of fuel consumption resulted in:

- Reduction of fuel evaporation process duration.
- Curtailment of cylinder pressure during expansion stroke with direct negative effects on the expansion work and subsequent small decrease of peak cylinder pressure.
- Reduction of bulk gas temperature during expansion stroke.
- Significant reduction of diffusion combustion intensity.
- Reduction of heat losses during expansion stroke.
- Significant reduction of indicated power and small increase of ISFC.
- No serious effect on ignition angle and ignition delay.
- Small increase of 90% combustion duration due to reduction of diffusion-controlled combustion intensity.

The reduction of fuel consumption resulted in:

- Reduction of fuel evaporation process duration.
- Curtailment of cylinder pressure during expansion stroke with direct negative effects on the expansion work and subsequent small decrease of peak cylinder pressure.
- Reduction of bulk gas temperature during expansion stroke.
- Significant reduction of diffusion combustion intensity.
- Reduction of heat losses during expansion stroke.
- Significant reduction of indicated power and small increase of ISFC.
- No serious effect on ignition angle and ignition delay.
- Small increase of 90% combustion duration due to reduction of diffusion-controlled combustion intensity.

The reduction of compression ratio resulted in:

- No serious effect on fuel evaporation rate.
- Reduction of cylinder pressure during late compression stroke and around TDC, which resulted in small decrease of peak cylinder pressure.

- Small reduction of bulk gas temperature around TDC.
- Small decrease of premixed combustion intensity and small enhancement of diffusion-controlled combustion intensity.
- Reduction of heat losses rate during compression stroke and around TDC.
- Small reduction of engine indicated power and small deterioration of engine ISFC.
- Reduction of ignition angle with respect to TDC and increase of ignition delay.
- Increase of both premixed and total combustion durations.

Overall, it can be stated that the reduction of mean injection pressure and compression ratio affects directly the combustion mechanism since they resulted in an increase of ignition delay and thus, to a shift of combustion to the expansion stroke with direct negative effects of exhaust gas temperature at EVO and on particulate emissions formed during diffusion-controlled combustion. The reduction of mean injection pressure and compression ratio also affected negatively both the duration of premixed combustion phase and the total combustion duration. On the other hand, the reduction of fuel consumption due to reduction of the engine supplied heating power has a direct negative effect on engine power and engine efficiency whereas, did not affect seriously the main combustion characteristics such as ignition angle, ignition delay and combustion duration. All faulty engine operation cases examined in the present study (i.e. faulty operation of fuel injection system either expressed as reduction of injection pressure or reduction of fuel injected mass per engine cycle and faulty operation of the piston-ring assembly expressed as loss of compression) have a direct negative impact on engine operability, availability and reliability and for this reason, each faulty case requires the undertake of specific maintenance actions such as the replacement of excessive wear rings in case of compression loss for the restoration of engine availability and reliability.

ACKNOWLEDGEMENTS

Authors wish to express their gratitude for his teaching and for his kind long-term consulting to the Director of Internal Combustion Engines Laboratory of National Technical University of Athens, Greece Prof. Dr. D. Hountalas. Also, the world-known pioneering work of Prof. Hountalas on diesel engine measurement and diagnostic techniques, who inspired the present study is humbly and gratefully acknowledged by authors.

NOMENCLATURE

A	area, m ²
c	constant
c _v	specific heat capacity under constant volume, J/(kgK)
D _b	piston bowl diameter, m
D _{ho}	injector nozzle orifice diameter, m
D _{inj}	injector hole diameter, m
D _{SM}	Sauter mean diameter, m
E	activation energy, J/kmol
F	zone area, m ²
FA _{st}	fuel-air stoichiometric ratio (by mass)
F _{ho}	nozzle hole discharge area, m ²
h	convective heat transfer coefficient, W/(m ² K)

I	moment of inertia of trapped mass, kgm^2
k_{if}	forward reaction rate constant for the “ith” reaction
l	length, m
m	mass, kg
M	torque, Nm
n	axial velocity exponent
n_r	radial zone number
P	pressure, Pa
\dot{Q}	heat exchange rate, W
r	radial distance, m
R	radius, m
r_0	radius of nozzle hole, m
R_i	one-way reaction rate for the “ith” reaction
R_{mol}	universal gas constant, $\text{J}/(\text{kmolK})$
R_p	piston radius, m
S_{pr}	ignition delay integral
T	temperature, K
t	time, s
u	zone velocity, m/s
\bar{u}	mean velocity, m/s
u_{inj}	injection velocity, m/s
u_p	instantaneous piston velocity, m/s
u_r	radial zone velocity, m/s
u_t	targential air velocity, m/s
u_T	turbulent velocity, m/s
u_{tr}	radial component of targential zone velocity, m/s
u_{tx}	axial component of targential zone velocity, m/s
u_x	axial zone velocity, m/s
V	volume, m^3
W	air angular velocity, rad/s
w	wall jet velocity, m/s
X	jet penetration, m

Greek

α	initial jet angle, rad
δ	wall jet thickness, m
ΔP	pressure difference, Pa
$\Delta\phi$	calculation step
θ	angle of zone with respect to jet axis, rad
λ	thermal conductivity, $\text{W}/(\text{mK})$
μ	dynamic viscosity, $\text{kg}/(\text{ms})$
ν	kinematic viscosity, m^2/s
ρ	density, kg/m^3
σ	Stefan-Boltzmann constant, $\text{W}/(\text{m}^2\text{K}^4)$

Subscripts

a	air
b, bu	burnt

car	characteristic
ev	evaporated
f	fuel
g	gas
ho	hole
i	zone (i)
inj	injection
pr	preparation
s	soot
SM	Sauter mean
st	stoichiometric
t	targential
T	turbulent
w	wall
x,y	coordinates
0	initial step conditions
1	final step conditions

Abbreviations

ABDC	after bottom dead centre
ATDC	after top dead centre
BTDC	before top dead center
CA	crank angle
RMS	root mean square
SMD	Sauter mean diameter

Dimensionless Numbers

Pr	Prandtl number
Re	Reynolds number
We	Weber number

REFERENCES

1. J.B. Heywood, Internal Combustion Engine Fundamentals, New York: McGraw-Hill, 1988.
2. D.T. Hountalas, Prediction of marine diesel engine performance under fault conditions, Applied Thermal Engineering, 20, 1753 – 1783 (2000).
3. V.T. Lamaris and D.T. Hountalas, A general-purpose diagnostic technique for marine diesel engines – Application on the main propulsion and auxiliary diesel units of a marine vessel, Energy Conversion and Management, 51, 740 – 753 (2010).
4. N.B. Jones and Yu-Hua Li, A review of condition monitoring and fault diagnosis for diesel engines, Tribotest, 6-3, (2000).
5. R. Jiang and X. Yan, “Condition Monitoring of Diesel Engines”, In: Complex System Maintenance Handbook. Springer Series in Reliability Engineering. Springer, London, (2008).
6. G.J.J. Oskam, Optimizing Diesel Engine Condition Monitoring, MSc Thesis, Faculty of Mechanical, Maritime and Materials Engineering, Delft University of Technology, (2014).
7. D.T. Hountalas and A.D. Kouremenos, Development and application of a fully automatic troubleshooting method for large marine diesel engines, Applied Thermal Engineering 19, 299-324, (1999)

8. L. Xingyu, S. Gequn, D. Lihui, W. Bin and Y. Kang, "Progress and Recent Trends in the Torsional Vibration of Internal Combustion Engines", *Advances in Vibration Analysis Research*, IntechOpen, (2011), DOI: 10.5772/16222.
9. S.H. Gawande, L.G. Navale, M.R. Nandgaonkar, D.S. Butala and S. Kunamalla, *Fault Detection of Inline Reciprocating Diesel Engine: A Mass and Gas-Torque Approach*, *Advances in Acoustics and Vibration*, Hindawi Publishing Corporation, 2012, Article ID 314706, (2012), doi:10.1155/2012/314706
10. Y. Alhouli, A. Alkhadeli, A. Alzayedi, M. Alardhi and A.I. Abed, *Study of Diesel Engine Vibration Condition Monitoring*", *Global Journal of Researches in Engineering: J General Engineering*, 15(6), (2015).
11. J. Orn J., *Vibration Guideline for Large Diesel Engines*, BSc Thesis, Mechanical and Production Engineering, Vaasa, (2014).
12. H. Raposo, J-T. Farinha, I. Fonseca and L. Andrade Ferreira, *Condition Monitoring with Prediction Based on Diesel Engine Oil Analysis: A Case Study for Urban Buses*, *Actuators*, MDPI, 8,14, (2019), doi:10.3390/act8010014.
13. Z. Li, X. Yan, Z. Guo, Y. Zhang, C. Yuan and Z. Peng, *Condition Monitoring and Fault Diagnosis for Marine Diesel Engines using Information Fusion Techniques*, *Electronics and Electrical Engineering*. – Kaunas: Technologija, 7(123), 109–112, (2012).
14. T.C. Zannis, *Thermodynamic Analysis and Experimental Investigation of the Effect of Liquid Fuels on Diesel Engines*, PhD Thesis, School of Mechanical Engineering, National Technical University of Athens, (2006).
15. R.G. Papagiannakis, *Study of the Behaviour of Diesel Engines with the Use of Liquid and Gaseous Fuels*, PhD Thesis, School of Mechanical Engineering, National Technical University of Athens, Greece, (2002).
16. D.A. Kouremenos, C.D. Rakopoulos and D.T. Hountalas, *Multi-zone Combustion Modelling for the Prediction of Pollutants Emissions and Performance of DI Diesel Engines*, *SAE Transactions, J. of Engines*, 106, 940-957, (1997). SAE Paper No. 970635.
17. C.D. Rakopoulos and D.T. Hountalas, *Development and Validation of a 3-D Multi-zone Combustion Model for the Prediction of a DI Diesel Engine Performance and Pollutant Emissions*, *SAE Transactions, J. of Engines*, 107, 1413–1429, (1998). SAE Paper No. 981021.
18. C.D. Rakopoulos, D.T. Hountalas, G.N. Taklis and E.I. Tzanos, *Analysis of Combustion and Pollutants Formation in a Direct Injection Diesel Engine using a Multi-zone Model*, *Int. J. Energy Research*, 19, 63-88, (1995).
19. C.D. Rakopoulos, D.T. Hountalas and T.C. Zannis, *Theoretical Study Concerning the Effect of Oxygenated Fuels on DI Diesel Engine Performance and Emissions*, *SAE Spring Fuels & Lubricants Meeting & Exhibition*, Society of Automotive Engineers (SAE), June 8-10, (2004), Toulouse, France, SAE Paper No 2004-01-1838.
20. T.C. Zannis, E.I. Pariotis, D.T. Hountalas and C.D. Rakopoulos, *Effects of Air-Side and Fuel-Side Oxygen Addition on DI Diesel Engine Performance and Pollutant Emissions*, *Energy Conversion and Management* 48(11), 2962-2970, (2007).
21. W.J.D. Annand, *Heat Transfer in the Cylinders of Reciprocating Internal Combustion Engines*, *Proc. Instn Mech. Engrs*, 177, 973-990, 1963.
22. D.A. Kouremenos, C.D. Rakopoulos and D.T. Hountalas, *Thermodynamic Analysis of Indirect Injection Diesel Engines by Two-zone Modelling of Combustion*, *Trans. ASME, J. Engineering for Gas Turbines and Power*, 112, 138-159, (1990).
23. D.A. Kouremenos, C.D. Rakopoulos and D.T. Hountalas, *Thermodynamic Analysis of Divided Combustion Chamber Diesel Engine*, *VDI Forschung Ing.-Wesens*, 54, 73-81, (1988).
24. Kamel M. and Watson N., *Heat Transfer in the Indirect Injection Diesel Engine*, SAE Paper No. 790826, (1979).
25. B.E. Launder and D.B. Spalding, *Mathematical Models of Turbulence*, Academic Press, London, (1972).

26. D.A. Willis, W.E. Meyer and C. Birnie, Mapping of Airflow Patterns in Engines with Induction Swirl, SAE Paper No. 660093, (1966).
27. J.C. Dent and J.A. Derham, Air Motion in a Four-Stroke Direct Injection Diesel Engine, Proc. Inst. Mech. Engrs, 188, 269-280, (1974).
28. J.I. Ramos, Internal Combustion Engine Modelling, New York: Hemisphere, (1989).
29. M.B. Glauert, The wall jet, J. Fluid Mechanics, 1, 625-643, (1956).
30. A. Idoum, J.P. Packer, F.J. Wallace and S.J. Charlton, An Experimental and Analytical Study of Jet Impingement and Wall Jets in High Swirl DI Diesel Engine using the Hydraulic Analogy, SAE Paper No. 850263, (1985).
31. H. Hiroyasu, T. Kadota and M. Arai, Development and Use of a Spray Combustion Modelling to Predict Diesel Engine Efficiency and Pollutant Emissions, Bulletin JSME, 26(214), 569-576, (1983).
32. G.L. Borman and J.H. Johnson, Unsteady Vaporization Histories and Trajectories of Fuel Drops injected into Swirling Air, SAE Paper 598C, National Powerplant Meeting, Philadelphia, PA, (1962).
33. D.A. Kouremenos, C.D. Rakopoulos and E.A. Yfantis, A Fortran Program for Calculating the Evaporation Rates in Diesel Engine Fuel Sprays, Advances in Engineering Software, 15, 67-71, (1992).
34. D.A. Assanis, Z.S. Filipi, S.B. Fiveland and M. Syrimis, A Predictive Ignition Delay Correlation under Steady-State and Transient Operation of a Direct Injection Diesel Engine, Trans. ASME, J. of Engineering for Gas Turbines and Power, 125(2), 450-457, (2003).
35. D. Hodgetts and H.D. Shroff, More on the Formation of Nitric Oxide in a Diesel Engine, Conference on "Combustion in Engines", Inst. Mech. Engrs, paper C95/75, 129-138, (1975).
36. C.R. Ferguson, Internal Combustion Engines, New York: John Wiley, (1986).
37. C.D. Rakopoulos, D.T. Hountalas, E.I. Tzanos and G.N. Taklis, A Fast Algorithm for Calculating the Composition of Diesel Combustion Products using 11 Species Chemical Equilibrium Scheme, Advances in Engineering Software, 19, 109-119, (1994).
38. R.J.B. Way, Methods of Determination and Composition and Thermodynamic Properties of Combustion Products for Internal Combustion Engines Calculations, Instn. Mech. Engrs, 190, 687-697, (1977).
39. C. Olikara and G.L. Borman, A Computer Program for Calculating Properties of Equilibrium Combustion Products with Some Applications to I.C. Engines, SAE Paper No.750468, (1975).
40. C.W. Vickland, F.M. Strange, R.A. Bell and E.S. Starkman, A Consideration of the High Temperature Thermodynamics of Internal Combustion Engines, SAE Transactions, 70, 785-793, (1962).